FEDERAL UNIVERSITY OF TECHNOLOGY — PARANA (UTFPR)

GIOVANNI PAOLO MONTAGNOLI

NUMERICAL MODELING OF LIQUID-GAS TWO-PHASE FLOW IN A HYDROGEN PRODUCTION CELL

CURITIBA

2025

GIOVANNI PAOLO MONTAGNOLI

NUMERICAL MODELING OF LIQUID-GAS TWO-PHASE FLOW IN A HYDROGEN PRODUCTION CELL

Modelagem do Escoamento Bifásico Líquido-Gas em Célula de Produção de Hidrogênio

Master's Dissertation submitted in partial fulfillment of the requirements for the degree of Master's Degree in Mechanical and Materials Engineering at the Master's Program in Mechanical and Materials Engineering of Federal University of Technology — Parana (UTFPR).

Advisor: Prof. Dr. Cezar Otaviano Ribeiro Negrão

Co-advisor: Drª. Nezia de Rosso

CURITIBA

2025

Ministério da Educação
Universidade Tecnológica Federal do Paraná
Campus Curitiba

GIOVANNI PAOLO MONTAGNOLI

NUMERICAL MODELING OF LIQUID-GAS TWO-PHASE FLOW IN A HYDROGEN PRODUCTION CELL

Trabalho de pesquisa de mestrado apresentado como requisito para obtenção do título de Mestre Em Engenharia da Universidade Tecnológica Federal do Paraná (UTFPR). Área de concentração: Engenharia Térmica.

Data de aprovação: 05 de Setembro de 2025

Dr. Daniel Augusto Cantane, Doutorado - Fundação Parque Tecnológico Itaipu

Dr. Henrique Stel De Azevedo, Doutorado - Universidade Tecnológica Federal do Paraná

Dr. Maik Becker, Doutorado - Clausthal University Of Technology

Dedico este trabalho à minha família.

ACKNOWLEDGEMENTS

I would like to thank all those who, in some way, contributed to the completion of this work. In particular, I would like to thank my family — my father, my mother, and my brother — for their unconditional support and for always providing the foundation I needed to dedicate myself to this study.

To my beloved Bruna, for being by my side in the final stage of this journey, offering inspiration, confidence, and encouragement that were essential for me to bring it to completion.

To my friends and colleagues, for their friendship and support throughout this process.

I also express my gratitude to Prof. Dr. Cezar Negrão and Prof. Dr. Nezia de Rosso for their guidance during this work and for granting access to the CERNN – Research Center for Rheology and Non-Newtonian Fluids, which was essential for the development of this study.

Finally, I thank Professors Dr. Maik, Dr. Daniel, and Dr. Henrique, members of the examination committee, for their valuable contributions and suggestions, which greatly enriched this research.

Somewhere, something incredible is waiting to be known.

Carl Sagan

RESUMO

O hidrogênio, quando obtido por eletrólise da água, tem ganhado destaque como meio de armazenamento e transporte de energia limpa, devido ao seu baixo impacto ambiental. No entanto, esse meio de produção ainda corresponde a apenas uma fração da produção global de hidrogênio, principalmente devido aos altos custos e à eficiência limitada do processo. Dentre os diversos fatores que afetam o desempenho do processo, a formação de bolhas gasosas nos eletrodos durante a eletrólise se destaca por influenciar diretamente na queda de tensão ôhmica e na hidrodinâmica do sistema, impactando negativamente a eficiência energética e a taxa de produção de gás. Neste contexto, o presente estudo realiza uma investigação numérica detalhada do escoamento bifásico em eletrolisadores de água alcalina, utilizando simulações CFD para avaliar o impacto das características das bolhas, como o diâmetro, a distribuição e as forças interfaciais, na dinâmica do escoamento. Foram comparados modelos monodispersos e polidispersos, permitindo a análise da sensibilidade do sistema à variação dos parâmetros operacionais, como vazão do eletrólito e taxa de geração de gás. Os resultados demonstraram que a heterogeneidade do tamanho de bolhas afeta significativamente a distribuição da fase gasosa, os padrões de recirculação e a estabilidade da camada de gás no eletrodo, reforçando a importância da escolha de modelos mais representativos da realidade. Além disso, a análise das trajetórias e regiões de aprisionamento de bolhas contribui para o entendimento do tempo de residência do gás e fornece subsídios para estratégias de otimização geométrica e operacional da célula eletrolítica.

Palavras-chave: hidrogênio verde; eletrólise da água; escoamento bifásico; simulação numérica; interação entre bolhas.

ABSTRACT

Hydrogen, when produced through water electrolysis, has gained importance as a clean energy carrier and storage medium due to its low environmental impact. However, this production route still accounts for only a small fraction of global hydrogen production, mainly because of the high costs associated with its limited efficiency. Among the various factors affecting process performance, the formation of gas bubbles at the electrodes during electrolysis stands out for directly influencing the ohmic voltage drop and the system's hydrodynamics, which negatively impact energy efficiency and gas production rates. In this context, the present study carries out a detailed numerical investigation of gas-liquid two-phase flow in alkaline water electrolyzers, using CFD simulations to assess the impact of bubble characteristics, such as diameter, distribution, and interfacial forces, on flow dynamics. Monodisperse and polydisperse models were compared, allowing for analysis of the system's sensitivity to variations in operational parameters such as electrolyte flow rate and gas generation rate. The results showed that bubble size heterogeneity significantly affects gas phase distribution, recirculation patterns, and the stability of the gas layer near the electrode, reinforcing the importance of using models that more accurately represent physical reality. Furthermore, the analysis of bubble trajectories and gas entrapment regions contributes to a better understanding of gas residence time and provides a basis for geometric and operational optimization strategies in electrolytic cells.

Keywords: green hydrogen; water electrolysis; two-phase flow; numerical simulation; bubble interaction.

LIST OF FIGURES

LIST OF TABLES

LIST OF ABBREVIATIONS AND ACRONYMS

Pseudo-Acronyms

UTFPR	Federal University of Technology – Paraná
HER	Hydrogen Evolution Reaction
EPE	Brazilian Energy Research Office
SMR	Steam Methane Reforming
CFD	Computational Fluid Dynamics
MUSIG	MUltiple SIze Group
PBM	Population Balance Model

LIST OF SYMBOLS

Symbol	Description	Unit
A	Area	[m^2]
H_2O	Water (liquid phase)	-
H^+	Hydrogen ion (proton)	mol/L
OH^-	Hydroxide ion	mol/L
H_2	Hydrogen gas	mol or mol/L
O_2	Oxygen gas	mol or mol/L
e^-	Electron	C (Coulomb), if used as charge
E_c	Cell potential (or voltage difference)	V (volt)
E_a	Anode potential (oxidation)	V (volt)
H_2	Hydrogen gas	mol or mol/L
O_2	Oxygen gas	mol or mol/L
H_2O	Water (liquid phase)	— (chemical)
OH^-	Hydroxide ion	mol/L
H^+	Hydrogen ion (proton)	mol/L
e^-	Electron	C (Coulomb), if used as charge
W_t	Theoretical energy consumption for H_2 production	kWh/m^3 of H_2
η_e	Maximum energy efficiency	dimensionless or %
V_{td}	Thermodynamic decomposition voltage (e.g., 1.23 V)	V (volt)
U	Total voltage of the electrolytic cell	V (volt)
E_a	Anode potential (oxidation)	V (volt)
E_c	Cathode potential (reduction)	V (volt)
i	Electric current density	A/m^2
$\sum R$	Sum of internal ohmic resistances	Ω·m^2
η_a	Anodic overpotential (energy loss at anode)	V (volt)
η_c	Cathodic overpotential (energy loss at cathode)	V (volt)
R	Total resistance of the electrolytic system	Ω·m^2
R_e	Electrolyte resistance	Ω·m^2
R_m	Membrane (or diaphragm) resistance	Ω·m^2
R_b	Gas bubble resistance (due to bubble presence)	Ω·m^2
R_c	Electrical contact or electrode conduction resistance	Ω·m^2
R	Effective electrolyte resistance with bubbles	Ω·m^2
R_e	Pure electrolyte resistance (no bubbles)	Ω·m^2
ε or ϵ	Gas void fraction	dimensionless
$\vec{V}$	Fluid velocity vector	m/s
ρ	Fluid density	kg/m^3
p	Pressure	Pa (N/m^2)
μ	Dynamic viscosity	Pa·s or kg/(m·s)
$\vec{g}$	Gravity acceleration vector	m/s^2
α_k	Volume fraction of phase k	dimensionless
ρ_k	Density of phase k	kg/m^3
$\vec{V}_k$	Velocity vector of phase k	m/s
P_k	Pressure of phase k	Pa (N/m^2)
$\mu_{\text{eff},k}$	Effective viscosity of phase k (includes turbulence)	Pa·s or kg/(m·s)
$\vec{g}$	Gravity acceleration vector	m/s^2
α_k	Volume fraction of phase k	dimensionless

Continued on next page

Table 1 – continued from previous page

Symbol	Description	Unit
$\vec{F}_L$	Lift force	N
$\vec{F}_D$	Drag force	N
$\vec{F}_{WP}$	Wall lubrication force	N
$\vec{F}_{VM}$	Virtual mass force	N
$\vec{F}_{TD}$	Turbulent dispersion force	N
V_p	Representative volume of the particle or cell	m^3
C_L	Lift force coefficient	dimensionless
$\vec{v}_g$	Gas phase velocity vector	m/s
$\vec{v}_l$	Liquid phase velocity vector	m/s
$\vec{\nabla} \times \vec{v}_l$	Curl of the liquid phase velocity	1/s
Eo'	Modified Eötvös number (for hydrodynamic diameter correction)	dimensionless
σ	Surface tension between fluids	N/m
d_b	Bubble diameter	m
d_h	Corrected hydrodynamic diameter	m
Re_b	Reynolds number of the bubble	dimensionless
C_D	Drag coefficient	dimensionless
A_k	Specific interfacial area of phase k	1/m
$\vec{v}_g - \vec{v}_l$	Relative velocity between gas and liquid	m/s
Re_b	Reynolds number of the bubble	dimensionless
μ_l	Dynamic viscosity of the liquid phase	Pa·s
U_t	Terminal velocity of the bubble	m/s
Mo	Morton number (fluid physical parameter)	dimensionless
J	Auxiliary parameter used in the U_t equation	dimensionless
G	Auxiliary parameter for J regimes	dimensionless
α_g	Volume fraction of the gas phase	dimensionless
d_b	Bubble diameter	m
C_{WL}	Wall lubrication coefficient	1/m
$\vec{n}_w$	Unit normal vector to the wall	dimensionless
C_{LP1}	Empirical constant for calculating C_{WL}	dimensionless
C_{LP2}	Additional empirical constant for C_{WL}	dimensionless
δ_w	Normal distance of the bubble to the wall	m
C_{VM}	Virtual mass force coefficient	dimensionless
C_{DT}	Turbulent dispersion coefficient	dimensionless
k_j	Turbulent kinetic energy of the continuous phase (usually liquid)	m^2/s^2
$\mu_{\text{eff},l}$	Effective viscosity of the liquid phase	Pa·s
μ_t	Turbulent viscosity from k-ε model (common to both phases)	Pa·s
$\mu_{t,l}$	Specific turbulent viscosity of the liquid phase	Pa·s
$\mu_{t,ib}$	Bubble-induced viscosity in the liquid phase	Pa·s
C_{Sato}	Empirical constant from Sato's model for bubbles	dimensionless
$\mu_{\text{eff},g}$	Effective viscosity of the gas phase	Pa·s
f_m	Bubble number density function for group m	$1/m^3$
B_m^c	Source by coalescence for group m	$1/m^3$·s
D_m^c	Sink by coalescence for group m	$1/m^3$·s
B_m^q	Source by breakup for group m	$1/m^3$·s
D_m^q	Sink by breakup for group m	$1/m^3$·s

Continued on next page

Table 1 – continued from previous page

Symbol	Description	Unit
F_m	Bubble breakup frequency for group m	1/s
M_m	Mean deformation rate for group m	1/s
N_m	Breakup efficiency for group m	dimensionless
$\Omega_Q(d_m,d_n)$	Daughter generation rate of size d_n from mother bubble d_m (redistribution function)	1/(m·s)
τ_{destr}	Deformation stress available for breakup	Pa (N/m^2)
τ_{crit}	Critical stress for bubble breakup	Pa
d_K	Diameter of daughter bubble resulting from breakup	m
d_m	Diameter of "mother" bubble (before breakup)	m
d_n	Diameter of "daughter" bubble (after breakup)	m
d_32	Sauter mean diameter (volume-to-surface equivalent diameter)	m
τ_{crit1}	First condition of critical stress	Pa
τ_{crit2}	Second condition of critical stress	Pa
ε_l	Turbulent dissipation rate of the liquid phase	m^2/s^3
k_l	Turbulent kinetic energy of the liquid phase	m^2/s^2
ω_l	Specific dissipation rate of the liquid phase (per unit energy)	1/s
C_μ	Empirical constant from the k-ω turbulence model (typically 0.09)	dimensionless
$\Gamma(m_i;m_j)$	Total coalescence rate between groups m_i and m_j	1/(m^3·s)
$\alpha_{g,\text{max}}$	Maximum gas volume fraction	dimensionless
Γ_{turb}	Coalescence rate by turbulence	1/(m^3·s)
Γ_{buoy}	Coalescence rate by buoyancy	1/(m^3·s)
Γ_{eddy}	Coalescence rate by turbulent eddies	1/(m^3·s)
Γ_{shear}	Coalescence rate by shear	1/(m^3·s)
Γ_{wake}	Coalescence rate by wake effect	1/(m^3·s)
Γ	Coalescence rate for a specific mechanism	1/(m^3·s)
h	Collision frequency between bubble pairs	1/s
λ	Coalescence efficiency (probability after collision)	dimensionless
A	Effective collision area between two bubbles	m^2
u_{rel}	Relative velocity between two bubbles	m/s
$u_{\text{rel,wake}}$	Relative velocity induced by wake of a bubble	m/s
C_{wake}	Empirical coefficient for wake coalescence model	dimensionless
$U_{T,i}$	Terminal velocity of bubble i	m/s
$C_{D,i}$	Drag coefficient of bubble i	dimensionless
Θ_i	Window function for coalescence based on bubble i size	dimensionless
d_{crit}	Critical bubble diameter for onset of coalescence	m
$\lambda_{\text{inertial}}$	Inertial regime coalescence efficiency	dimensionless
C_{eff}	Inertial coalescence efficiency coefficient	dimensionless
$We_{ij,\text{max}}^{0.5}$	Square root of maximum Weber number between bubbles i and j	dimensionless
d_{eq}	Equivalent diameter between two bubbles	m
λ_{viscous}	Viscous regime coalescence efficiency	dimensionless
μ_l	Dynamic viscosity of the liquid phase	Pa·s
γ_{edd}	Local turbulent shear rate	1/s
A_H	Hamaker constant (molecular interaction force)	J
$\ln$	Natural logarithm (mathematical)	—

Continued on next page

Table 1 – continued from previous page

Symbol	Description	Unit
ρ_{KOH}	Density of potassium hydroxide (KOH) electrolyte	kg/m^3

CONTENTS

1 INTRODUCTION

Renewable energy sources have emerged as a promising solution in the transition to a cleaner and more efficient energy matrix. This shift is driven by growing awareness of environmental challenges and the urgent need to find sustainable alternatives to meet global energy demands (PANT; GUPTA, 2009). In this context, hydrogen has gained importance not only as a clean energy carrier but also as an efficient storage medium, especially suitable for integrating intermittent renewable sources, due to its low environmental impact. This growing interest has stimulated the development of hydrogen as a viable alternative to fossil fuels (BALL; WEEDA, 2015). Among the various methods for hydrogen production, water electrolysis stands out as a renewable pathway, particularly when powered by sources such as wind or solar energy (DAWOOD *et al.*, 2020). However, only a small fraction of the hydrogen currently produced comes from electrolysis. The vast majority is still derived from hydrocarbon sources such as natural gas, oil, and coal — processes that result in significant environmental pollution (BALAT, 2008).

The limited adoption of water electrolysis as a hydrogen production method is primarily due to its high cost relative to its low energy efficiency. According to the U.S. Department of Energy, the cost of hydrogen produced via electrolysis is approximately five times higher than that produced through natural gas reforming (PANT; GUPTA, 2009). This high production cost is mainly attributed to energy losses caused by internal resistances within the system, particularly in the electrodes. These losses lead to an increase in the operating voltage of the electrolyzer, resulting in greater energy consumption for the same amount of hydrogen produced (AVCI; TOKLU, 2022).

A significant portion of the energy losses in electrolysis is attributed to the internal resistance of the system, particularly due to the presence of hydrogen and oxygen bubbles generated at the electrode surfaces. These bubbles act as barriers to current transfer and alter the electrolyte flow, thereby reducing the efficiency of the electrochemical reactions. Studies indicate that bubble-induced resistance may account for up to 33.4% of the total potential losses in alkaline electrolyzers (ZENG; ZHANG, 2010).

The dynamics of gas bubbles constitute a complex and poorly understood two-phase flow problem. The distribution and behavior of these bubbles influence not only the overpotential, but also the electrical resistance within the electrolyte and the efficiency of gas removal from the reaction zone. Understanding these phenomena is essential for optimizing the performance of alkaline water electrolyzers (AVCI; TOKLU, 2022)

Numerical simulation based on computational fluid dynamics (CFD) has proven to be a valuable tool for investigating two-phase flow behavior in electrochemical systems. This modeling approach allows for a detailed representation of the interactions between the gas and liquid phases. However, many studies still rely on simplified assumptions, such as treating the system as monodisperse and considering only a limited set of interfacial forces, typically drag and lift (AVCI; TOKLU, 2022; BIDEAU *et al.*, 2020). Such simplifications overlook essential aspects of

the actual flow dynamics, including bubble size distribution, turbulence effects induced by the gas phase, and the breakup and coalescence mechanisms characteristic of polydisperse systems.

Based on this context, the present work proposes to model numerically the gas-liquid flow in alkaline water electrolyzers, with a focus on studying the dynamics of hydrogen bubbles. Using a polydisperse Euler–Euler model (MUSIG), the study aims to evaluate how operational variables, such as bubble size and electrolyte flow rate, influence the void fraction of the gas phase and the velocity profiles of the electrolyte. This analysis seeks to deepen the understanding of two-phase flow behavior in electrolyzers, providing relevant insights to improve the performance of the electrolysis process.

1.1 General Objective

Based on the premises and opportunities discussed above, this study aims to investigate the behavior of two-phase flow in an alkaline water electrolyzer. Using a polydisperse Euler–Euler model, the analysis focuses on evaluating the influence of bubble size and electrolyte flow rate on the velocity profiles and gas void fraction distribution.

1.2 Specific Objective

- Develop a mathematical model based on the Euler–Euler approach, coupled with the polydisperse MUSIG model.
- Implement relevant interfacial forces, including drag, lift, wall lubrication, virtual mass, and turbulent dispersion.
- Incorporate turbulence models such as SST, Gamma–Theta transition model, and models for bubble-induced turbulence.
- Compare the numerical results with experimental data available in the literature.
- Simulate different operating conditions, such as variations in bubble diameter and electrolyte flow rate, to evaluate their impact on the electrolyte velocity profiles and the distribution of void fraction among bubble size groups.

1.3 Justification

Understanding the fluid dynamics within the electrolyzer is of great interest to researchers due to the significant impact that the products generated during electrolysis, particularly gas bubbles, have on hydrogen production efficiency. The formation and accumulation of bubbles on electrode surfaces can hinder reaction rates and lead to a reduction in the overall performance of the system (AVCI; TOKLU, 2022).

To address this issue, the present study aims to contribute to the understanding of the physical phenomena involved in alkaline water electrolysis. Computational simulations of two-phase flow and bubble dynamics are essential for developing strategies that facilitate the release of gas from electrode active sites, thereby enhancing the overall efficiency of hydrogen production.

The mathematical modeling of two-phase flow within the production cell contributes to the scientific advancement of this technology. Therefore, understanding the flow behavior and the interaction between phases is a crucial step toward consolidating alkaline water electrolysis as a viable component of the global energy matrix.

1.4 Structure

The first chapter of this work presents the Introduction, which includes the contextualization of the study, the justification, and the general and specific objectives of the research. Subsequently, Chapter Two presents the Literature Review, offering an analysis of the theoretical background and existing studies on alkaline water electrolyzers available in the literature.

Chapter Three focuses on Materials and Methods, describing the geometry of the study and its characteristics, as well as the mathematical model developed. This section also details the boundary conditions applied in the computational simulation, the numerical procedures adopted, the software used, the convergence criteria, and the simulation time. Additionally, a mesh sensitivity analysis is presented for the single-phase case, as well as for the monodisperse and polydisperse two-phase flow simulations.

In the Results and Discussion section, the numerical model is calibrated using experimental data from the literature, followed by an analysis of the results obtained through the simulations. The Conclusions and Suggestions for Future Work section summarizes the main findings of the study, discusses their implications, and outlines the next steps of the research, focusing on deepening the investigation and expanding the proposed model.

2 LITERATURE REVIEW

2.1 Theoretical Background

The chemical process of electrolysis consists of breaking down a substance through the conduction of electrical energy. The decomposition of the element results in the conversion of electrical energy into chemical energy (HAMANN *et al.*, 2007). During the ionization of water, stimulated by the electric current flowing through the electrochemical system, the generated products undergo oxidation and reduction reactions at the electrodes. The electrolytic cell contains two electrodes, made of various materials, immersed in an electrolytic conductor, usually a liquid, referred to as the electrolyte (GONZALEZ; TICIANELLI, 1998).

The system configuration presents some operational variations depending on the type of electrolytic cell; however, the present study aims to focus only on the principles of alkaline water electrolyzers (AWE). Water ionization involves the dissociation of the molecule into two components: hydrogen ions (H^+) and hydroxide ions (OH^-). After dissociation, hydrogen ions migrate to the cathode (negative electrode), while hydroxide ions are transferred to the positive side of the cell through a porous separator and migrate toward the anode (positive electrode). At the cathode, the hydrogen ions undergo a reduction process, gaining two electrons and forming hydrogen in its gaseous form. This process is known as the hydrogen evolution reaction (HER). At the anode, hydroxide ions undergo an oxidation process, releasing two electrons and forming liquid water and gaseous oxygen. This process is known as the oxygen evolution reaction (OER). Figure 1 presents a schematic of the electrolysis process in alkaline water electrolysis cells.

The half-reactions occurring during the electrolysis process are described by the equations below:

Water Ionization:

$$2H_2O(l) \rightarrow 2H^+(g) + 2OH^-(aq) \tag{1}$$

Half-reactions:

$$\text{Reduction:} \qquad 2H^+(g) + 2\,e^- \rightarrow H_2(g) \tag{2}$$

$$\text{Oxidation:} \qquad 2\text{OH}^-(aq) \rightarrow 2\,e^- + H_2O(l) + \frac{1}{2}O_2(g) \tag{3}$$

Overall Reaction:

$$H_2O(l) \rightarrow H_2(g) + \frac{1}{2}O_2(g) \tag{4}$$

The performance of hydrogen production is directly related to the electrical properties of the electrolysis cell. The main challenge in hydrogen production via electrolysis is the low gas evolution rate in relation to the high consumption of electrical energy. The process typically

Figure 1 – Schematic of alkaline water electrolysis

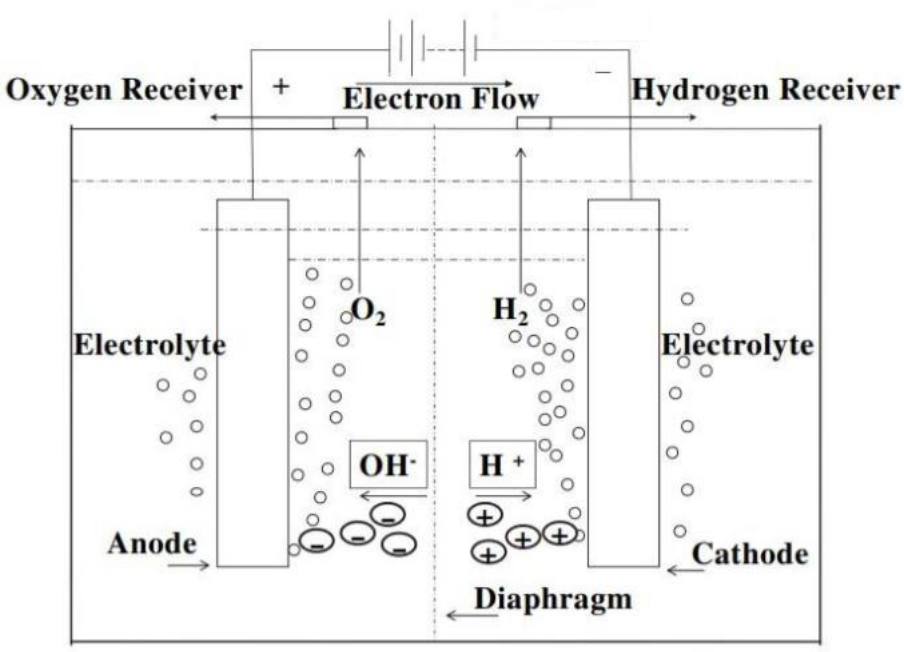

Source: Adapted from (ZENG; ZHANG, 2010).

requires an energy consumption of 4.5 to 5 kWh/m³ of H_2 in industrial applications (WANG *et al.*, 2014). Under conditions of 25℃ and 1 atm, the equilibrium reaction of electrolysis generates a potential of 1.23 V, as shown below:

$$\text{Cathode:} \qquad 2H^+(g) + 2e^- \rightarrow H_2(g) \quad E_c^\theta = -0{,}83\,\text{V} \tag{5}$$

$$\text{Anode:} \qquad 2\text{OH}^-(aq) \rightarrow 2\,e^- + H_2O(l) + \frac{1}{2}O_2(g) \quad E_a^\theta = 0{,}40\,\text{V} \tag{6}$$

$$\text{Overall Reaction:} \qquad H_2O(l) \rightarrow H_2(g) + \frac{1}{2}O_2(g) \quad E_c^\theta = 1{,}23\,\text{V} \tag{7}$$

The theoretical energy consumption (W_t) for hydrogen production with a thermodynamic decomposition voltage of 1.23 V is equivalent to 2.94 kWh/m³ of H2. However, in real hydrogen production processes, no hydrogen evolution reaction (HER) occurs before the system reaches a potential between 1.8 and 2.6 V. Since these values are higher than the theoretical potential, the practical energy consumption (W_p) reaches values around 4.78 kWh/m³ of H2. This disparity between theoretical and practical consumption results in a maximum energy efficiency (ηe) of 61.5% (WANG *et al.*, 2014). In a comparative analysis with other production processes, such as natural gas reforming, data from the Brazilian Energy Research Office (EPE) published in 2022 indicate that the conversion efficiency of methane into blue hydrogen using SMR (Steam Methane Reforming) technology is 75%. The factors that contribute to the increase in cell voltage

are related to the theoretical decomposition voltage, reaction overpotential, and ohmic voltage drop (WANG *et al.*, 2014). The theoretical voltage is defined by the following equation:

$$U = E_a - E_c + i \cdot \sum R = U^\theta + |\eta_a| + |\eta_c| + i \cdot \sum R \tag{8}$$

According to the equation, E_a represents the anode potential for the oxygen evolution reaction, E_c is the cathode potential for the hydrogen evolution reaction, i is the current density, $\sum R$ is the total ohmic resistance, U^θ is the theoretical decomposition voltage, η_a is the anode overpotential, and η_c is the cathode overpotential. The voltage of the water electrolysis cell consists of three components: the theoretical decomposition voltage (U^θ), the reaction overpotential (η) and the ohmic voltage drop ($i \cdot \sum R$). The ohmic voltage drop is the product of the current density (i) and the total ohmic resistance ($\sum R$).

The total resistance embraces all resistive contributions of the system, and the potential difference required to overcome this resistance is known as the ohmic voltage. Since part of the applied energy is dissipated as heat, the process becomes less efficient (WANG *et al.*, 2014). This quantity is represented by the product of the current density, in A/m², and the sum of the ohmic resistances present in water electrolysis. The sum of the ohmic resistances is expressed by the following equation:

$$\sum R = R_e + R_m + R_b + R_c \tag{9}$$

Each term in the equation represents a specific component of this resistance. R_e, referred to as the electrolyte resistance, corresponds to the electrical resistance of the conductive solution used in electrolysis, commonly composed of water and an electrolyte such as KOH or N_aOH. The term R_m, or membrane resistance, represents the electrical resistance imposed by the electrolytic membrane, which separates the areas where oxidation and reduction reactions occur during the process. R_b, or bubble resistance, is associated with the resistance caused by the formation and release of gas bubbles (such as hydrogen and oxygen) during electrolysis. Finally, R_c, or circuit resistance, refers to the electrical resistance in the external circuit, including conductive wires and connections, as part of the path followed by the external current to complete the circuit. Understanding these terms is essential for identifying and addressing the sources of resistance within the electrolysis system, contributing to the optimization of the electrochemical process efficiency (WANG *et al.*, 2014).

During the electrolysis process, the resulting products (hydrogen and oxygen) are generated at the active sites of the electrode, leading to supersaturation and bubble formation. These bubbles accumulate on the electrode surface and gradually grow until they reach a critical size, at which point they detach from the electrode and rise into the electrolyte solution (KIUCHI *et al.*, 2006). The resistance caused by bubbles (R_b) has a significant influence on the system's ohmic voltage drop, as it also affects the electrolyte resistance (R_e) and the electrode overpotentials

(η). Gas bubbles adsorbed on the electrode surfaces reduce the active area (A_e) responsible for gas evolution. This surface blockage reduces the distribution of electric current along the electrode, resulting in an increase in the system's actual current density and, consequently, raising the overpotential. Thus, it is possible to identify a relationship between the electrode coverage rate caused by bubbles and the current density (KRENZ, 1984). In addition, the distribution of bubbles within the medium also alters the electric field, leading to an increase in the electrolyte resistance (WANG *et al.*, 2014).

The presence of bubbles reduces the electrolyte conductivity by increasing the system's effective resistance as a function of the void fraction (ϵ) in the foam layer formed over the electrodes. Here, (R_e) represents the system without bubbles, and (R_ϵ) corresponds to the resistance in the presence of bubbles. This fraction represents the gas-to-total volume ratio and is influenced by parameters such as current density, bubble layer thickness, and electrode spacing. The Bruggeman equation (Equation 10) has been widely adopted as a basis for estimating the additional resistance imposed by the gas phase in alkaline electrolyzers (RUE *et al.*, 1953).

$$\frac{R_\varepsilon}{R_e} = (1-\varepsilon)^{-\frac{3}{2}} \tag{10}$$

The validity of the Bruggeman equation has been confirmed by studies that relate bubble dispersion to the effective ohmic resistance of the cell. The non-uniform distribution of the void fraction along the electrode directly affects electrochemical performance, especially in the upper regions, where the bubble layer is thicker and the cell voltage increases proportionally to the difficulty of removing the gas phase. (JANSSEN, 2000; MANDIN *et al.*, 2014, 2014). Figure 2 illustrates the variation of the void fraction along the electrolytic cell, as experimentally observed in an electrolysis cell.

The bubbles generated during electrolysis are among the main factors that compromise process efficiency, accounting for potential losses that can reach up to one-third of the total energy lost. As demonstrated by Zeng e Zhang (2010), the potential losses caused by bubbles in the electrolyzer account for up to 33.4% of the total process losses. The difficulty in removing these bubbles from the electrode surfaces contributes to an increase in both the reaction overpotential and ohmic resistance, highlighting the need for more effective approaches to promote their release and transport within the electrolyte. To achieve this, it becomes essential to adopt numerical models that represent the two-phase flow inside electrolyzers, aiming to understand the interaction mechanisms between phases and to develop optimization strategies (ZENG; ZHANG, 2010).

Figure 2 – Representation of the electrolyzer's two-phase medium at three different locations (x = 5, 15, and 25 mm)

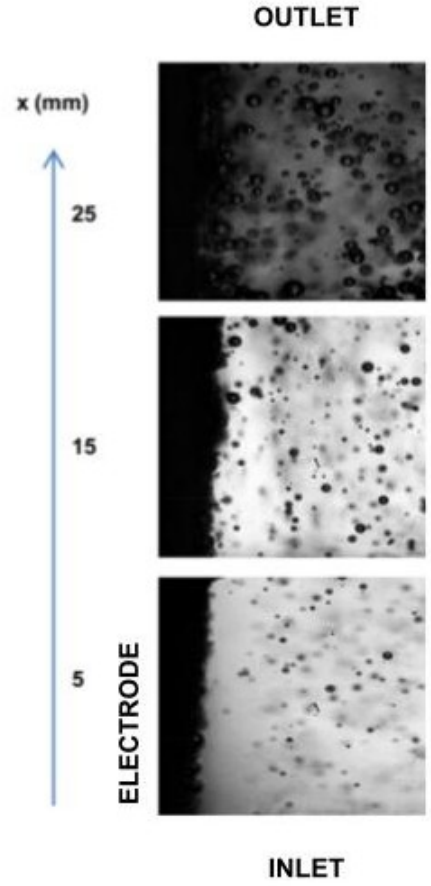

Source: (ABDELOUAHED *et al.*, 2014b).

2.2 Two-Phase Flow in Electrolyzers

Recent advances in computational performance and numerical methods have enabled increasingly detailed simulations of two-phase flows with dispersed bubbles. Among the various available models, two-fluid models stand out as robust approaches for representing multiphase systems at engineering scales (YAN *et al.*, 2020). In this class of models, the conservation equations of mass, momentum, and energy are formulated for a fixed control volume in which both phases coexist and are treated as continuous and interpenetrating fluids. The model operates with two main categories of local equations: the governing equations for each phase and the equations that describe the interfacial interactions between them. Each phase is represented by a local volume fraction, such that the sum of the phase fractions at every point in space and time is always equal to one (ISHII; MISHIMA, 1984)

Among the multiphase flow modeling approaches, the Lagrangian and Eulerian formulations are alternatives for obtaining detailed descriptions of complex flow fields. Lagrangian models are useful for calculating bubble trajectories immersed in a continuous medium, as well as their interactions. This approach, when applied to dispersed flow regimes, enables each par-

ticle's motion to be resolved individually, which helps in understanding specific details of the physics involved. However, when the aim of the study is a global analysis, the large number of particles can result in an unviable computational cost (ANSYS, Inc., 2019).

In such cases, the Eulerian–Eulerian formulation arises as an efficient alternative, especially for describing complex flows involving a large number of small bubbles distributed throughout the domain, as observed in electrolyzers operating under direct current and continuous gas generation (SANKARANARAYANAN; SUNDARESAN, 2002). In this approach, both the continuous phase (electrolyte) and the dispersed phase (gas) are treated as interpenetrating fluids, with the conservation equations solved separately for each phase. The interactions between them are modeled through interfacial forces and momentum exchange, allowing for the simulation of the collective behavior of bubbles without the need to individually track each particle. For the mathematical model to adequately represent the phenomenon, these interaction forces between the continuous and dispersed phases must be taken into account, as they play a fundamental role in the dynamics of bubbles generated during two-phase flow (WANG *et al.*, 1987)

Once formed on the electrode surface, bubbles remain adhered for a brief period, sustained by the balance between surface tension effects and the contact angle. Once formed, they become subject to the forces resulting from the electrolyte flow. As the bubble diameter increases, the contact angle tends to decrease, enlarging the interfacial area between the bubble and the liquid, which helps its detachment (AVCI; TOKLU, 2022).

When the bubble reaches a critical size, the resulting force acting against adhesion overcomes the tension that holds it attached to the electrode surface, leading to its detachment. From that moment on, the bubble begins to interact dynamically with the flow. Mathematical models of two-phase flows describe this behavior as the result of the combined action of different interfacial forces, whose intensity and direction vary according to the local velocity field, fluid properties, and bubble size. These forces are responsible for determining the bubble's trajectory throughout its path in the electrolyte (AVCI; TOKLU, 2022).

This interaction is commonly described as a combination of drag force and other interfacial forces, such as the lift force. The drag force represents the resistance encountered by the bubble as it moves through the fluid, resulting from the relative velocity between the phases. The lift force, in turn, arises due to the asymmetry of the velocity field around the bubble and is proportional to the fluid velocity gradient. It acts perpendicular to the flow direction, causing lateral migration of the bubble. Additional forces can also be incorporated into the mathematical model. For example, in the case of a high velocity gradient, an inertial force known as the virtual mass force due to rapid changes in bubble velocity is created. Additionally, the wall lubrication force, which is the force exerted on the bubble as it approaches a wall, also takes place (BESAGNI *et al.*, 2023).

In flows with a high concentration of bubbles, turbulence dispersion may also occur. This phenomenon happens when turbulent fluctuations in the continuous fluid induce the spreading of the dispersed phase, promoting bubble migration from high to low concentration regions. Tur-

bulent dispersion contributes significantly to flow homogenization and to the stability of the gas phase. Disregarding it in mathematical models may lead to the underestimation of void fraction in certain regions and a loss of accuracy in predicting bubble distribution. The inclusion of this term has proven essential in simulations aiming to accurately represent two-phase behavior in alkaline electrolyzers (MARFAING *et al.*, 2016; DAVIDSON, 2014).

2.3 Interfacial Forces

Interfacial forces play an important role in the dynamics of two-phase flows, especially in gas–liquid systems, where they have a significant influence on the behavior of bubbles in the continuous phase. These forces, such as drag force, lift force, virtual mass force, wall lubrication force, and turbulent dispersion force, must be properly modeled to ensure accurate numerical simulations (SHANG, 2015). The correlations for these forces are derived from numerical and experimental studies involving the individual analysis of bubbles in a continuous medium. The following section discusses studies that address each of these forces, presenting different approaches and correlations found in the literature.

2.3.1 Drag Force

The drag force acting on bubbles is influenced by the viscosity of the continuous phase acting on the bubble surface, referred to as skin drag, as well as by pressure differences caused by the shape of the bubble, referred to as form drag. This force acts as a resistance to the movement of bubbles in the continuous phase and depends directly on the drag coefficient and the interfacial area (YAMOAH *et al.*, 2015).

Several models have been proposed to calculate the drag coefficient, and they are commonly used in CFD simulations. One of the most well-known is the model by CLIFT *et al.* (1978), which is applicable in cases of low gas volume fractions. Ishii e Zuber (1977) developed a mixture viscosity model to derive drag coefficient correlations for each flow regime.

Another important model in the literature is that of Tomiyama (1998), who developed constitutive equations for the drag coefficient of single bubbles by varying parameters such as liquid properties and bubble diameter. Bertola *et al.* (2004) identified that as the volume fraction increases, the interaction between bubbles becomes more significant, leading to collisions, coalescence, and breakups, which greatly affect the drag force. Later, Simonnet *et al.* (2007) developed a correlation for the drag coefficient based on laser Doppler velocimetry experiments, applicable to local void fractions of up to 30%.

2.3.2 Lift Force

The lift force is a lateral force acting on a bubble immersed in a viscous flow. This force arises due to the asymmetric velocity field to which the bubble is exposed. It plays a fundamental role in the distribution of the void fraction in a gas–liquid two-phase flow, especially in upward flows, where a non-uniform pressure distribution over the bubble surface generates a force perpendicular to the flow direction.

Several studies have investigated the lift force acting on particles and bubbles in a flow. Saffman (1965) developed a correlation for the shear-induced lift force on spherical particles. Dandy e Dwyer (1990) proposed specific correlations for the lift coefficient of spherical particles. Later, Mclaughlin (1991) expanded this understanding by exploring the dynamics of particles and bubbles in flow, highlighting how flow conditions influence the lift force. Legendre e Magnaudet (1998) contributed to the study of lift force on deformed bubbles by developing correlations that account for bubble deformation under varying flow conditions.

Tomiyama (1998) made significant contributions by identifying that the lift coefficient for deformed bubbles can undergo a sign change, which explains the different behaviors between large and small bubbles. Later, Schmidtke *et al.* (2005) numerically demonstrated how variations in the lift coefficient lead to lateral separation of bubbles of different sizes, validating their results with the experimental findings of Tomiyama *et al.* (2002). Lucas *et al.* (2005) also identified the dependence of lateral deviation on bubble diameter in polydisperse bubbly flows and vertical pipes. In an air–water flow, they observed a reversal in the direction of the lift force within the shear field at a bubble diameter of approximately 5.6 mm.

2.3.3 Wall Lubrication Force

The wall lubrication force plays a fundamental role in the distribution of voids near the wall in a two-phase flow. This force arises in situations where lateral forces, such as the lift force, displace the bubble trajectory toward the wall of the geometry. Due to a velocity difference between the electrolyte flow and the liquid at the bubble–wall interface, the lubrication force repels the bubble, preventing it from coming into contact with the surface (LOTE *et al.*, 2018). Studies by Antal *et al.* (1991) and Frank *et al.* (2008a) have experimentally investigated this phenomenon.

In the study by Antal *et al.* (1991), the wall lubrication force was defined as being generated by a change in the velocity distribution around particles near the wall. When a rising bubble approaches the wall, it is exposed to an asymmetric velocity field. This occurs because the liquid between the bubble and the wall flows at a lower velocity than the liquid on the opposite side, which is not subjected to wall friction. This asymmetry in the velocity field generates a hydrodynamic force that pushes the bubble away from the wall. Later, Tomiyama *et al.* (1995) applied modifications to correct the model proposed by Antal *et al.* (1991).

2.3.4 Virtual Mass Force

The virtual mass force arises from the interaction between a moving bubble and the surrounding liquid. When the bubble moves through the fluid, it causes a disturbance in the adjacent liquid. This phenomenon influences the bubble's trajectory, as the surrounding liquid is accelerated due to the interaction (SHANG, 2015). Drew e Lahey (1987) developed a formula to describe this force, which depends on the virtual mass coefficient (C_{VM}), and is sensitive to parameters such as bubble shape and gas void fraction (CHEN, 2004). Although Mudde e Simonin (1999), in an experimental study, identified that the virtual mass force plays a significant role in predicting oscillations in bubble behavior, many studies choose to neglect its effects under certain conditions (SHANG, 2015).

Studies by Krishna e Baten (2001) and Oey *et al.* (2003), for example, found that in flows where other forces, such as drag and lift, play a more significant role in bubble behavior, the virtual mass force can be neglected. Frank *et al.* (2008a) also observed that, in steady-state flow regimes, the influence of this force is less important for identifying variations in bubble behavior compared to other forces.

2.3.5 Turbulent Dispersion Force

The turbulent dispersion force arises from the velocity fluctuations of the liquid acting on the bubbles. This phenomenon results from the combined effects of turbulence and interphase drag force and has a significant influence on gas volume fraction profiles (YAMOAH *et al.*, 2015). The gradient of the gas volume fraction influences this force, which tends to homogenize the void fraction distribution along the flow (WANG *et al.*, 2014). The studies by Bertodano (1991) and later by Lahey *et al.* (1993) were among the first models developed to describe these turbulent interactions (YAMOAH *et al.*, 2015).

Burns *et al.* (2004) proposed a turbulent dispersion force model based on the time-averaged fluctuating component of the interfacial drag force. Later, Shang (2015) numerically studied upward and downward two-phase flows in pipes using the model developed by Burns *et al.* (2004) to describe turbulent dispersion and obtained satisfactory results when compared to experimental studies by Sun *et al.* (2004) and Wang *et al.* (2014).

Bertodano *et al.* (2006) developed a new model to describe the turbulent dispersion force. The authors identified that this force becomes particularly relevant in two-phase flows. In such cases, the interaction between bubbles and the surrounding fluid turbulence intensifies bubble dispersion, significantly affecting the void fraction distribution. The proposed model contributes to the study of two-phase flow behavior, where turbulent dispersion plays a significant role in flow dynamics (WANG *et al.*, 2014).

2.4 Bubble Dynamics in Two-Phase Flows

In addition to interfacial forces, the motion of bubbles within the continuous medium induces significant disturbances in the flow, altering velocity distribution, void fraction, and phase interactions.

These changes are especially relevant in electrolytic systems, where bubbles not only respond to the flow but also influence it. As a result, it becomes necessary for mathematical models of two-phase flows in the dispersed regime to incorporate an additional effect associated with the presence of bubbles in the continuous medium: bubble-induced turbulence.

Due to the influence that bubbles exert on the continuous medium, simulation models must accurately represent the turbulent energy generated by bubble–fluid interaction. In electrolyzers, the flow may simultaneously exhibit laminar and turbulent regions within the same plane, as a result of the action of rising bubbles. This behavior is frequently described in the literature by the concept of bubble-induced turbulence (YEOH; TU, 2009). Numerical models propose that part of the drag force exerted on the bubbles is converted into turbulent kinetic energy, especially in the bubble wake, generating vortices and flow fluctuations (RZEHAK; KREPPER, 2013). Figure 3 illustrates this phenomenon.

Figure 3 – Representation of turbulence induced by a bubble during two-phase flow

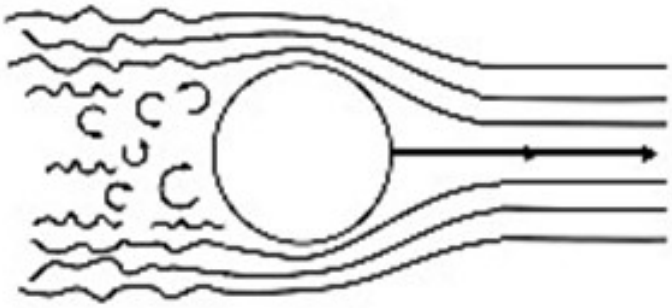

Source: Adapted from (AZEVEDO, 2019).

In addition to turbulence, another important characteristic is the way in which the bubbles are distributed within the flow. The interaction between the liquid and gas phases is essential not only for determining the characteristics of the two-phase flow, but also for understanding the behavior of the electrolyte and the bubbles along the flow path. As gas bubbles move through the continuous medium, they not only affect fluid dynamics but also generate disturbances that must be accounted for in mathematical models. This complex dynamic results in key characteristics for analysis, such as variations in bubble velocity profiles. It also influences the nature of the boundary layer, where bubbles begin to disperse and mix with the liquid (BIDEAU *et al.*, 2020).

Electrolysis studies generally treat the two-phase flow in the electrolyzer as belonging to the bubbly flow regime. In this regime, the bubbles formed at the electrode remain relatively dispersed within the electrolyte, and the interaction between phases is characterized by a high mixing rate (AVCI; TOKLU, 2022).

The way bubbles are distributed within the electrolyte is a key factor for the accuracy of two-phase flow modeling (CHANDRAN *et al.*, 2015). Avci e Toklu (2022) identified that the two-phase flow pattern is directly related to the void fraction and the electrolyte velocity. Along the channel, variations in bubble diameter significantly influence the flow behavior.

Several studies opt for the use of monodisperse models to represent gas production during electrolysis (JOMARD *et al.*, 2008; CHARTON *et al.*, 2009; BIDEAU *et al.*, 2020). This simplification reduces the complexity of the analysis and the computational cost of numerical simulations (BIDEAU *et al.*, 2020). However, this approach does not adequately represent the actual behavior of the electrolysis process, in which bubbles exhibit a wide range of sizes (BOISSONNEAU; BYRNE, 2000).

The variation in bubble size along the flow is influenced by several factors. Nagai *et al.* (2003) observed that bubble diameter is highly dependent on the electric current density applied to the system. However, the main mechanisms responsible for this variability are bubble coalescence and breakup, phenomena that occur continuously during the electrolysis process (BOISSONNEAU; BYRNE, 2000).

These interaction mechanisms between bubbles have a major influence on the flow pattern, which coalescence is one of the most significant (LUCAS *et al.*, 2003). Coalescence results from bubble collisions, driven by factors such as turbulence which intensifies velocity fluctuations in the fluid (LIAO *et al.*, 2015).

Bubble interactions during upward flows generally occur due to differences in bubble velocities. These variations can be caused by velocity gradients within the flow, where bubbles in different regions may be exposed to different velocities, resulting in a relative rising velocity between bubbles (CHENG *et al.*, 2010).

Inertial and gravitational forces also influence the coalescence process. Due to differences in bubble diameters, these forces can vary in their degree of influence on the bubbles depending on particle density. Another essential mechanism in the coalescence process is wake capture, where bubbles are drawn into the wake of a larger bubble. Smaller bubbles caught in this wake may be pulled toward the larger bubble generating the drag, resulting in collisions (LIAO *et al.*, 2015). These mechanisms are illustrated in Figure 4.

In addition to coalescence, bubble breakup is also a fundamental phenomenon that affects the dynamics of two-phase flow. When a bubble is immersed in a flow, it is subjected to a disruptive tension that acts to deform and break it. In contrast, the surface tension of the bubble provides a restoring force, requiring a minimum tension, known as the critical stress, for breakup to occur. As illustrated in Figure 5, when the disruptive tension exceeds the critical stress, the bubble breaks. Therefore, the frequency of bubble breakup depends on the balance between these two tensions (SUN *et al.*, 2004).

Polydisperse studies of bubble breakup and coalescence couple population balance equations with the mathematical model to accurately represent this phenomenon. Several models aim to describe the distribution of bubble sizes throughout the flow. The most widely used is

Figure 4 – Representation of bubble coalescence mechanisms in a two-phase flow

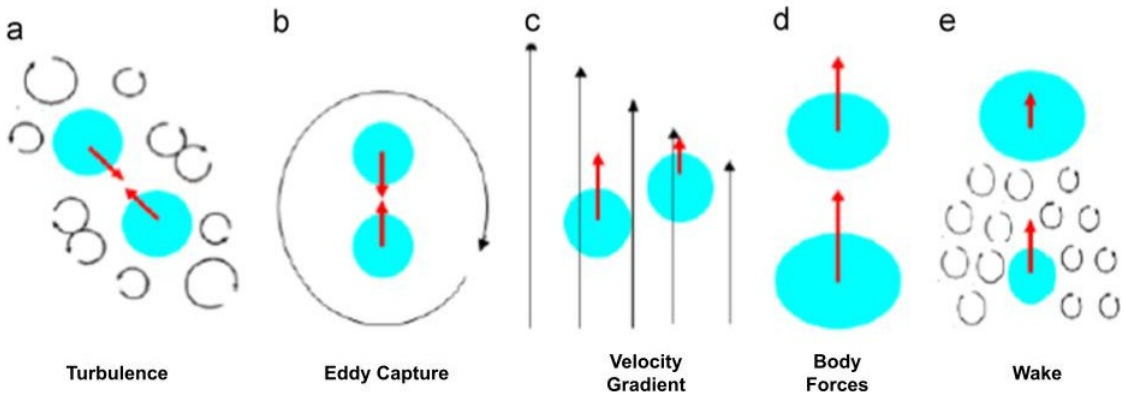

Source: Adapted from (LIAO *et al.*, 2015).

Figure 5 – Representation of the bubble breakup mechanism

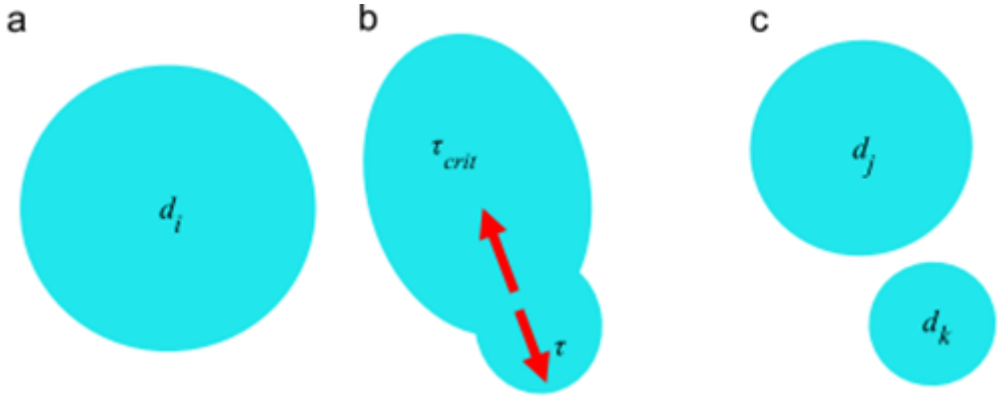

Source: Adapted from (LIAO *et al.*, 2015).

the discretized population balance method, which seeks to discretize the distribution into specific bubble size intervals, providing a detailed description of the bubble size distribution in the flow (LIAO *et al.*, 2015). These models divide the bubbles into size classes and define radial distribution profiles of void fraction for each class. During two-phase flow, different bubble sizes may be generated through the mechanisms of breakup and coalescence (KREPPER *et al.*, 2008). The consequence of this phenomenon is the formation of a range of diameters, each exhibiting distinct behavior when exposed to the interfacial forces present in the flow. As a result of this size variability, the bubble distribution is characterized by groups of bubbles with different diameters (SHANG, 2015).

Figure 6 illustrates an example of bubble class definition in a polydisperse system. Bubbles of the same size, belonging to the same group (m) with diameter equal to (d_m), are grouped together. Each bubble size class is solved throughout the entire flow field by means of transport equations for the size fractions. This method contributes to the understanding of coalescence processes and how they affect the flow dynamics (KREPPER *et al.*, 2008).

The model requires high computational effort due to the large number of differential equations generated for each bubble class (KREPPER *et al.*, 2008). Other models aim to reduce

Figure 6 – Representation of a bubble diameter group in two-phase flow

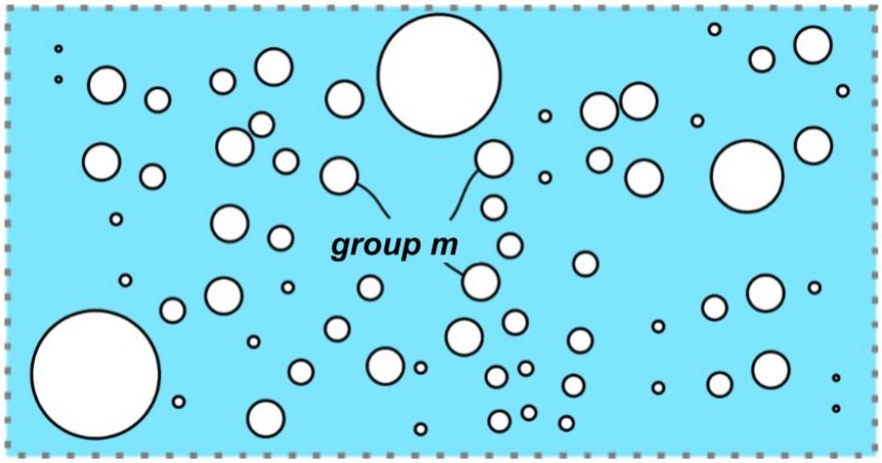

Source: Adapted from (AZEVEDO, 2019).

computational cost, such as the method proposed by Kocamustafaogullari e Ishii (1995), which introduces an additional transport equation for interfacial area concentration, and the method by Hulburt e Katz (1964), which is based on solving the population balance equation through the moments of the bubble size distribution (KREPPER *et al.*, 2008).

The MUSIG model (Multiple Size Group Model) uses separate continuity equations for different bubble size classes, which are solved together with a common momentum equation for the gas phase across all bubble classes. This approach results in the entire gas phase being described by a single velocity field. Consequently, only one momentum equation is used to describe the behavior of the gas phase. As a result, the gas phase is represented by a unified velocity field, which means that the differences in behavior arising from the various bubble sizes, as well as the distinct effects of interfacial forces, cannot be reproduced as they occur in a real two-phase flow. (LUCAS *et al.*, 2007).

For this reason, a non-homogeneous MUSIG model was proposed by Krepper *et al.* (2005), in which different bubble size classes are assigned different velocity fields. With this adaptation, bubbles of varying sizes exhibit distinct behaviors, making the model more realistic in flows where interfacial forces depend on bubble diameter. This method is also referred to as the N*M-MUSIG model, since N velocity classes and M bubble size classes can be considered (LUCAS *et al.*, 2007).

Lucas *et al.* (2001), based on the model by Krepper *et al.* (2005) investigated different velocity fields for each bubble size group using a model with multiple bubble classes, which were later implemented in ANSYS CFX. This non-homogeneous model was based on the homogeneous MUSIG model previously introduced by Lo (1996) in a collaboration between ANSYS CFX and Forschungszentrum Dresden-Rossendorf (KREPPER *et al.*, 2008). These alternative models aim to reduce computational cost. Therefore, the choice of model to be used depends on the specific needs of the study, as well as the balance between the desired accuracy and the available computational resources.

2.5 Experimental Studies

Mat *et al.* (2004) conducted a combined experimental and numerical investigation of two-phase flow in an electrochemical cell with vertical electrodes. The proposed model followed the Eulerian–Eulerian approach, incorporating the effects of interfacial friction, interfacial forces, and electrochemical phenomena such as gas generation via electrolysis reactions. Model validation was performed using an acrylic cell with nickel electrodes, where flow visualization was achieved using microscopy and image analysis. To quantify the void fraction, the authors developed a method based on electrical resistivity measurements between pairs of nickel wires distributed laterally. The results showed that the void fraction increased along the height of the electrode, with bubble accumulation in the upper region, and decreased laterally from the electrode surface, forming an exponential profile.

Figure 7 – Comparison of (a) Image of two phase region (b) measured and (c) calculated void fraction near the electrode

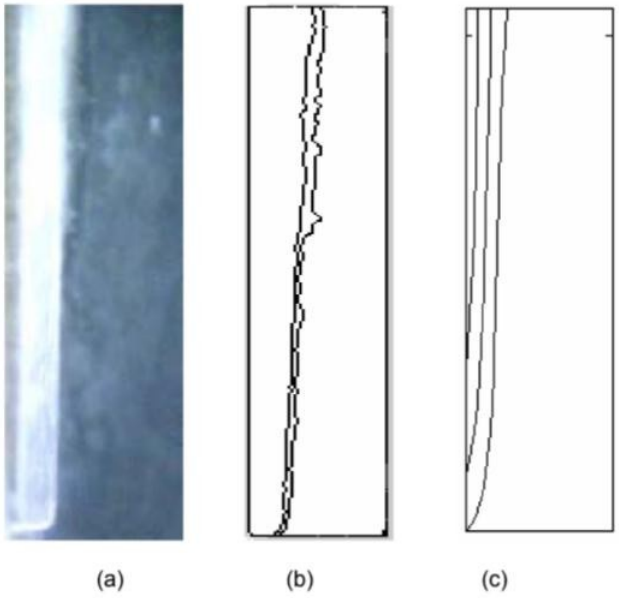

Source: (MAT *et al.*, 2004).

The study also revealed that higher flow rates reduce the residence time of the bubbles, resulting in lower void fractions, a behavior captured both numerically and through measurements using the resistivity system.

Nagai, Ito e Nishijiri (2010) conducted an experimental analysis of two-phase flow between parallel electrodes in an alkaline electrolysis cell. Using high-speed imaging and digital processing, the authors evaluated the influence of parameters such as electrode spacing, membrane presence, and current density on bubble formation and distribution. The results showed that the void fraction increases with increasing electric current, and that bubbles tend to concentrate near the electrodes, especially on the gas-generating side. The presence of a membrane significantly altered the void fraction profile and modified the optimal electrode spacing,

Figure 8 – Effect of electrolyte volumetric flow rate on the hydrogen evolution rate

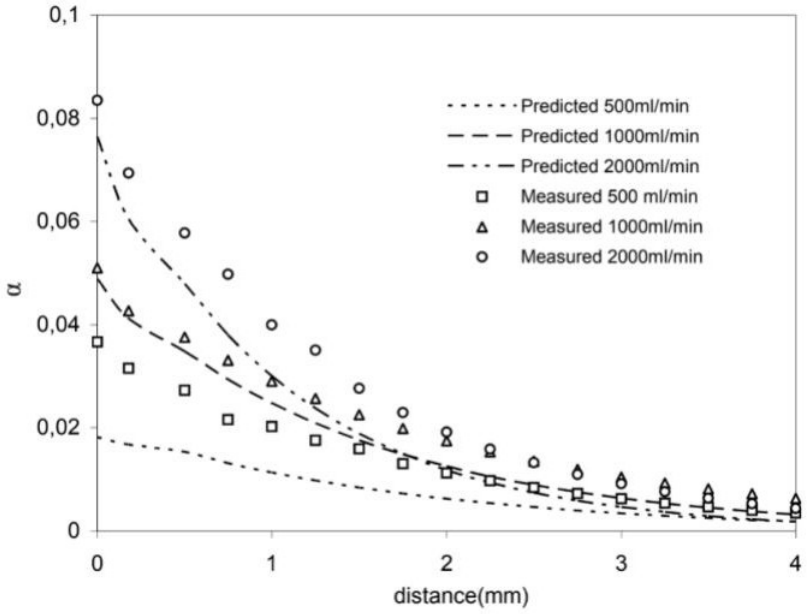

Source: (MAT *et al.*, 2004).

defined as the distance between the anode and cathode that minimizes the electrolyte's electrical resistance and maximizes the efficiency of the electrolysis process, thus influencing both the hydrodynamic behavior and the electrical resistance of the cell.

Ali e Pushpavanam (2011) conducted a detailed analysis of gas–liquid two-phase flow in a rectangular geometry with air injection at the lower right corner. Using particle image velocimetry (PIV) techniques, the authors mapped the velocity field of the liquid phase and compared the results with numerical simulations based on Euler–Eulerian and Euler–Lagrangian models. The experimental setup revealed the formation of a bubble plume capable of inducing circulation in the electrolyte, with upward flow near the gas inlet and downward flow along the opposite wall.

Boissonneau e Byrne (2000) investigated the effects of bubble size, gas flow rate, and channel width on the electrolyte velocity in a rectangular cell with vertical electrodes. The study employed magnified flow visualization via microscopy, laser Doppler velocimetry (LDV), and particle image velocimetry (PIV). The results revealed a transition from laminar to turbulent flow as a result of bubble evolution. It was found that coalescence promotes bubble growth during their migration from the electrode wall toward the interior of the electrolyzer, thereby altering the structure of the gas layer. The interaction of bubbles near the electrode can be divided into three distinct regions. The first zone refers to the adhesion region, located close to the electrode surface, where the bubbles remain attached. The average bubble layer thickness observed in this region was equivalent to the average diameter of the generated bubbles and was thicker at the upper part of the electrodes. The second zone is known as the bubble diffusion region, characterized by a high concentration of bubbles that are visibly larger than those in the adhesion zone. The size growth is attributed to coalescence. This region defines the boundary layer where bub-

Figure 9 – Comparison between experimental and simulated bubble plume patterns: (a) Experimental visualization, (b) Euler–Eulerian simulation, (c) Euler–Lagrangian simulation

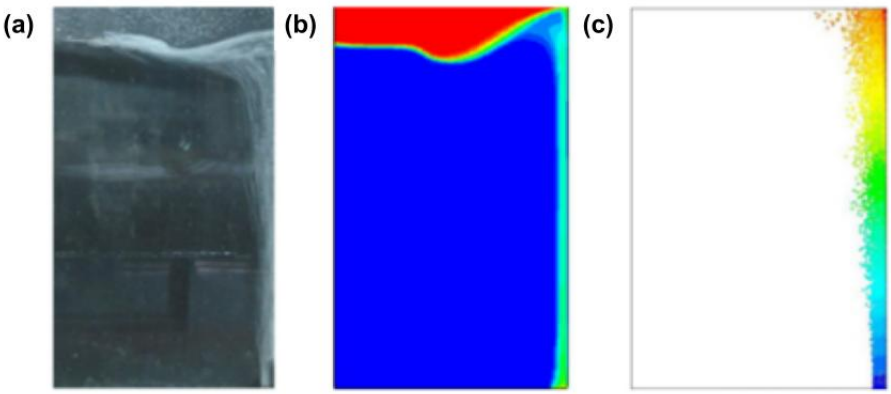

Source: Adapted from (ALI; PUSHPAVANAM, 2011).

bles begin to disperse. The third zone, referred to as the bulk region, contains bubbles that are already well dispersed in the electrolyte. According to the authors, bubbles in this region arrive via the "jumping" mechanism, in which bubbles on the electrode surface coalesce with others in the adhesion zone, forming larger bubbles that jump into the channel interior.

Figure 10 – Representation of bubble behavior regions near the electrode

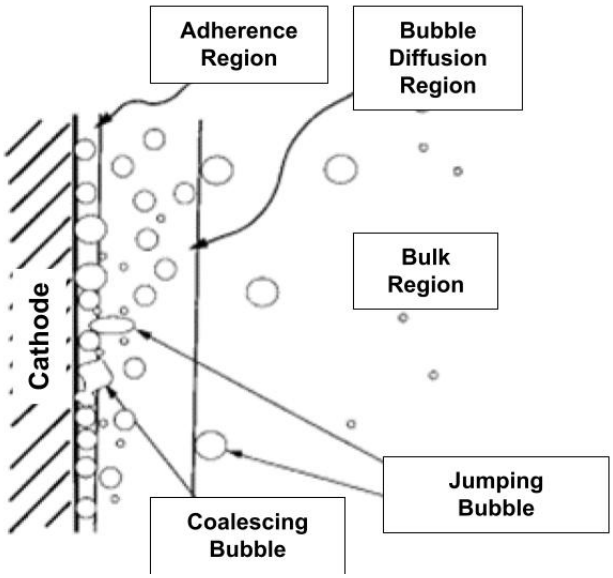

Source: Adaptado de (BOISSONNEAU; BYRNE, 2000).

The study also demonstrated that bubbles of varying diameters were observed along the flow in the electrolyzer, attributed to coalescence processes occurring near the electrode regions. However, after the formation of the bubble layer, the average bubble size stabilizes along

the length of the cell. Figure 11 presents the bubble size distribution observed in the experiment by Boissonneau e Byrne (2000).

Figure 11 – Bubble size distribution in the bulk region

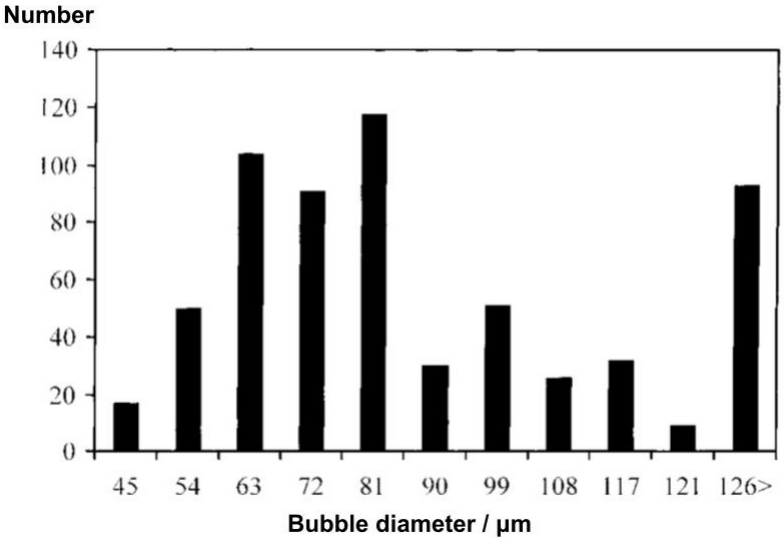

Source: Adaptado de (BOISSONNEAU; BYRNE, 2000).

Bubble dynamics have a significant influence on the evolution of electrolyte flow along the cell. Even when the flow begins with a typical Poiseuille velocity profile (Figure 12a), a progressive flattening of this profile is observed in the center of the cell along the channel (Figure 12b), resulting in a more uniform velocities region, a characteristic of the bulk region. According to Boissonneau e Byrne (2000) , this behavior is caused by bubble-induced turbulence, as bubbles migrate from the wall-adhered region into the channel interior via the jumping mechanism. As the bubbles travel through the electrolyte, vortices and microcurrents are generated, redistributing the liquid and reducing velocity gradients in the central flow region. In Figure 12c, at a higher position in the cell, the onset of the gas-lift effect can also be observed, causing a slight increase in velocities near the electrode.

Figure 12 – Influence of bubbles on the flattening of the electrolyte velocity profile along the electrolyzer

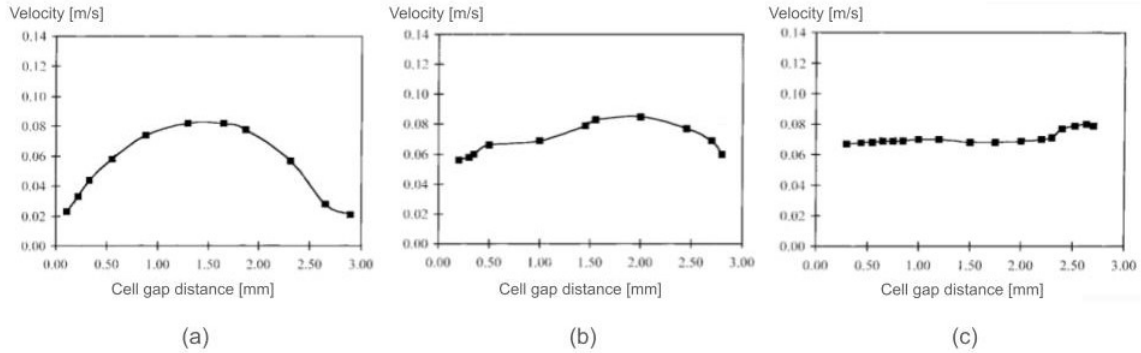

Source: Adaptado de (BOISSONNEAU; BYRNE, 2000).

Liu *et al.* (2024) conducted a detailed experimental investigation into bubble size distribution and detachment mechanisms during alkaline water electrolysis. Using a nickel wire electrode

and high-speed imaging techniques, the authors separately characterized the bubbles generated at the cathode and the anode. The results showed that hydrogen bubbles predominantly had diameters below 60 μm, while oxygen bubbles could exceed 250 μm, with pronounced growth at higher current densities. It was observed that oxygen bubble detachment occurred primarily through the bouncing mechanism, in which a sudden release of surface energy after coalescence generates local disturbances in the concentration boundary layer. This effect is similar to the "jumping" phenomenon previously described by Boissonneau e Byrne (2000). As shown in Figure 13, the average hydrogen bubble detachment diameter increased approximately linearly with current density in the range of 0.15–0.35 A/cm², from about 23 to 29 μm. This trend reflects faster bubble growth and a greater chance of coalescence at higher current densities. The phenomenon has direct implications for gas retention in the electrolyte and mass transfer efficiency, highlighting the importance of understanding growth and detachment regimes for the proper design of electrodes.

Figure 13 – Average hydrogen bubble detachment diameter at different current densities

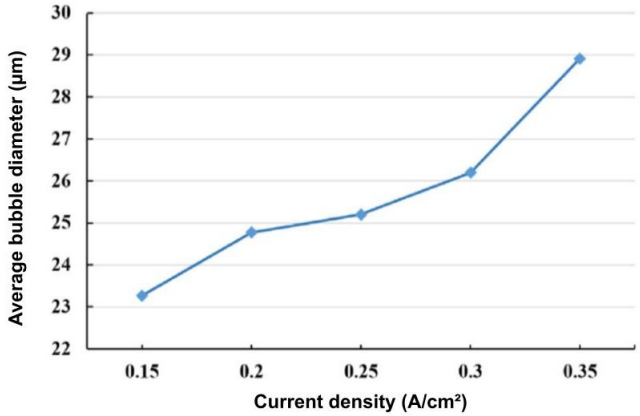

Source: Adaptado de (LIU *et al.*, 2024).

Liu *et al.* (2018) conducted an integrated experimental and numerical investigation of two-phase flow in systems with vertical electrodes, aiming to characterize the three-dimensional velocity field induced by bubble generation. Experimentally, the study employed three-component volumetric velocimetry (V3V), which was used to reconstruct the three-dimensional liquid velocity field based on the tracking of fluorescent particles in the fluid. The results obtained with this technique, as shown in Figure 14, highlight the presence of recirculation structures and zones of high velocity magnitude.

Simultaneously, a three-dimensional CFD model based on the Euler–Euler approach was implemented to simulate the behavior of the two-phase fluid. The results showed that the rise of bubbles intensified turbulence and caused a significant deviation of the liquid flow, forming lateral recirculation structures and promoting mass redistribution within the cell. The comparison between experimental measurements and simulated data showed good agreement, validating the applicability of three-dimensional models for predicting hydrodynamic effects in real electrolyzers.

Figure 14 – Three-dimensional velocity field distribution in the electrolyzer based on experimental data obtained using the V3V technique

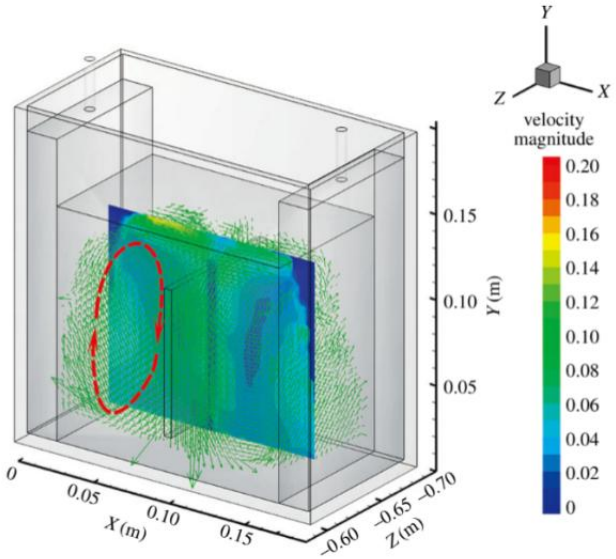

Source: Adaptado de (LIU *et al.*, 2018).

2.6 Numerical Studies

In a two-phase flow, due to interactions between the phases, bubble dynamics result in the spontaneous movement of the electrolyte. As the particles rise, the surrounding fluid is displaced, creating a disturbance in the medium. This movement generates flow in the region around the bubble. This phenomenon, known as the gas-lift configuration, describes the spontaneous motion of the electrolyte induced by bubble ascent. The effect contributes to mixing and circulation of the electrolyte within the electrochemical cell, promoting additional fluid flow (BIDEAU *et al.*, 2020).

Based on a numerical investigation of two-phase flow in electrolyzers, Avci e Toklu (2022) found that the rise velocity of hydrogen bubbles is intrinsically linked to factors such as bubble diameter, electrolyte viscosity, and the densities of both the electrolyte and hydrogen gas. During this process, a significant increase in electrolyte flow velocity was observed as hydrogen bubbles detached from the electrode surface, driven by the gas-lift effect. The authors identified that this effect was directly related to the growth in bubble diameter. The study also found that an increase in void fraction results in a higher bubble rise velocity. Moreover, a higher void fraction corresponds to a larger number of dispersed bubbles. Figure 15, taken from the study by Avci e Toklu (2022), presents a graph showing the variation in electrolyte velocity as a function of hydrogen gas void fraction, as predicted by an analytical model based on drift-flux formulation and force balance.

This behavior, related to the gas-lift effect, suggests that the rise velocity also increases with the bubble concentration. This dynamic occurs due to the gas-lift mechanism, which is strongly dependent on bubble diameter. It is observed that when a large number of bubbles

Figure 15 – Graph of velocity variation as a function of void fraction

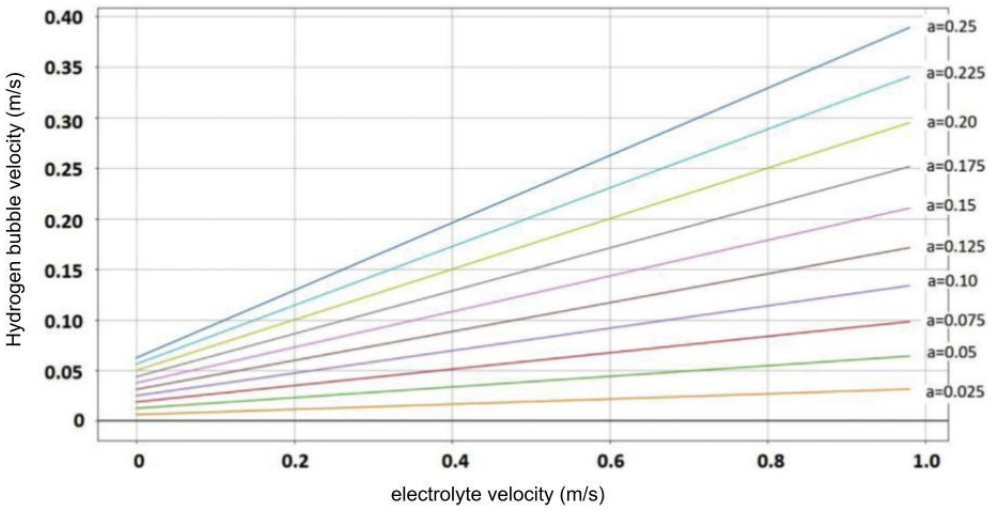

Source: Adaptado de (AVCI; TOKLU, 2022).

are involved, they tend to form a trailing path along the flow, moving sequentially in a row-like pattern. Such organization suggests a clustering dynamic among the rising bubbles, resulting in the formation of distinct bubble lanes along the channel (AVCI; TOKLU, 2022).

In a numerical study, Aldas (2004) evaluated the electrolyte velocity profiles at four different points along the cell to identify the influence of the gas-lift effect. In this work, a two-phase Euler–Euler model was implemented, with drag force as the interfacial momentum exchange term. The simulation setup followed the geometric configuration and operating parameters reported by Boissonneau e Byrne (2000). The author observed an increase in electrolyte velocity near the electrode surfaces, attributed to the gas-lift effect, which refers to the liquid motion induced by the buoyancy-driven rise of bubbles. In this context, the effect is interpreted as a local acceleration of the liquid phase in regions with higher void fraction. The evolution of velocity profiles along the y-axis, as recorded in the study, is shown in Figure 16. Among the four velocity profiles analyzed, the result extracted near the outlet corresponds to the velocity profile at y = 3/4, which exhibited the most pronounced influence of the gas-lift effect. This indicates that near the outlet bubbles have an even more significant effect on the electrolyte velocity.

The numerical modeling of these bubble-induced hydrodynamic effects, as observed in the studies by Avci e Toklu (2022) and Aldas (2004), requires consideration of interfacial forces that govern the interaction between phases. Among these forces, the drag force plays a central role, as it quantifies the resistance imposed by the continuous fluid on the upward motion of the bubbles. Some authors have adopted this approach as a starting point for Euler–Euler modeling, assuming that the drag force alone would be sufficient to represent the vertical gas dynamics and the gas-lift mechanism observed experimentally.

Accordingly, the numerical studies of Jupudi *et al.* (2009) and Zhan *et al.* (2017b) have opted for simplified models based exclusively on F_D, aiming to capture the essence of the two-

Figure 16 – Electrolyte velocity profile at different vertical positions y of the electrolysis cell

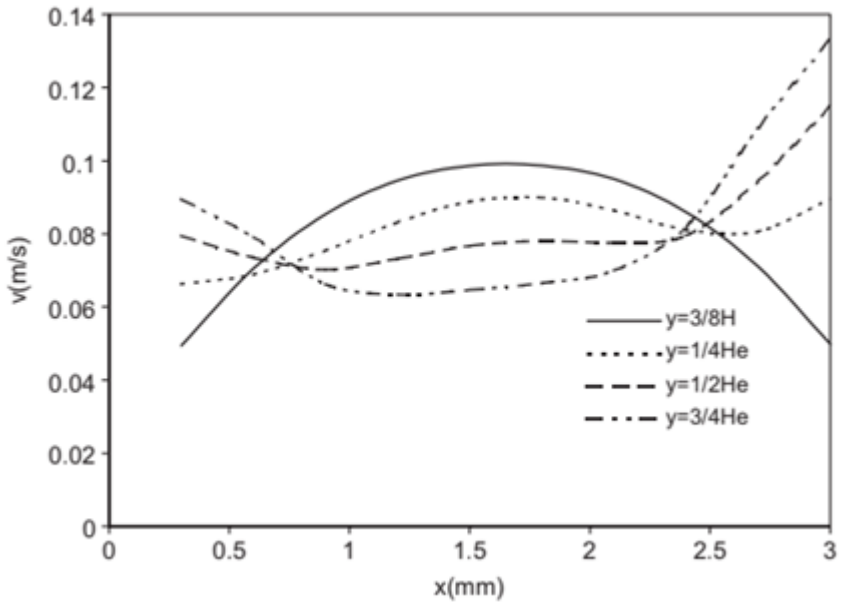

Source: (ALDAS, 2004).

phase flow driven by gas phase rise. Jupudi *et al.* (2009) conducted a combined numerical and experimental study to investigate current density and bubble distribution in an alkaline electrolysis cell, emphasizing the dominant role of the resistance imposed by the liquid phase on gas dynamics. A two-dimensional Euler–Euler model was developed to simulate the multiphase flow, incorporating electrochemical equations to account for electrode overpotential, including the reduction of active surface area due to bubble coverage. Separate mass and momentum conservation equations were solved for each phase, with the drag force as the interfacial momentum exchange term. The numerical results were validated against experiments performed on a 5” $\times$ 5” parallel-plate cell equipped with a Raney nickel cathode and a stainless steel anode, operating with a 30% KOH electrolyte at 20–60 ℃ and inlet flow rates up to 2 L/min.

As shown in Figure 17 the numerical results illustrate the distribution of hydrogen gas volume fraction throughout the simulated domain. From the volume fraction contours (a) and the curves at four distinct positions (b), it can be observed that drag-force-only models can predict the dispersed-phase gradient, where the gas fraction near the electrode tends to increase along the vertical flow.

Similarly, Zhan *et al.* (2017b) highlighted that for two-phase flows in aluminum electrolysis cells, models based on drag force are widely adopted due to their predominant role over non-drag interfacial forces, such as lift, wall lubrication, and virtual mass forces.

Subsequently, Abdelouahed *et al.* (2014b) developed an Euler–Euler model incorporating interfacial forces such as drag, lift, and virtual mass to numerically simulate and validate results against measurements obtained with the experimental unit described in Abdelouahed *et al.* (2014a). Figure 18 presents the predicted phase velocity contours (left) and gas volume fraction contours (right), showing a front view of the cell, where the left and right sides corre-

Figure 17 – Illustration of gas volume fraction variation at different positions along the Y-axis of the electrolysis cell

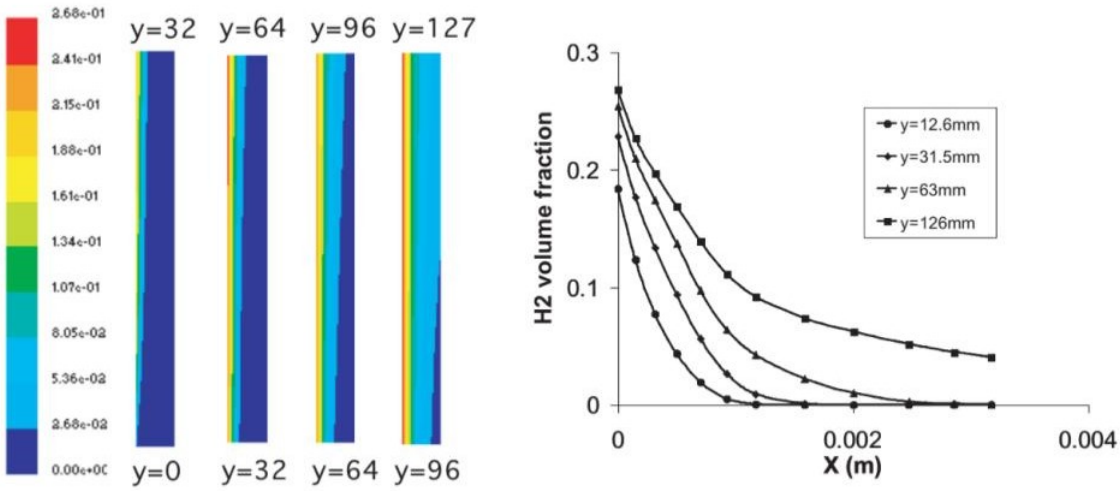

Source: (JUPUDI *et al.*, 2009).

spond to the electrodes generating gas. It can be observed that the regions with the highest void fraction, where bubbles are detaching from the electrodes, are also those with the highest rise velocities. Electrolyte velocity decreases in the central region of the gap, with bubbles in the central flow having lower absolute velocity than those near the electrode surfaces. However, the authors noted that the model did not adequately reproduce bubble dispersion, suggesting that a turbulent dispersion force should be included, as it may play a major role in the expansion and redistribution of the bubble swarm.

Figure 18 – Contours of bubble velocity and void fraction in an electrolysis cell

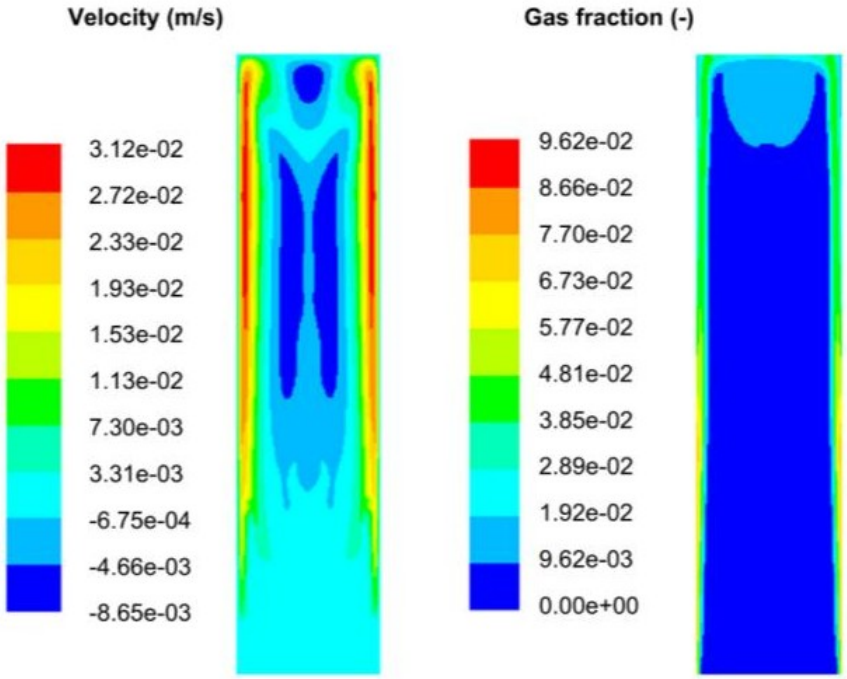

Source: (ABDELOUAHED *et al.*, 2014b).

Based on these findings, Bideau *et al.* (2020) included a turbulent dispersion force in their Euler–Euler model and applied it to replicate the experiments of Boissonneau e Byrne (2000). They observed that high bubble concentrations intensified the dispersion phenomenon, redistributing bubbles from high- to low-concentration regions. The additional force was inspired by formulations proposed by Marfaing *et al.* (2016) and Davidson (2014) in similar Euler–Euler approaches. This modification allowed for a more accurate reproduction of the experimental behavior, especially in regions with high bubble concentration.

Other studies have also chosen to incorporate the turbulent dispersion force into their models, recognizing its key role in representing bubble redistribution effects, especially in systems where the gas-lift effect is significant. This additional force enables more accurate modeling of the transverse transport of bubbles, driven by turbulent fluctuations in the electrolyte, and its resulting influence on the continuous phase velocity field. In this context, Zhang *et al.* (2023) and Li *et al.* (2024) simultaneously adopted both drag and turbulent dispersion force in their models to better capture bubble dispersion.

Zhang *et al.* (2023) simulated flow in concave–convex channels for alkaline electrolyzers, showing that the inclusion of F_{TD} was crucial for accurately predicting gas volume fraction distribution. Li *et al.* (2024), in turn, studied bubble coverage on electrodes and how it can influence local electrolyte flow, free bubble distribution, and the velocity field within the electrolyzer. The authors found that the turbulent dispersion force helps to smooth out sharp gradients in gas volume fraction caused by the non-uniform distribution of bubbles inside the cell.

Due to the scarcity of studies that employ more complex models to simulate bubbly flows in alkaline water electrolyzers, it becomes relevant to turn to related literature, such as aluminum electrolysis, which examines the same interfacial interaction phenomena in a two-phase flow. In this context, Zhan *et al.* (2017a) stood out by implementing a three-dimensional CFD model coupled with a Population Balance Model (PBM) to describe the gas-liquid two-phase flow behavior in aluminum electrolysis cells. The authors conducted a comprehensive analysis involving interfacial forces, such as drag force , lift force, turbulent dispersion force, and wall lubrication force, in addition to turbulence models, including the bubble-induced turbulence model proposed by Sato e Sekoguchi (1975).

It was found that although (F_D) plays a dominant role in momentum transfer between the phases, the inclusion of (F_{TD}) led to significant improvements in predicting the electrolyte velocity profile. On the other hand, forces such as (F_L), (F_{VM}), and (F_{WL}) had a reduced impact on the overall hydrodynamics and could, in some cases, be neglected without compromising model accuracy.

The study also aimed to evaluate the impact of bubble size distribution through the implementation of the PBM model with coalescence and breakup mechanisms proposed by Luo e Svendsen (1996). The results showed that the CFD–PBM coupling enables a more realistic representation of two-phase dynamics due to the polydisperse behavior with different bubble diameters, being capable of adequately capturing bubble–bubble interactions. It was observed

that coalescence predominated under the anodes, a region with high gas fraction and low turbulence, while bubble breakup became more relevant in regions with higher velocity gradients, where turbulent energy dissipation is greater. The study highlighted the importance of explicitly considering coalescence and breakup mechanisms in simulations of large-scale electrolyzers. Moreover, it reinforces that monodisperse flow assumptions are inadequate when aiming to represent complex gas-lift effects and bubble–bubble interactions in high gas concentration regions.

Other complementary studies have also addressed phenomena such as coalescence and electrode coverage, such as the work by Xu *et al.* (2022), who conducted a numerical simulation in a micro–nanobubble generator using a CFD–PBM model coupled with coalescence and breakup models. The study analyzed the gas–liquid two-phase flow in a cyclone jet flotation cell, with a bubble size distribution ranging from 0.99 to 140 μm. The results showed that, throughout the flow inside the generator, larger bubbles located in the center of the tube fragmented into smaller bubbles, which migrated toward the periphery. Later, these smaller bubbles regrouped, forming larger bubbles near the outlet. It was observed that bubble breakup dominated in the central regions, while coalescence became dominant at the periphery, indicating a dynamic equilibrium between the two phenomena along the flow path. The average bubble diameter gradually increased from 30 to 110 μm, with a more pronounced growth between sections 2 and 4 of the channel, as illustrated in Figure 19. Although the system does not directly represent an electrolyzer, the work clearly illustrates the potential of CFD–PBM coupling to model bubble evolution processes in complex two-phase flows.

Figure 19 – Geometry of the study and bubble diameter distribution map at an inlet flow velocity of 6.5 m/s

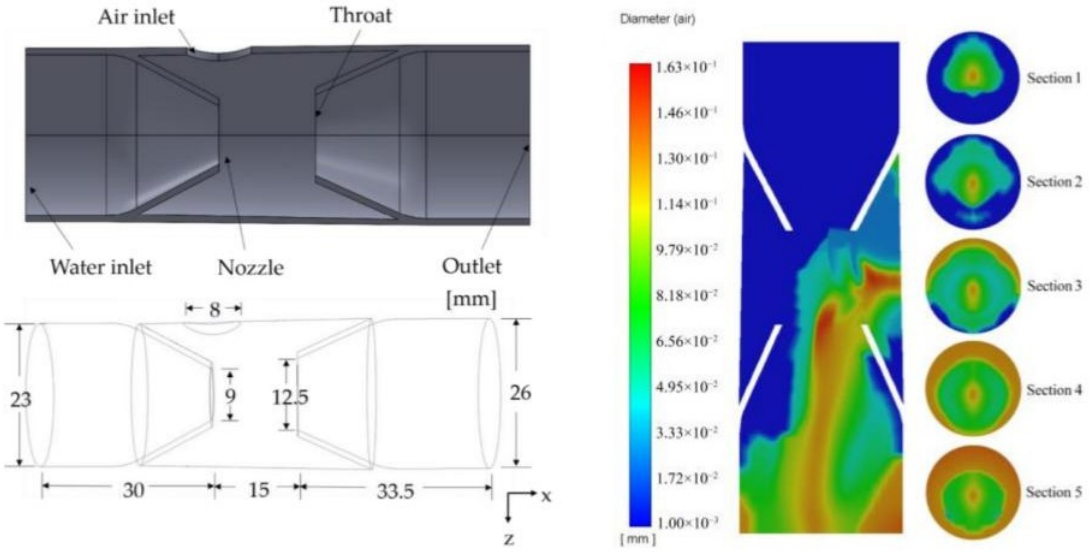

Source: Adapted from (XU *et al.*, 2022).

Finally, it is worth highlighting the study by Liao *et al.* (2015), who proposed an update to the polydisperse MUSIG model (Multiple Size Group Model) through its implementation as a

discrete version of the Population Balance Model (PBM) in fixed size groups within the ANSYS CFX software, aiming to improve the reliability of bubble behavior predictions in two-phase flows.

The experimental data used by Liao *et al.* (2015) were obtained from the MTLoop and TOPFLOW facilities at HZDR (Germany), which are dedicated to the study of two-phase flows in vertical columns. While MTLoop is characterized by the injection of small bubbles that grow by coalescence, TOPFLOW simulates scenarios with the injection of larger bubbles and predominant breakup along the column, due to high turbulent energy. The authors identified that traditional coalescence and breakup models, based on global averages of energy dissipation, presented limitations in capturing local interactions between bubbles of different sizes.

In conventional bubble coalescence and breakup models used in CFD–PBM simulations (such as those implemented in the original MUSIG), the turbulent energy dissipation rate (ε) is generally taken as an average value over the domain or over entire mesh regions (e.g., a cell or group of cells). This approach neglects the local fluctuations that occur around the bubbles, especially in regions with high anisotropy or strong turbulence gradients.

To overcome these limitations, the authors proposed a reformulation of the PBM equations to incorporate local turbulence effects, implementing new coalescence and breakup kernels.The new model was validated with experimental data of upward flow in pipes and showed improved performance over the conventional MUSIG model, particularly in predicting the Sauter mean diameter (d_{32}), a statistical measure describing the ratio between volume and surface area of a particle or bubble distribution, and the axial bubble distribution.

This approach represents a significant advancement in the modeling of gas-evolving two-phase systems and provides a solid foundation for implementing more robust bubble distribution models.

2.7 Closing Remarks of the Literature Review

Although alkaline water electrolysis is a well-established hydrogen production technology, it still presents operational bottlenecks related to two-phase flow dynamics and the presence of gas bubbles. This review has shown that the hydrodynamic behavior of electrolyzers is strongly influenced by the generation, growth, coalescence, breakup, and transport of gas bubbles in the electrolyte. Initially, the importance of the ohmic resistance caused by gas bubbles was highlighted as a limiting factor for the energy efficiency of the process, being modeled through Bruggeman's equation and validated by experimental studies (JANSSEN, 2000; MANDIN *et al.*, 2014). This resistance is directly associated with the void fraction and the difficulty in removing bubbles from the electrode surface.

From a numerical point of view, Euler-Euler models have become established as robust tools for simulating two-phase flow in electrolyzers, allowing for the incorporation of multiple interfacial forces. Among these, the most prominent are drag force, lift force, virtual mass force, wall lubrication force, and turbulent dispersion force. A critical review of the studies revealed

that, although some studies have adopted the use of only F_D in their models due to its dominant role in momentum transfer, its isolated application may be insufficient to reproduce the patterns observed experimentally. This was demonstrated in the works of Abdelouahed *et al.* (2014b) and Bideau *et al.* (2020). Another relevant point concerns the need to accurately represent the actual distribution of bubble sizes, since the monodisperse approach limits the precision of simulations. Polydisperse models, particularly the MUSIG and its non-homogeneous variants, have been proposed to overcome these limitations, enabling a more realistic capture of coalescence and breakup effects along the electrolysis channel. The integration of CFD with the Population Balance Model (PBM) has proven promising, as evidenced by (ZHAN *et al.*, 2017a; LIAO *et al.*, 2015), in describing the evolution of bubble size and the transition regimes observed experimentally.

Based on the insights gained from the literature review, the modeling strategy adopted in this work will combine a polydisperse Euler–Euler approach with the non-homogeneous MUSIG model, coupled with population balance equations for bubble breakup and coalescence. As demonstrated in the reviewed studies, the drag force plays a fundamental role in two-phase flow; however, other forces such as lift, wall lubrication, virtual mass, and especially turbulent dispersion have also proven to be critical for reproducing experimentally observed patterns. All these forces will be tested to evaluate their influence within the scope of this work, and the most relevant ones will be incorporated into the final model. Table 2 presents a summary of the studies discussed in the Experimental Studies and Numerical Studies sections.

Table 2 – Summary of Literature on Two-Phase Flow Modeling in Electrochemical and Related Systems

No.	Reference	Theme	Study Type	Model	Dispersion Type	Interfacial Forces	PBM	Coalescence	Break-up
1	(ALDAS *et al.*, 2008)	Alkaline Water Electrolysis	Numerical and Experimental	Euler–Euler	Monodisperse	Drag	—	—	—
2	(NAGAI; ITO; NISHIJIRI, 2010)	Alkaline Water Electrolysis	Experimental	—	—	—	—	—	—
3	(ALI; PUSHPAVANAM, 2011)	Gas–Liquid Flows in a Rectangular Tank	Numerical and Experimental	Euler–Euler and Euler–Lagrange	Monodisperse	Drag	—	—	—
4	(BOISSONNEAU; BYRNE, 2000)	Alkaline Water Electrolysis	Experimental	—	—	—	—	—	—
5	(LIU *et al.*, 2024)	Alkaline Water Electrolysis	Experimental	—	—	—	—	—	—
6	(LIU *et al.*, 2024)	Alkaline Water Electrolysis	Numerical and Experimental	Euler–Euler	Monodisperse	Drag - Turbulent Dispersion	—	—	—
7	(AVCI; TOKLU, 2022)	Alkaline Water Electrolysis	Analytic	Homogeneous / Drift-Flux	Monodisperse	Drag - Lift	—	—	—
8	(ALDAS, 2004)	Alkaline Water Electrolysis	Numerical	Euler–Euler	Monodisperse	Drag	—	—	—
9	(JUPUDI *et al.*, 2009)	Alkaline Water Electrolysis	Numerical and Experimental	Euler–Euler	Monodisperse	Drag	—	—	—
10	(ZHAN *et al.*, 2017b)	Aluminum Electrolysis Cells	Numerical	Euler–Euler	Monodisperse	Drag - Lift - Wall Lubrication - Turbulent Dispersion	—	—	—
11	(ABDELOUAHED *et al.*, 2014b)	Alkaline Water Electrolysis	Numerical and Experimental	Euler–Euler	Monodisperse	Drag - Lift - Virtual Mass	—	—	—

Continued on next page

No.	Reference	Theme	Study Type	Model	Dispersion Type	Interfacial Forces	PBM	Coalescence	Break-up
12	(BIDEAU *et al.*, 2020)	Alkaline Water Electrolysis	Numerical	Euler–Euler	Monodisperse	Drag - Lift - Turbulent Dispersion	—	—	—
13	(MARFAING *et al.*, 2016)	Bubbly Flow in Vertical Pipe	Numerical and Analytical	Euler–Euler	Monodisperse	Drag - Lift - Wall Lubrification - Turbulent Dispersion	—	—	—
14	(ZHANG *et al.*, 2023)	Alkaline Water Electrolysis	Numerical	Euler–Euler	Monodisperse	Drag - Turbulent Dispersion	—	—	—
15	(LI *et al.*, 2024)	Alkaline Water Electrolysis	Numerical	Euler–Euler	Monodisperse	Drag - Lift - Virtual Mass	—	—	—
16	(DAVIDSON, 2014)	Gas Injection in Liquid Bath	Numerical	Euler–Euler	Monodisperse	Drag - Lift - Virtual Mass - Turbulent Dispersion	—	—	—
17	(ZHAN *et al.*, 2017a)	Aluminum Electrolysis Cells	Numerical	Euler–Euler	Polydisperse	Drag - Turbulent Dispersion	Yes	Yes	Yes
18	(XU *et al.*, 2022)	Bubble generation in micro-nanobubble generator	Numerical	Euler–Euler and PBM	Polydisperse	Drag - Lift - Virtual Mass	Yes	Yes	Yes
19	(LIAO *et al.*, 2015)	Vertical Bubbly Pipe Flow	Numerical	Euler–Euler and PBM	Polydisperse	Drag - Lift - Wall Lubrification - Turbulent Dispersion	Yes	Yes	Yes

3 MATERIALS AND METHODS

Based on an electrolyzer geometry, two-fluid type mathematical models proposed in the literature were applied to simulate the electrolyte–hydrogen two-phase flow. In this approach, the electrochemical hydrogen generation process was not explicitly modelled; instead, a uniform hydrogen distribution at the inlet was assumed, considering that local void fraction variations do not affect hydrogen production. This simplification allows the study to focus on the hydrodynamic behaviour of the phases and the influence of interfacial forces, without the additional complexity of coupling electrochemical reaction kinetics.

The geometry used in the analysis was based on an experimental study conducted by TU Clausthal – Technische Universität Clausthal in Germany. Figure 20 shows a photograph of the electrolyzer developed by the laboratory and also an exploded view of the prototype components. The experimental unit consists of a bipartite acrylic structure with internal compartments for water electrolysis. The hydrogen and oxygen compartments have electrodes on the external sides and, when assembled, are separated by an impermeable membrane that allows only ion transport.

Figure 20 – Experimental unit of the hydrogen production cell developed at TU Clausthal

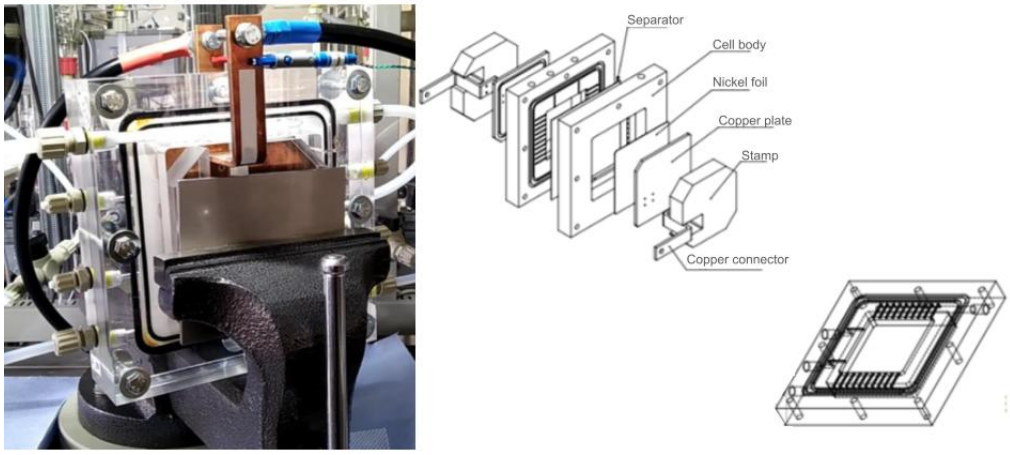

Source: Author.

Each side of the electrolyzer contains two cylindrical channels, with the lower one used for electrolyte inlet and the upper one for the outlet of products generated during electrolysis. Each cylindrical channel has ten branches distributed along the compartment where gas production occurs, and the products are also directed out of the cell through ten identical outlets, as demonstrated by Figure 21. The internal dimensions in which the electrolyte flows were extracted from this model. A system model was then built to represent the flow regions, focusing exclusively on the hydrogen production region. Since the study aims at evaluating the performance of hydrogen

gas production, only the phenomena occurring in the hydrogen compartment were considered and the oxygen gas production region was not included in the simulation.

Figure 21 – Representation of the flow region for the phases

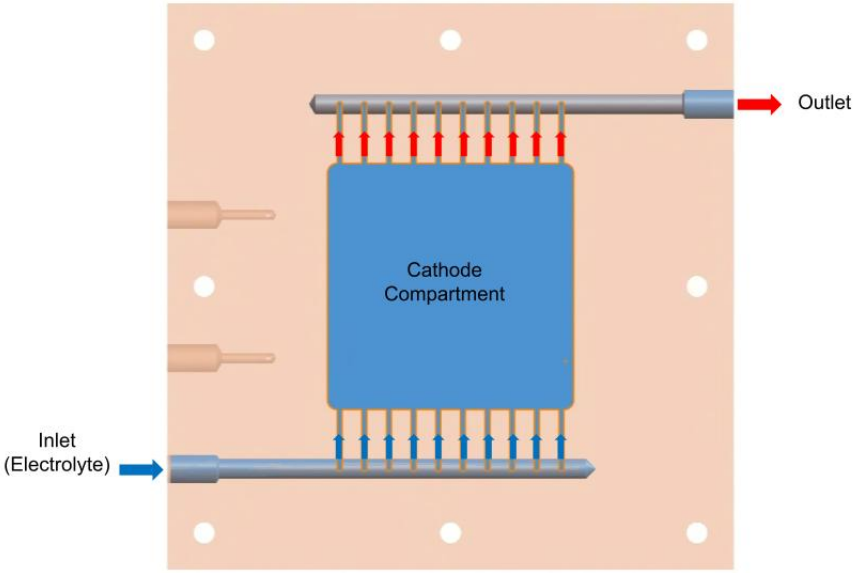

Source: Author.

Due to the complexity of the original geometry and the high computational cost required to model the two-phase flow throughout the entire cell, the system was simplified. The component was divided into 10 identical sections, each containing one inlet and one outlet channel. This strategy reduces computational cost. Figure 22a. shows, with red dashed lines, the simplified region of the geometry considered in the current study. The test section has a height “H,” width “L,” and thickness “T,” as illustrated in Figure 22b. The square inlet and outlet channels have a side length “a.” Since only one channel was simulated, symmetry boundary conditions were applied to the lateral faces, representing the influence of the adjacent sections.

The electrolyte enters the lower part of the test section through the square inlet channel, while hydrogen gas is injected in the back wall. The products of the process (hydrogen bubbles and electrolyte) exit via a square outlet channel, as shown in Figure 23.

3.1 Mathematical Model

The mathematical model to simulate the gas–liquid two-phase flow is here presented. The model is divided into fundamental equations applied for both single and two-phase flow models, the constitutive equations that describe the interfacial forces between the two phases, the polydisperse model, along with the mechanisms used to predict bubble coalescence and breakup rates.

Figure 22 – Simplified representation of the geometry

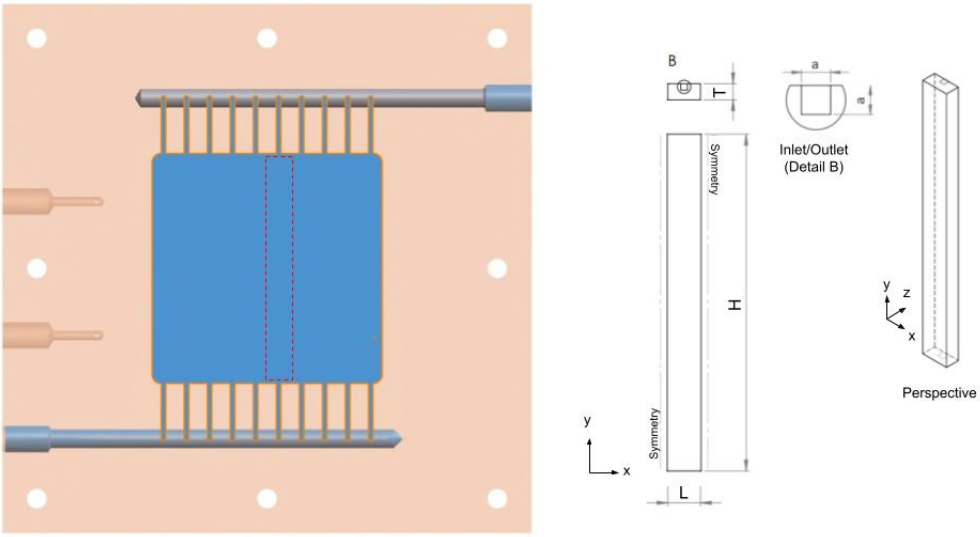

Source: Author.

Figure 23 – Representation of inlet and outlet conditions

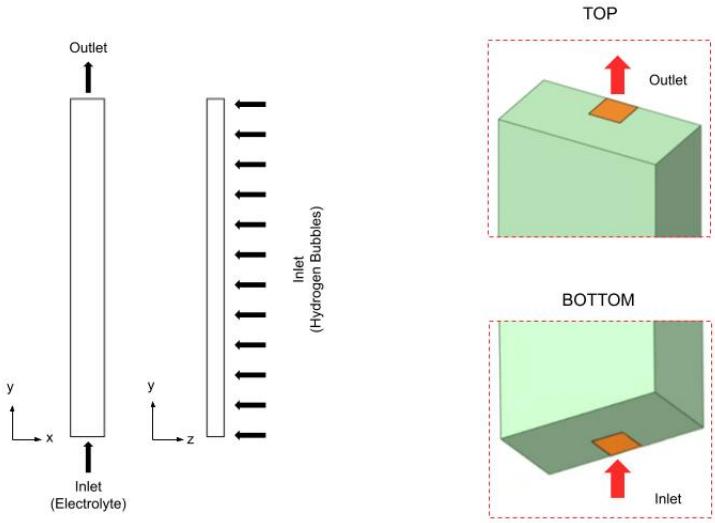

Source: Author.

3.1.1 Single-Phase Flow Model

Initially, a single-phase flow in a rectangular channel geometry is considered in order to establish a baseline for comparison with the two-phase flow case and to evaluate the influence of bubbles on the hydrodynamics. The flow is assumed Newtonian, viscous, and incompressible. Due to the low inlet velocity of the electrolyte (50 mL/min), the Reynolds number for the rectangular channel is 117, which characterizes the flow as laminar.

The simulations were carried out under steady-state conditions with the aim of identifying the flow behavior without variations in fluid properties over time, allowing the observation of characteristics such as velocity distribution and changes in the velocity profile regardless of time.

To conduct the analysis, it is essential to establish the equations that represent the flow. The modeling is based on the fundamental equations of mass and momentum conservation. The continuum hypothesis is assumed, which considers the fluid as a continuous and homogeneous medium:
Mass conservation equation

$$\nabla \cdot \vec{V}_{xyz} = 0 \tag{11}$$

Momentum conservation equation

$$\nabla \cdot (\rho \vec{V}_{xyz} \vec{V}_{xyz}) = -\nabla \cdot p + \mu \nabla^2 \vec{V}_{xyz} + \rho g \tag{12}$$

Where the left-hand side of Equation (11) represents the divergence of the velocity field. Considering the fluid as incompressible, its density does not vary in time or space. As a result, the divergence of the velocity field is zero in the continuity Equation (11). In Equation (12), the left-hand side represents the divergence of the momentum flux, where ρ is the fluid density and $\vec{V}_{xyz}$ is the velocity vector. On the right-hand side. The first term, $-\nabla \cdot p$, corresponds to the pressure gradient force, responsible for accelerating or decelerating the fluid due to pressure differences in the domain. The second term, $\mu \nabla^2 \vec{V}_{xyz}$, represents the viscous diffusion term, which models the momentum transport caused by internal friction between fluid layers, where μ is the dynamic viscosity. The last term, $\rho \vec{g}$, corresponds to the body force due to gravity, acting uniformly on the fluid mass and responsible for effects such as buoyancy when density differences are present.

3.1.2 Two-Phase Flow Model

The numerical simulation of two-phase flow requires a model capable of representing how the phases behave within the medium and how they interact with each other. A non-homogeneous Eulerian–Eulerian approach, known as the two-fluid model, is employed in the current study. This formulation treats each phase separately, allowing for a more detailed prediction of interfacial phenomena compared to mixture models, as mass, momentum, and energy transfer processes are expressed independently for each phase. Each phase is denoted by k, where $k = l$ represents the continuous phase and $k = g$ the dispersed phase (ISHII; HIBIKI, 2006). The mass and momentum conservation equations for the two-phase flow were also formulated under steady-state conditions. The governing equations for phase k are presented below:
Mass conservation equation

$$\nabla \cdot \left(\alpha_k \rho_k \vec{V}_k \right) = 0 \tag{13}$$

Momentum conservation equation

$$\nabla \cdot \left(\alpha_k \rho_k \vec{V}_k \vec{V}_k\right) = -\nabla \cdot (\alpha_k P_k) + \nabla \cdot \left(\alpha_k \mu_{eff,k} \left(\nabla \vec{V}_k + (\nabla \vec{V}_k)^T\right)\right) + \alpha_k \rho_k \vec{g} + M_k \tag{14}$$

The term on the left-hand side of Equation 13 represents the divergence of the mass flux of phase k while the right-hand side corresponds to the mass exchange between phases. In Equation 14, the term M_k represents the interfacial interaction force per unit volume between the continuous phase l and the dispersed phase g. This term incorporates the different interfacial forces into the model. The interaction forces include the lift force F_L, the drag force F_D, the wall lubrication force F_{WL} the virtual mass force F_{VM} and the force generated by turbulent dispersion F_{TD}.

3.1.3 Interfacial Forces

Equation 15 presents the forces that compose the momentum exchange term between the phases:

$$\vec{M_k} = \alpha_k \frac{\left(\vec{F}_D + \vec{F}_L + \vec{F}_{WL} + \vec{F}_{VM} + \vec{F}_{TD}\right)}{V_p} \tag{15}$$

3.1.3.1 Drag Force

The first force coupled to the model is the drag force, which represents the resistance experienced by the particle during its movement through the continuous medium and is defined by the relative velocity between the particle and the continuous phase, given by:

$$\vec{F}_D = -\frac{1}{8} C_D A_k \rho_l (\vec{v}_g - \vec{v}_l)|\vec{v}_g - \vec{v}_l| \tag{16}$$

where C_D is the drag coefficient, A_k is the specific interfacial area of the bubble, and the difference between the gas and liquid phase velocities ($\vec{v}_g - \vec{v}_l$) represents the relative velocity. The drag coefficient depends on the Reynolds number for spherical bubbles (Re_b) and on the Eötvös (E_o) and Morton (M_o) numbers for non-spherical bubbles. The Eötvös and Morton numbers act together to determine the bubble shape. In fluids with low M_o, bubbles are more likely to become elongated, even at low (E_o) values. The drag coefficient is defined based on the model proposed by CLIFT *et al.* (1978), which describes the tendency of bubbles to deform when exposed to the stresses generated in the flow (ROSA, 2012). The equations that define this model are shown below:

$$\mathsf{Re}_b = \frac{\rho_l d_b |\vec{v}_g - \vec{v}_l|}{\mu_l} \tag{17}$$

$$C_{(D,\mathsf{sphere})} = \max\left[\frac{24}{\mathsf{Re}_b}\left(1 + 0.15\mathsf{Re}_b^{0.687}\right); 0.44\right] \tag{18}$$

$$C_{(D,\mathsf{ellipse})} = \frac{4 g d_b (\rho_l - \rho_g)}{3 U_t^2 \rho_l} \tag{19}$$

$$U_t = \frac{\mu_l}{\rho_l d_b} M_o^{-0.149} (J - 0.857) \tag{20}$$

$$J = \begin{cases} 0.94 G^{0.757} & \text{if } 2 < G \leq 59.3 \\ 3.42 G^{0.441} & \text{if } G > 59.3 \end{cases} \tag{21}$$

$$G = \frac{4}{3} E_o M_o^{-0.149} \left(\frac{\mu_l}{0.0009}\right) \tag{22}$$

$$E_o = \frac{g(\rho_l - \rho_g) d_b^2}{\sigma} \tag{23}$$

$$M_o = \frac{g \mu_l^4 (\rho_l - \rho_g)}{\rho_l^2 \sigma^3} \tag{24}$$

In Equation 17, Re_b is the Reynolds number of the bubble, ρ_k is the density of the continuous phase, d_b is the bubble diameter, and μ_l is the dynamic viscosity of the continuous phase. In Equation 18, $C_{D,sphere}$, sphere is the drag coefficient for a spherical bubble, which may vary between the empirical formula used for low and moderate flow velocities and the constant value of 0.44 , which corresponds to the drag coefficient for high Re_b. In Equation 19, $C_{D,ellipse}$ represents the drag coefficient for an ellipsoidal bubble, where g is the gravitational acceleration, d_b is the bubble diameter, and U_t is the terminal velocity of the bubble. Equation 20 calculates the maximum velocity the bubble can reach as it moves through the continuous phase, the terminal velocity. It depends on the Morton number (M_o) and the dimensionless parameter J, which is related to the value of the function G.The parameter is defined in Equations 21 and 22, where G is a function depending on the Eötvös number (E_o) and Morton number (M_o), as well as on the dynamic viscosity of the continuous phase. Finally, Equations 23 and 24 define the Eötvös number (E_o) and Morton number (M_o) respectively.

Additionally, a correction for bubble packing was applied through the Volume Fraction Correction Exponent parameter, which adjusts the value of C_D as a function of the local gas volume fraction α_g. In this work, an exponent of -1 was used, corresponding to a correction of the form $C_D^{\text{eff}} = C_D(1-\alpha_g)^{-1}$. This value in the current work was fitted to the experimental results presented by Rodríguez e Amores (2020), as discussed in the next section. The correction increases the drag coefficient in high bubble concentration regions, reflecting the increased resistance to gas-phase motion due to interfacial interactions. Another essential factor in modeling the drag force is the interfacial area density A_k, which is defined as the ratio of the bubble surface area to its volume, multiplied by the gas volume fraction α_g.

$$A_k = \alpha_g \left(\frac{\pi d_b^2}{\pi d_b^3/6} \right) = 6 \left(\frac{\alpha_g}{d_b} \right) \tag{25}$$

According to ANSYS, Inc. (2019)), a high gas volume fraction leads to physical inconsistencies and numerical instabilities in the simulation. Since the interfacial area density is inversely proportional to the bubble diameter, it is important to consider the concept of maximum bubble packing, which defines the upper limit of the volume fraction in a dispersed flow regime (AZEVEDO, 2019). Based on ANSYS, Inc. (2019) guidelines, for α_k values above 0.8, bubbles become so closely packed that the flow can no longer be characterized as dispersed, as the separation between bubbles disappears and the medium behaves as a continuous gas phase.

3.1.3.2 Lift Force

The second force is the lift force, which is associated with the translational motion of a bubble in a viscous flow with an asymmetric velocity field around it. This phenomenon generates a force that displaces the bubble laterally. The expression that defines the force is shown below:

$$\vec{F}_L = -C_L \rho_l \left(\vec{v}_g - \vec{v}_l \right) \times \text{rot}(\vec{v}_l) \tag{26}$$

The term C_L represents the lift coefficient, and rot(v_l) is the vorticity of the liquid phase velocity field v_l. Tomiyama (1998) proposed a model that describes the lift coefficient as a function of the bubble Reynolds number and the modified Eötvös number (E_o').

$$E_o' = \frac{g(\rho_l - \rho_g) d_h^2}{\sigma}; d_h = d_b \left(1 + 0.163 E_o^{0.757} \right)^{\frac{1}{3}} \tag{27}$$

where d_h is the maximum horizontal dimension of the bubble. The general expression for the lift coefficient is defined as

$$C_L = \begin{cases} \min(0.288\tanh(0.121\mathsf{Re}_b), f(E_o')) & \text{if } E_o' \leq 4 \\ f(E_o') & \text{if } 4 < E_o' \leq 10 \\ -0.27 & \text{if } E_o' > 10 \end{cases} \tag{28}$$

$$f(E_o') = 0.00105(E_o')^3 - 0.0159(E_o')^2 - 0.0204E_o' + 0.474 \tag{29}$$

For Eötvös numbers $E_o \leq 1$, the bubble tends to maintain a spherical shape and migrate toward the wall. For $E_o > 1$, the bubble begins to deform, acquiring an oblate or elongated shape, and migrates toward the center of the geometry. The transition between these behaviors does not occur at a fixed Eötvös value, as it also depends on other system characteristics, such as fluid properties and flow conditions. However, in general, bubbles with E_o above approximately 10 begin to exhibit significant deformation (TOMIYAMA, 1998).

3.1.3.3 Wall Lubrication Force

The third force coupled to the model is the wall lubrication force. As previously mentioned, interactions such as the lift force can cause bubbles to migrate toward the wall of the geometry, and a repulsive force arises as a bubble approaches the wall. When a rising bubble nears the wall, it experiences an asymmetric velocity field, caused by the presence of liquid between the bubble and the wall. This velocity asymmetry results in a hydrodynamic force that pushes the bubble away from the wall. The equation that describes this force is shown below:

$$\vec{F}_{WL} = -C_{WL}\rho_l \left|(\vec{v}_g - \vec{v}_l)_w\right|^2 \vec{n}_w \tag{30}$$

where C_{WL} is the wall lubrication force coefficient, and $\vec{n}_w$ is the unit vector perpendicular to the wall. According to the model proposed by Antal *et al.* (1991), the coefficient can be described as:

$$C_{WL} = \max\left(0; \frac{C_{WL1}}{d_b} + \frac{C_{WL2}}{\delta_w}\right) \tag{31}$$

where the term δ_w represents the distance between the wall and the bubble's position. The parameters C_{WL1} and C_{WL2} are coefficients defined in the model by Antal *et al.* (1991), used to describe the intensity of the force as the bubble approaches the wall. These parameters are set to -0.01 and 0.05, respectively.

3.1.3.4 Virtual Mass Force

The virtual mass force accounts for the additional force a bubble must exert to displace the surrounding fluid as it accelerates through the continuous phase. Drew e Lahey (1987), define virtual mass as:

$$F_{VM} = C_{VM}\rho_l \left(\frac{D_g \vec{v}_g}{Dt} - \frac{D_l \vec{v}_l}{Dt} \right) \tag{32}$$

where C_{VM} refers to the virtual mass coefficient. Commonly, studies such as Auton *et al.* (1988) adopt a value of $C_{VM} = 0.5$ for this coefficient.

3.1.3.5 Turbulent Dispersion Force

The last force included in the model is the turbulent dispersion force (F_{TD}), which represents the influence of the continuous phase on the dispersed phase. The model proposed by Bertodano (1991) was used in the current work to describe this force:

$$F_{TD} = -C_{TD}\rho_l k_l \nabla \alpha_l \tag{33}$$

where k_l is the turbulent kinetic energy and C_{TD} is the turbulent dispersion coefficient. Bertodano (1991) suggested that the dispersion coefficient be set to 0.1. During single-phase flow, the low Reynolds number indicates a laminar regime. However, the introduction of a dispersed phase alters the flow dynamics. The interaction between the phases causes velocity fluctuations, promoting instabilities that can induce turbulence in the continuous phase.

3.1.4 Turbulence Models

The effective viscosity of the liquid phase $\mu_{eff,l}$ represents the total resistance to flow and is calculated as the sum of the fluid's molecular viscosity μ, the turbulent viscosity generated in the liquid phase $\mu_{t,l}$, and a term related to the bubble-induced turbulent viscosity $\mu_{t,ib}$. While the molecular viscosity is an intrinsic physical property of the fluid, the turbulent viscosity arises from the Reynolds-averaging process and the application of the Boussinesq hypothesis, being associated with the additional stresses generated by velocity field fluctuations (POPE, 2000). The determination of the turbulent viscosity in the liquid phase depends directly on the turbulence models adopted, as discussed below.

The $k - \varepsilon$ model is used to represent flows with high Reynolds numbers, based on two transport equations: one for the turbulent kinetic energy k and another for the dissipation rate ε. Although it is commonly applied in fully developed flow regions, this model has limitations near

walls, where large velocity gradients occur. Alternatively, the $k-\omega$ model uses the specific turbulence generation rate ω and performs better in boundary layer regions and flows with complex geometry. The SST (Shear Stress Transport) model combines the advantages of both previous models, operating as a $k-\omega$ model near the walls and as a $k-\varepsilon$ model in the remaining flow regions. This combination is particularly effective, as it improves the prediction of turbulence induced at the phase interfaces (ISHII; MISHIMA, 1984).

To capture the transition from laminar to turbulent flow induced by bubble–liquid interactions, the Gamma–Theta transition model was implemented. This model is based on two parameters: Gamma (γ), representing the intermittency or turbulence fraction in the flow, and Theta (θ), which is associated with the boundary layer transition length scale.

In addition to the turbulence generated by flow instabilities, there is an additional phenomenon known as bubble-induced turbulence. This effect arises from the disturbances that bubbles create in the continuous fluid as they move through it, forming vortices in their wake and increasing velocity fluctuations. To represent this phenomenon, the model proposed by Sato e Sekoguchi (1975) is adopted, which defines an additional turbulent viscosity associated with the bubbles. Thus, the effective turbulent viscosity of the liquid phase is expressed as the sum of the molecular viscosity, the turbulence of the liquid phase, and the turbulence induced by the bubbles.

$$\mu_{\text{eff},l} = \mu_t + \mu_{t,l} + \mu_{t,ib} \tag{34}$$

where $\mu_{t,ib} = C_{\text{Sato}}\,\rho_l\,d_b\,\alpha_g\,|\vec{v}_g - \vec{v}_l|$. This additional term depends on the average bubble diameter d_b, the local void fraction α_g, the relative velocity between phases, and an empirical coefficient C_{Sato}, typically valued at 0.6. The inclusion of this model is essential for simulations that aim to more accurately represent the effects of the gas phase on the flow, especially in electrolyzers operating under bubbly flow regimes.

The effective viscosity of the gas phase ($\mu_{\text{eff},g}$) is calculated based on the effective viscosity of the liquid phase, as proposed by Zhan *et al.* (2017a):

$$\mu_{\text{eff},g} = \frac{\mu_{\text{eff},l}\,\rho_g}{\rho_l} \tag{35}$$

3.1.5 Breakup and Coalescence Model

To achieve a more accurate distribution of bubble diameters in the flow, the MUSIG (Multiple Size Group) as proposed by Lo (1996) is adopted. This model extends the two-fluid formulation with the theory of population balance, where the dispersed phase is segmented into groups based on bubble size, that represent certain probabilities of occurrence. The model is described by the size fraction, which refers to the proportion of the gas volume occupied by a specific bubble size. The size fraction is defined as $f_m = \frac{M_m N_m}{\alpha_g \rho_g} = \frac{\alpha_m}{\alpha_g}$, where M_m and α_m

represent the mass and volume fraction of group , respectively. The N_m refers to the probability of occurrence of group m at a given point in the flow. Equation 36 describes the model:

$$\nabla \cdot \left(\alpha_g \rho_g \vec{V}_g f_m \right) = B_m^c + D_m^c + B_m^q + D_m^q \tag{36}$$

The first term represents the transport of the size fraction across the volume. On the right-hand side, the terms correspond to the birth and death rates of bubbles in group m due to coalescence and breakup phenomena. Specifically, B_m^c and D_m^c, represent the birth and death rates by coalescence, respectively, while B_m^q and D_m^q, represent the birth and death rates by breakup.

The MUSIG model resolves a transport equation for the size fraction f_m of each group, which describes the advection and diffusion of the size fractions throughout the flow field. Additional source and sink terms account for the birth and death rates of bubbles due to coalescence and breakup phenomena, allowing the model to predict the evolution of the bubble size distribution over time.

To describe the bubble breakup rate, the model proposed by Liao *et al.* (2015) is used. This model is based on the breakup criterion developed MARTÍNEZ-BAZÁN *et al.* (1999). When immersed in a flow, the bubbles experience a destructive stress (τ_{destr}), generated by external mechanisms such as turbulence. The surface tension of the bubble acts to restore its original shape, therefore, breakup only occurs if τ_{destr} exceeds the critical stress (τ_{crit}).

According to MARTÍNEZ-BAZÁN *et al.* (1999), the breakup frequency of a parent bubble with diameter d_m into daughter bubbles of diameter d_n, denoted by $\Omega_Q(d_m,d_n)$, depends on the relationship between τ_{destr} and τ_{crit}. The equation is given as follows:

$$\Omega_Q(d_m,d_n) = \begin{cases} \frac{1}{d_m}\sqrt{\frac{\tau_{\text{destr}}-\tau_{\text{crit}}}{\rho_L}} & \text{if } \tau_{\text{destr}} > \tau_{\text{crit}} \\ 0 & \text{if } \tau_{\text{destr}} \leq \tau_{\text{crit}} \end{cases} \tag{37}$$

The model assumes that a bubble of size d_m breaks into two other bubbles: one of size d_n for which the breakage rate is calculated using Equation 37, and a complementary bubble of size d_p, calculated as:

$$d_p = \left(d_m^3 - d_n^3 \right)^{1/3} \tag{38}$$

The critical stress (τ_{crit}) is calculated by combining two criteria. The first criterion (τ_{crit1}) is determined by the increase in the energy required to form the surfaces of the daughter bubbles d_n and d_p compared to the energy needed to form the parent bubble d_m. The second criterion (τ_{crit2}) is determined by the capillary force of the smallest bubble formed after the breakup.

$$\tau_{\text{crit}} = \max(\tau_{\text{crit1}}, \tau_{\text{crit2}}) \tag{39}$$

$$\tau_{\text{crit1}} = \frac{6\sigma}{d_m}\left(\left(\frac{d_n}{d_m}\right)^2 + \left(\frac{d_p}{d_m}\right)^2 - 1\right) \tag{40}$$

$$\tau_{\text{crit2}} = \frac{\sigma}{\min(d_n, d_p)} \tag{41}$$

where σ is the surface tension between the phases. The destructive stress (τ_{Destr}) is defined based on the bubble breakup mechanisms. According to Liao *et al.* (2015), the mechanisms include turbulent fluctuation, laminar shear, turbulent shear, and interfacial slip. In the case of water electrolysis, the turbulent fluctuation mechanism is considered appropriate, since the interaction between bubbles and the electrolyte generates velocity variations that promote the formation of turbulent regions. The equation that defines the destructive stress under the turbulent fluctuation mechanism is shown below:

$$\tau_{\text{destr}} = \rho_l \left(\varepsilon_l \cdot d_m\right)^{2/3} \tag{42}$$

where ε is the turbulence dissipation rate of the liquid phase, estimated by $\varepsilon = C_{mu}.k_l.\omega_l$. In this equation, k_l is the turbulent kinetic energy of the liquid phase, ω_l is the specific dissipation rate per unit of turbulent kinetic energy, and C_{mu} is a constant that describes turbulence behavior, which is typically 0.09, as defined by Liao *et al.* (2015).

Coalescence in gas–liquid flows generally results from collisions between bubbles. The model adopted to describe this phenomenon in the current work is based on the formulation proposed by Prince e Blanch (1990).

The total coalescence frequency between two bubbles from size groups i and j is modeled as the sum of various physical mechanisms that may lead to collisions, including turbulence effects, eddy capture, velocity gradients in the mean flow, body forces, and wake entrainment. The model assumes that the contributions of these mechanisms are cumulative and modulated by a damping function that increases the collision frequency as the local gas volume fraction approaches the maximum packing limit $\alpha_{g,\text{max}}$, typically set to 0.8, as proposed by Wang, Wang e Jin (2005). Thus, the total coalescence frequency is expressed as:

$$\Gamma_{mi,mj} = \left(\frac{\alpha_{g,\text{max}}}{\alpha_{g,\text{max}} - \alpha_g}\right) \cdot \left(\Gamma_{\text{turb}} + \Gamma_{\text{buoy}} + \Gamma_{\text{eddy}} + \Gamma_{\text{shear}} + \Gamma_{\text{wake}}\right) \tag{43}$$

However, a simple collision between bubbles does not guarantee coalescence, and the concept of coalescence efficiency λ is introduced, which represents the probability that two colliding bubbles will merge. Thus, the effective coalescence frequency is defined as:

$$\Gamma = h \cdot \lambda \tag{44}$$

where h represents the collision frequency and λ the coalescence efficiency associated with the interaction between bubble pairs. The collision frequency, is modeled based on analogies from kinetic gas theory, where the collision rate depends on the product of the relative approach velocity u_{rel} between two bubbles of sizes m and n, and the effective collision cross-sectional area A:

$$h = A \cdot u_{\text{rel}} \tag{45}$$

$$A = \frac{\pi}{4} \left(d_m + d_n\right)^2 \tag{46}$$

Following the approach of Zhan *et al.* (2017a), only the wake entrainment mechanism of coalescence is here considered. This phenomenon occurs when larger bubbles generate recirculation regions in their wake, allowing smaller bubbles entering this region to be accelerated and collide with the leading bubble. The relative velocity generated by this effect is estimated as follows:

$$u_{\text{rel,wake}} = C_{\text{wake}} \cdot U_{T,m} \cdot C_{D,m}^{1/3} \tag{47}$$

where C_{wake} is an empirical coefficient, $U_{T,m}$ is the terminal velocity of bubble m, and $C_{D,m}$ is the drag coefficient of the bubble. Assuming that wake-induced collisions always result in coalescence (λ = 1), the resulting coalescence frequency can be expressed as:

$$\Gamma_{\text{wake}} = \frac{C_{\text{wake}} \cdot 0.5\pi}{4} \left[d_m^2 U_{T,m} C_{D,m}^{1/3} \theta_m + d_n^2 U_{T,n} C_{D,n}^{1/3} \theta_n \right] \tag{48}$$

The term θ represents a blending function that modulates the contribution of wake-induced coalescence based on the bubble diameter relative to a critical diameter d_{crit}. The function is given by:

$$\theta_m = \begin{cases} \dfrac{(d_m - 0.5\,d_{\text{crit}})^6}{(d_m - 0.5\,d_{\text{crit}})^6 + (0.5\,d_{\text{crit}})^6} & \text{if } d_m > 0.5\,d_{\text{crit}} \\ 0 & \text{otherwise} \end{cases} \tag{49}$$

With the critical diameter defined as:

$$d_{\text{crit}} = 4.0\sqrt{\frac{\sigma}{g\,(\rho_l - \rho_g)}} \tag{50}$$

The coalescence efficiency λ can take different forms depending on whether inertial or viscous effects dominate the collision. When inertial effects prevail (typically for larger bubbles), the maximum Weber number is used:

$$\lambda_{\text{inertial}} = \exp\left(-C_{\text{eff}} \cdot \text{We}_{mn,\text{max}}^{0.5}\right) \tag{51}$$

$$\text{We}_{mn,\text{max}}^{0.5} = \frac{\rho_l d_{\text{eq}}}{\sigma}\left(U_{\text{real,wake}}\right)^2 \tag{52}$$

$$d_{\text{eq}} = \frac{2 d_m d_n}{d_m + d_n} \tag{53}$$

For collisions dominated by viscous effects (typically involving small bubbles), the efficiency is expressed as:

$$\lambda_{\text{viscous}} = \exp\left[-\left(\frac{3\mu_l d_{\text{eq}}\gamma_{\text{eddy}}}{4\sigma}\right)\ln\left(\frac{\pi\sigma d_{\text{eq}}^2}{32 A_H}\right)^{1/3}\right] \tag{54}$$

where A_H is the Hamaker constant (typically 3.7×10^{-20} J for air–water systems), and γ_{eddy} is the local turbulent shear rate.

3.2 Boundary Conditions

The boundary conditions were defined to represent the flow behavior inside the electrolytic cell. Initially, single-phase flow simulations were performed to analyze the behavior of the electrolyte within the geometry, without the presence of hydrogen bubbles. This approach allows for the assessment of the impact of the dispersed phase on the flow. Subsequently, two-phase flow simulations were conducted, including both monodisperse and polydisperse cases.

The simulated domain was defined as a three-dimensional rectangular geometry with a square-section channel through which the electrolyte enters. The simulations were carried out under steady-state conditions, assuming incompressible flow. A volumetric flow rate was specified at the inlet, with the values varying for each simulated case, as detailed in the next sections. The flow was simulated under isothermal conditions at 25℃, with the outlet pressure set to 0 Pa. A no-slip condition was applied to the domain walls, while the lateral faces were defined with symmetry conditions, representing the continuity of flow between adjacent channels. The geometric dimensions are listed in Figure 24.

Figure 24 – Simulation Parameters

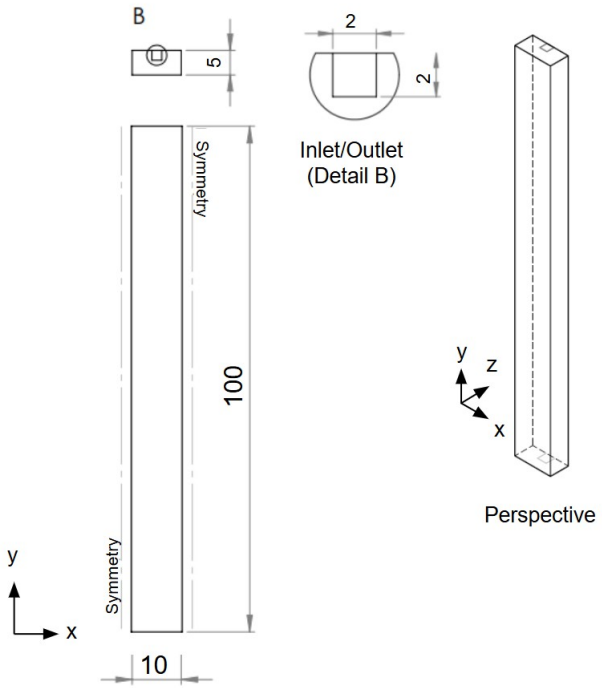

Source: The author.

3.2.1 Single-Phase Simulation

The single-phase simulations were performed with the aim of understanding the behavior of the electrolyte flow within the proposed geometry, as well as enabling the assessment of the bubbles' influence on the continuous phase by comparing with the two-phase flow simulation results. The domain was filled only with electrolyte - a solution of KOH (potassium hydroxide) in water - with a density of $\rho_{\text{KOH}} = 1050\,\text{kg/m}^3$, according to the study by Mat *et al.* (2004).The electrolyte was injected through the square channel illustrated in Figure 23, at a constant flow rate Q, different flow rates were tested for each case: 30, 50, and 70 ml/min.

3.2.2 Two-Phase Flow Simulation

In the two-phase simulation, in addition to the electrolyte, hydrogen gas was also considered, with a density of $\rho_{H2} = 0.08\,\text{kg/m}^3$, according to the study by Mat *et al.* (2004). The hydrogen gas was injected uniformly along the rear face of the cell, as illustrated in Figure 23, with a constant flow rate of 15 ml/min for all cases. The surface tension between the phases was set to $\sigma = 0.072N/m$ according to Weast (1976).

A sensitivity analysis was carried out to evaluate the effect of the different interfacial forces: drag force (F_D), lift force (F_L), wall lubrication force (F_{WL}), virtual mass force (F_{VM}), and turbulent dispersion force (F_{TD}).

The monodisperse two-phase cases were defined using bubbles with fixed diameters of 50μm, 100μm, and 200μm, respectively. For the polydisperse case, the Population Balance Model (PBM) was implemented through the Multiple Size Group Model (MUSIG) approach, using five bubble size groups, as summarized in Tables 3. These groups cover a diameter range from 50μm to 100μm and 100μm to 200μm, allowing for a discrete representation of the bubble size distribution throughout the flow.

Table 3 – Bubble size groups defined in the MUSIG model for both diameter ranges tested

Range [µm]	Group	Mean Diameter d_m [µm]	Inlet Volume Fraction Share [%]
50–100	1	50	20
	2	62.5	20
	3	75	20
	4	87.5	20
	5	100	20
100–200	1	100	20
	2	125	20
	3	150	20
	4	175	20
	5	200	20

Source: Author.

The bubble sizes were based on the experimental scales reported by Boissonneau e Byrne (2000), in which the applied current densities ranged from 500 to 2000 A/m^2. For all cases, monodisperse and polydisperse, the electrolyte flow rates were varied at 30, 50, and 70 ml/min. Additionally, an analysis of the influence of varying the inlet gas flow rate was conducted by simulating two additional values: 10 and 20 mL/min, corresponding to estimated current densities of 130mA/cm² and 260mA/cm², respectively. These gas flow simulations were performed with a constant electrolyte flow rate of 50 mL/min.

3.3 Numerical Procedure

The governing equations presented earlier were solved using the computational fluid dynamics software *ANSYS®CFX®*, which applies the finite volume method based on elements. This approach involves discretizing the computational domain into a numerical mesh composed of finite control volumes. The governing equations are integrated, discretized, and linearized, resulting in an algebraic system of equations that is solved computationally through an iterative process (ANSYS, Inc., 2019).

The root-mean-square of normalized residuals below 10^{-5} was set as a convergence criterion for the single-phase cases and below 10^{-4} for the two-phase cases. The computational time was 21 minutes and 5 seconds for the single-phase simulations, 21 hours, 22 minutes, and 38 seconds for the two-phase monodisperse case, and 1 day, 1 hour, 50 minutes, and 48 seconds for the two-phase polydisperse case using an *Intel Core i7-13700KF CPU @ 3.40 GHz*.

As shown in Figure 25, the analyzes were performed across seven different regions throughout the geometry (lines 1 to 7). Regions 1, 2, and 3 are horizontal lines ranging from x* = 0 to x* = 1, located at z* = 0.2 and positioned at y* = 0.05, y* = 0.5, and y* = 0.95, respectively. Regions 4, 5, and 6 are horizontal lines extending from z* = 0 to 1, located at x* = 0.5 and positioned at y* = 0.05, y* = 0.5, and y* = 0.95, respectively. Region 7 is a vertical line ranging from y* = 0 to 1, positioned exactly at the center of the inlet and square outlet channels, at x* = 0.5 and z* = 0.2. The data were extracted along these lines and plotted for comparative analysis.

Figure 25 – Demonstration of the analysis regions

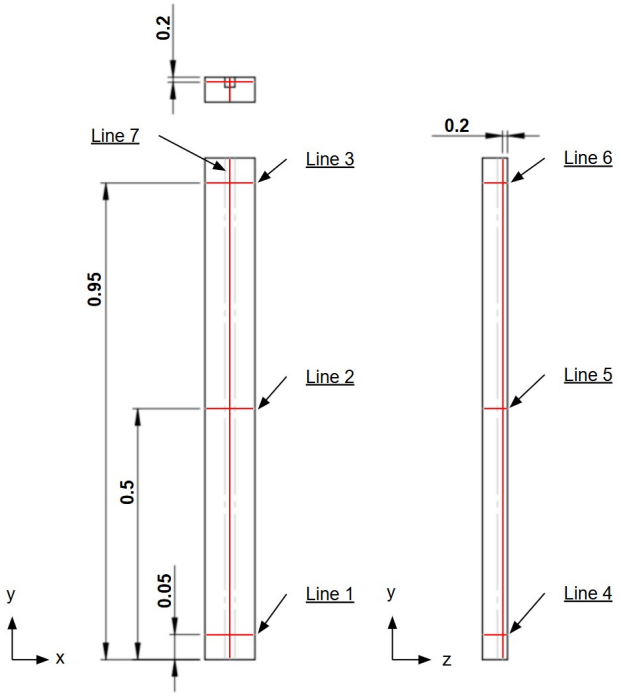

Source: The author.

To evaluate the influence of mesh refinement on the results, mesh sensitivity tests were conducted for both single-phase and two-phase flow cases. Five meshes composed of structured hexahedral elements, varying in the number of nodes and elements, were created. Four meshes were used for the single-phase simulations, and an additional mesh was created specifically for the two-phase cases. The five mesh configurations are illustrated in Figure 26, and the corresponding element and node counts are presented in Table 4.

Figure 26 – Mesh Refinement Study

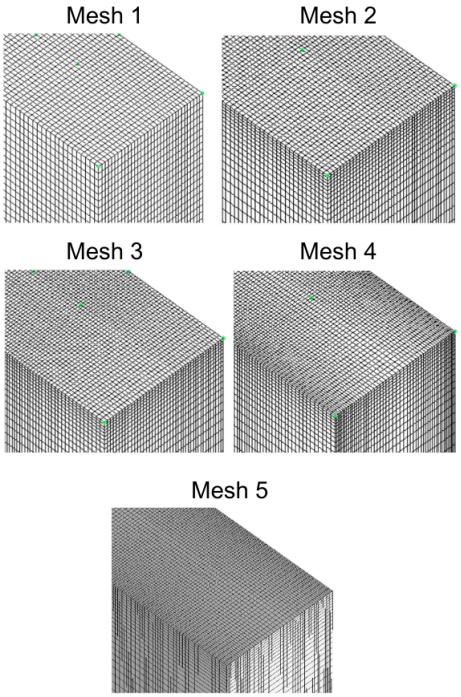

Source: The author.

Table 4 – Mesh Characteristics

Mesh	Number of Elements	Number of Nodes
M_1	172.619	163.200
M_2	290.214	277.200
M_3	358.339	343.200
M_4	438.109	421.200
M_5	568.339	547.560

Source: Author.

3.3.1 Mesh Sensitivity Test for the Single-Phase Flow Case

The mesh sensitivity test for the single-phase flow case was conducted considering a steady-state, Newtonian, viscous, incompressible, isothermal, and laminar flow. The inlet flow rate of the electrolyte was set to 50 ml/min. The four mesh cases were simulated and their results compared. The y-component velocity of the electrolyte was used for comparison.

The analysis region was Region 2 (x = 0 to 10 mm; y = 50 mm; z = 1 mm). Figure 27 presents the overlapping of the velocity profiles for the different meshes. A difference is observed between meshes 1 and 2, while the electrolyte velocity profiles of meshes 3 and 4 are practically the same. Therefore, Mesh 3 was selected for single-phase simulations, as it provides the optimal balance between result accuracy and computational cost.

Figure 27 – Comparison of Velocity Profiles for Different Meshes in Single-Phase case

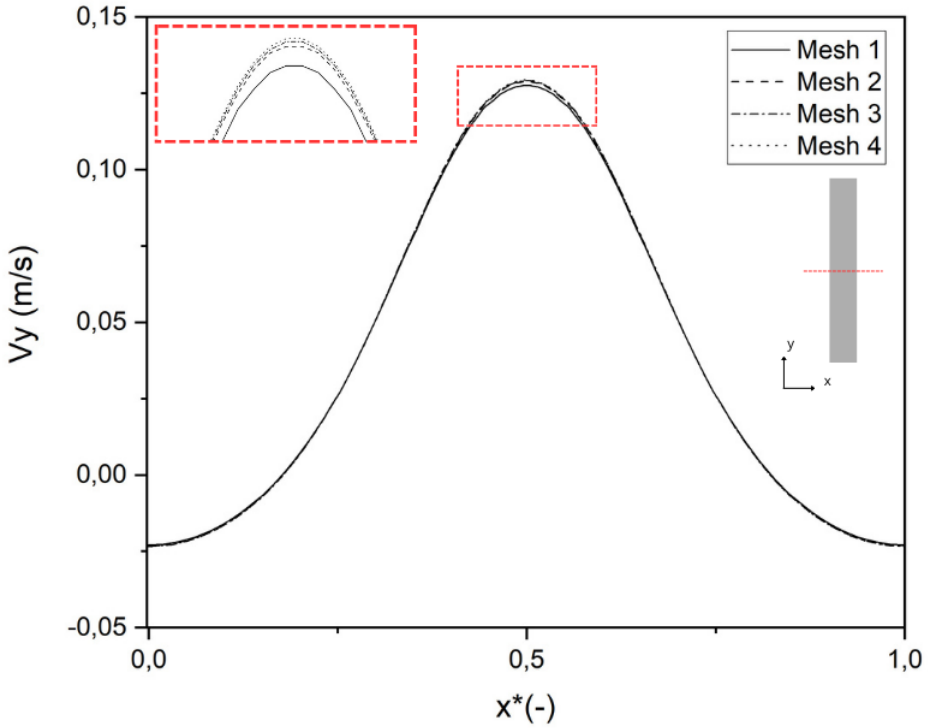

Source: Author.

3.3.2 Mesh Sensitivity Test for the Two-Phase Case

The mesh sensitivity test for the two-phase flow case was conducted under steady-state, Newtonian, viscous, incompressible, and isothermal conditions. The inlet flow rate of the electrolyte was set to 50 mL/min, while the inlet flow rate of hydrogen gas was 15 mL/min, with a bubble diameter of 50 μm.

In order to reduce computational cost, the five different meshes were simulated considering only the monodisperse case. For the comparison, the profiles of hydrogen gas volume fraction were evaluated. The analysis was conducted in Region 6 (x = 5 mm; y = 75 mm; z ranging from 0 to 5 mm). Figure 28a shows the superposition of results obtained with the first four meshes. As shown, the volume fraction profiles exhibit significant differences between Meshes 3 and 4, indicating that the refinement applied in Mesh 4 had a relevant impact on resolving the two-phase flow. For this reason, an additional mesh was created and compared with Mesh 4. The comparison shown in Figure 28b indicates that both produced similar results. Therefore,

Mesh 4 was selected for the single-phase simulations, as it offers the best balance between result accuracy and computational cost.

Figure 28 – Comparison of Hydrogen Gas Volume Fraction Profiles in Two-Phase case

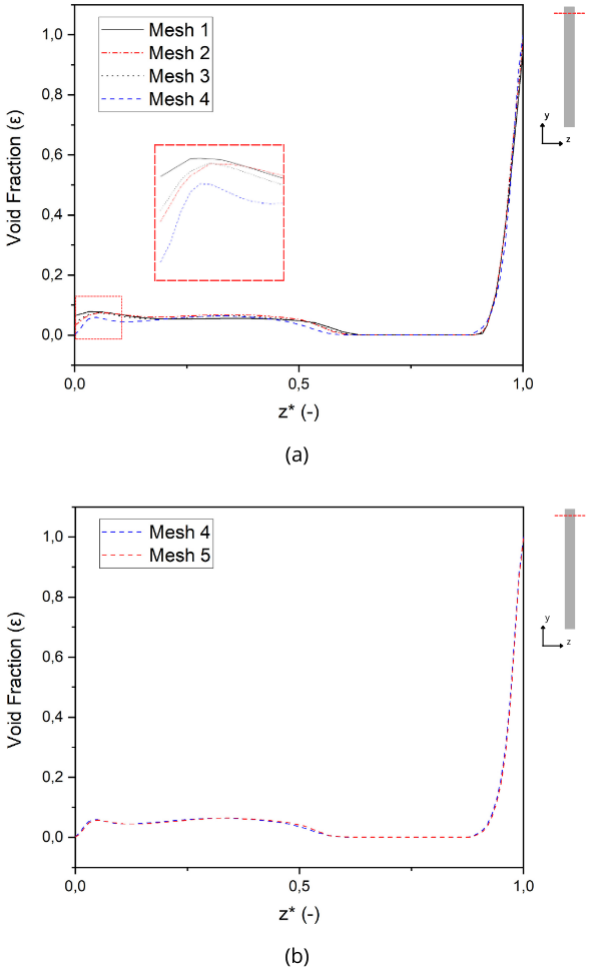

Source: Author.

To confirm the numerical stability of the mesh 4, a local residual analysis was performed for the hydrogen gas volume fraction variable. Nine monitoring points were selected along the geometry, and the residual associated with this variable was tracked over 1000 iterations. Figure 29a shows the distribution of the monitoring points throughout the geometry.

Based on this analysis, it was observed that Mesh 4 demonstrated adequate numerical stability, with the residuals consistently remaining below 10^{-4}. Figure 29b illustrates the behavior of the monitored residuals throughout the simulation process.

Figure 29 – Local Residuals of Hydrogen Gas Volume Fraction for Mesh 4

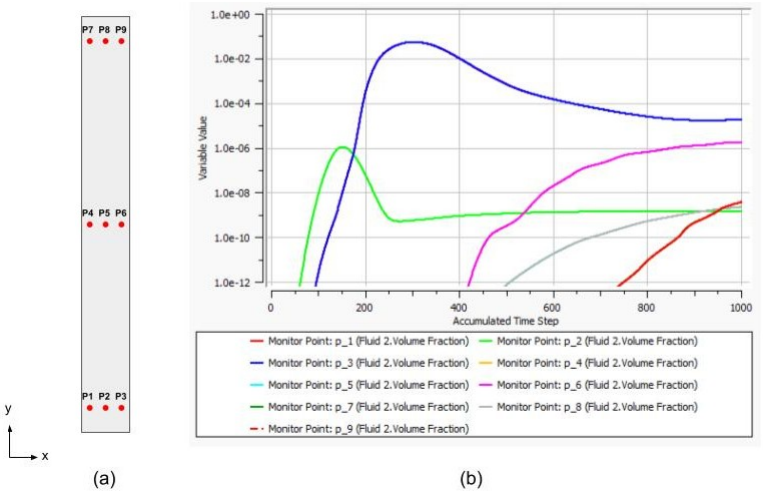

Source: Author.

3.3.3 Interfacial Force Sensitivity Test

In order to evaluate the individual influence of interfacial forces on the behavior of the two-phase flow, a sensitivity test was conducted considering three distinct simulation configurations: monodisperse with 50μm bubbles, monodisperse with 100μm bubbles, and polydisperse with a distribution between 50 and 100μm. The inlet flow rate of the electrolyte was set at 50 mL/min, while the inlet flow rate of hydrogen gas was 15 mL/min. For each configuration, five simulations were carried out by including the interfacial in the numerical model:

- $\rightarrow$ S1: Only drag force;
- $\rightarrow$ S2: Drag + lift force;
- $\rightarrow$ S3: Drag + wall lubrication force;
- $\rightarrow$ S4: Drag + turbulent dispersion force;
- $\rightarrow$ S5: Drag + virtual mass force.

The simulations were analyzed through visual comparison of electrolyte velocity contours in the YX and YZ planes, as well as void fraction contours in the YZ plane. Figure 31 presents the electrolyte velocity contour for simulation S1 (only drag force). It was observed that the drag force is the dominant interfacial force, significantly affecting both the direction and intensity of the flow.

In this configuration, the drag force is primarily responsible for the phase interactions. In the YX plane, a region of electrolyte deceleration is formed in the lower half of the geometry along the centerline. This slowdown is attributed to the resistance imposed by the rising gas bubbles due to the drag effect. As the bubbles rise due to buoyancy, the gas displaces the flow

streamline laterally, resulting in a characteristic velocity profile with acceleration in the channel extremities (symmetry regions). In the upper half of the flow domain, the electrolyte accelerates again, now due to the gas-lift effect, as the concentration of bubbles increases, the electrolyte is accelerated due to their ascent.

The comparison between the 50 and 100 μm monodisperse cases shows no significant variation in flow patterns, indicating that, at this stage, the drag force alone exhibits limited sensitivity to bubble size. In contrast, the polydisperse case reveals a distinct flow pattern due to the distribution of bubbles across different size groups. However, the overall flow behavior maintains the same central deceleration and subsequent upper-half acceleration, consistent with the monodisperse cases. For the void fraction contours, the monodisperse cases indicate a small difference in the length of the gas accumulation layer along the rear wall, showing a reduced thickness with 100 μm bubbles. A noticeable distinction is observed between monodisperse and polydisperse cases, which will be further explored in the following sections.

Figure 30 – Electrolyte velocity and Void Fraction contours for only-drag force cases (S1)

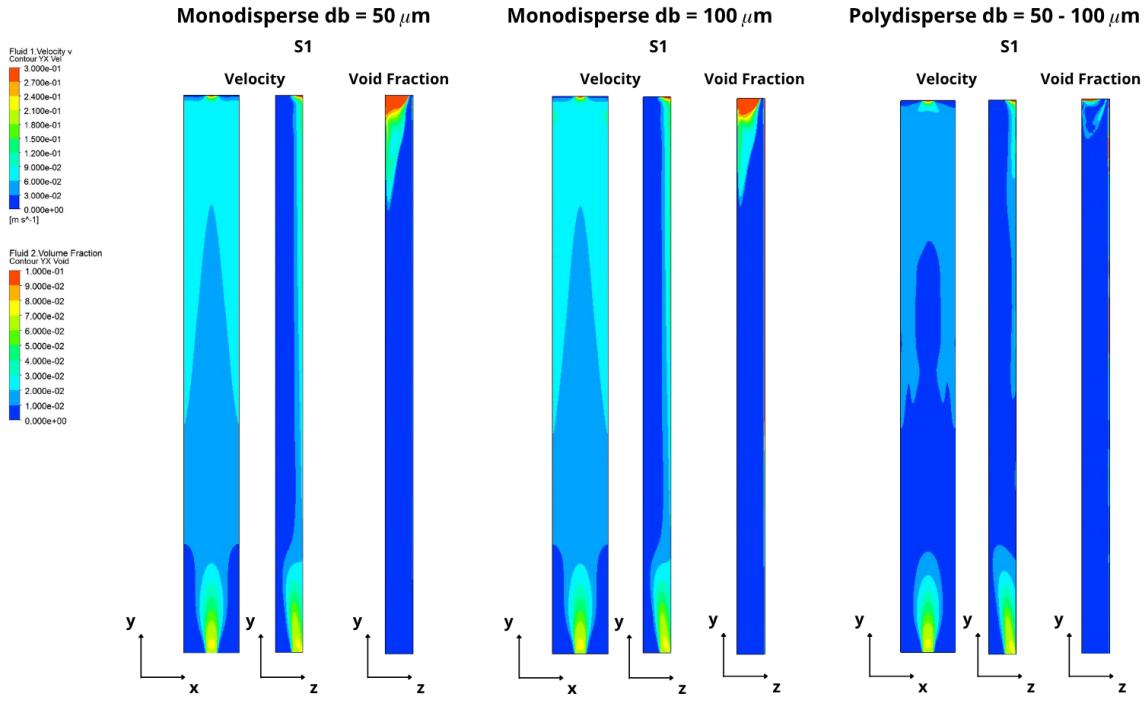

Source: Author.

Among all tested force combinations, only the coupling of drag force with turbulent dispersion resulted in great changes in the velocity contours, as shown in Figure 31. The presence of the turbulent dispersion force promotes a more homogeneous redistribution of the gas volume fraction, which results in distinct regions of electrolyte acceleration. This behavior highlights the importance of turbulent dispersion in the dynamics of two-phase flow in electrolyzers.

Figure 31 – Electrolyte velocity and Void Fraction contours for turbulent dispersion force cases (S4)

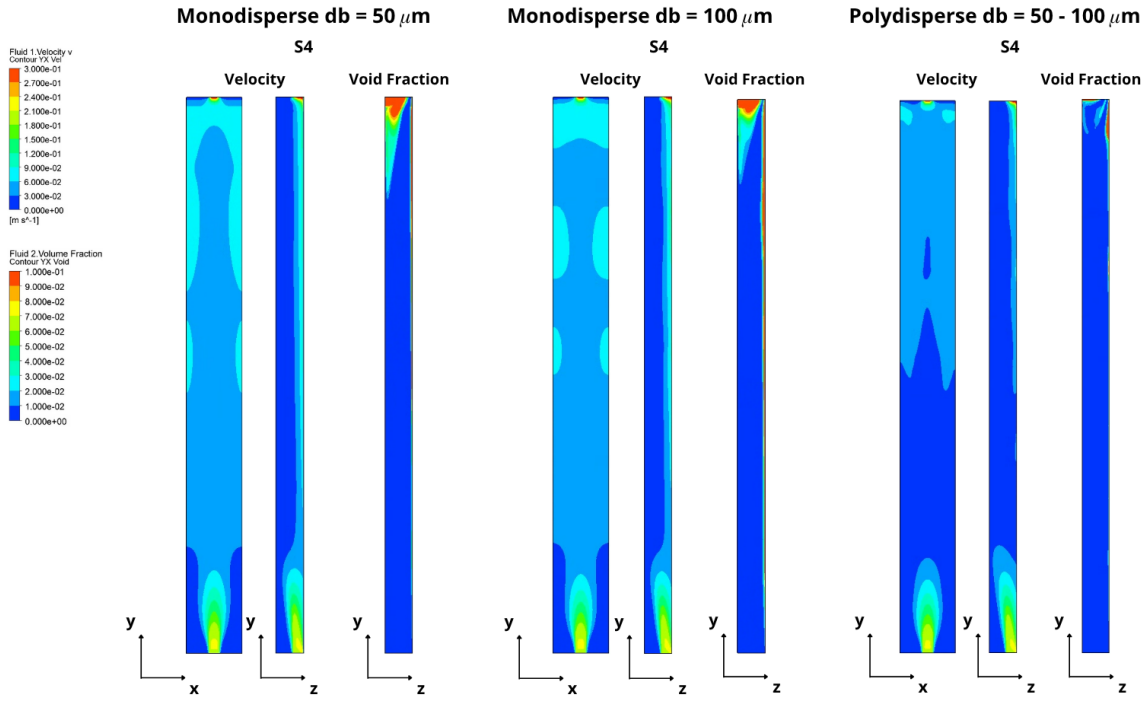

Source: Author.

Regarding the remaining forces, lift, wall lubrication, and virtual mass, no perceptible changes in velocity or void fraction contours were observed in the monodisperse cases, as shown in Figure 32. This limited sensitivity is mainly attributed to the low gas volume fraction and smooth velocity gradients characteristic of the simulated conditions, rather than to the use of a monodisperse model itself. Under such conditions, the drag and turbulent dispersion forces dominate the interfacial momentum exchange. Therefore, the final configuration adopted only the drag (F_D) and turbulent dispersion (F_{TD}) forces for the monodisperse cases.

Additionally, the same comparative analysis in the hydrogen gas volume fraction contours reinforces the pattern observed in the velocity field, as regions with higher dispersed phase concentration corresponded with areas of greater electrolyte upward velocity. Moreover, regions of greater bubble dispersion aligned with zones of higher electrolyte acceleration, indicating a direct correlation between gas phase redistribution and velocity profile development.

Figure 32 – Electrolyte velocity and Void Fraction contours for 50 and 100 μm monodisperse cases

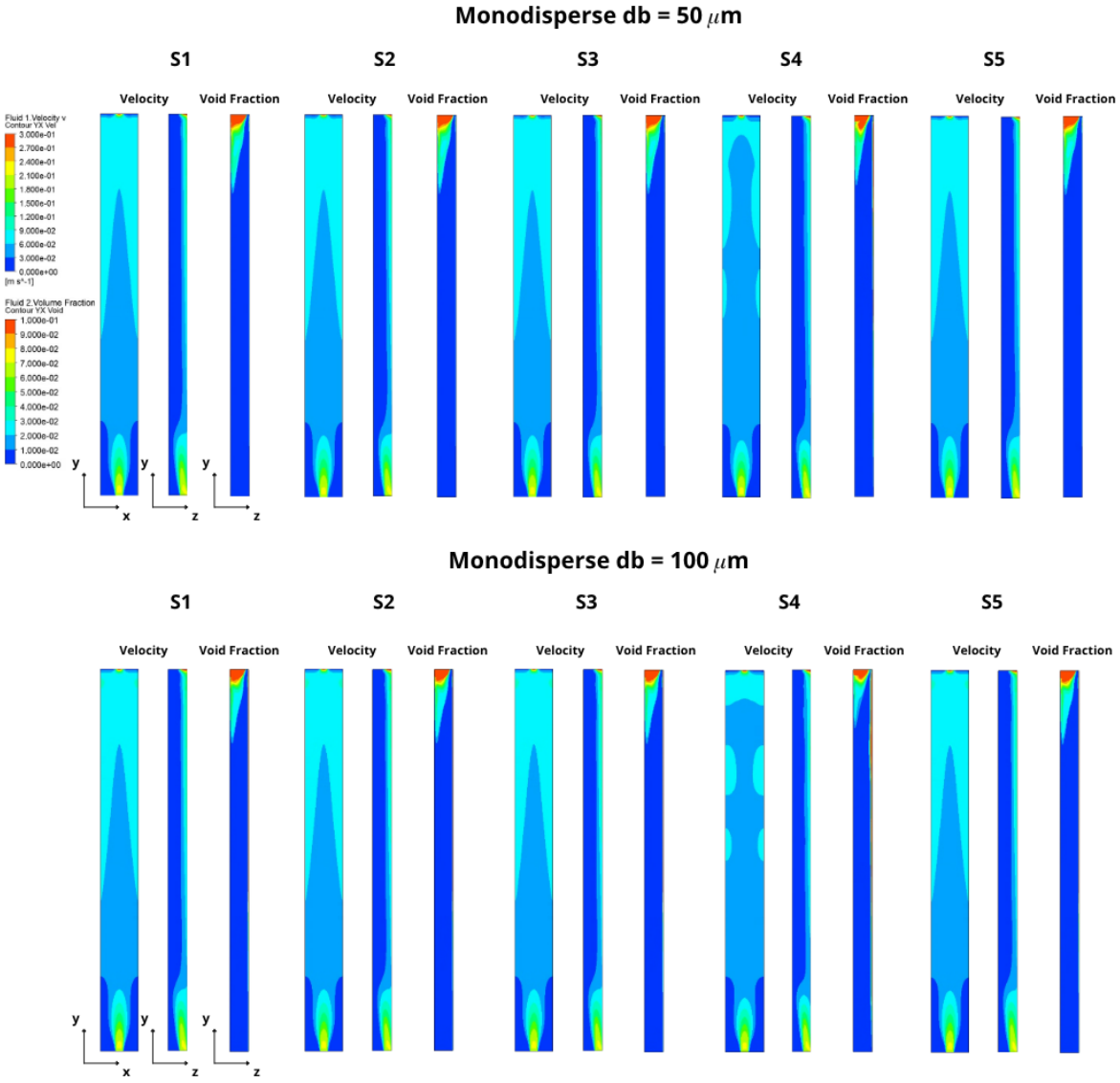

Source: Author.

In the polydisperse case, the turbulent dispersion force exhibited a stronger influence, and a higher sensitivity to the remaining interfacial forces was also observed, as shown in Figure 33. Compared to the monodisperse scenarios, the velocity distribution in the polydisperse flow exhibited more spatial variations, reflecting the complex interactions among the different bubble size groups.

The additional forces induced subtle changes, particularly near the upper rear region of the domain, where differences in the trapped gas fraction appeared across all force combinations. These results indicate that the inclusion of multiple bubble size classes increases the model's sensitivity to interfacial forces, affecting the local gas–liquid distribution and velocity field.

Based on this increased sensitivity, all forces were maintained in the polydisperse model except for virtual mass, which showed minimal influence and is also known to introduce numerical instability, as previously reported in the literature (KRISHNA; BATEN, 2001; OEY *et al.*, 2003; FRANK *et al.*, 2008b).

Figure 33 – Electrolyte velocity and Void Fraction contours for 50 - 100 μm polydisperse case

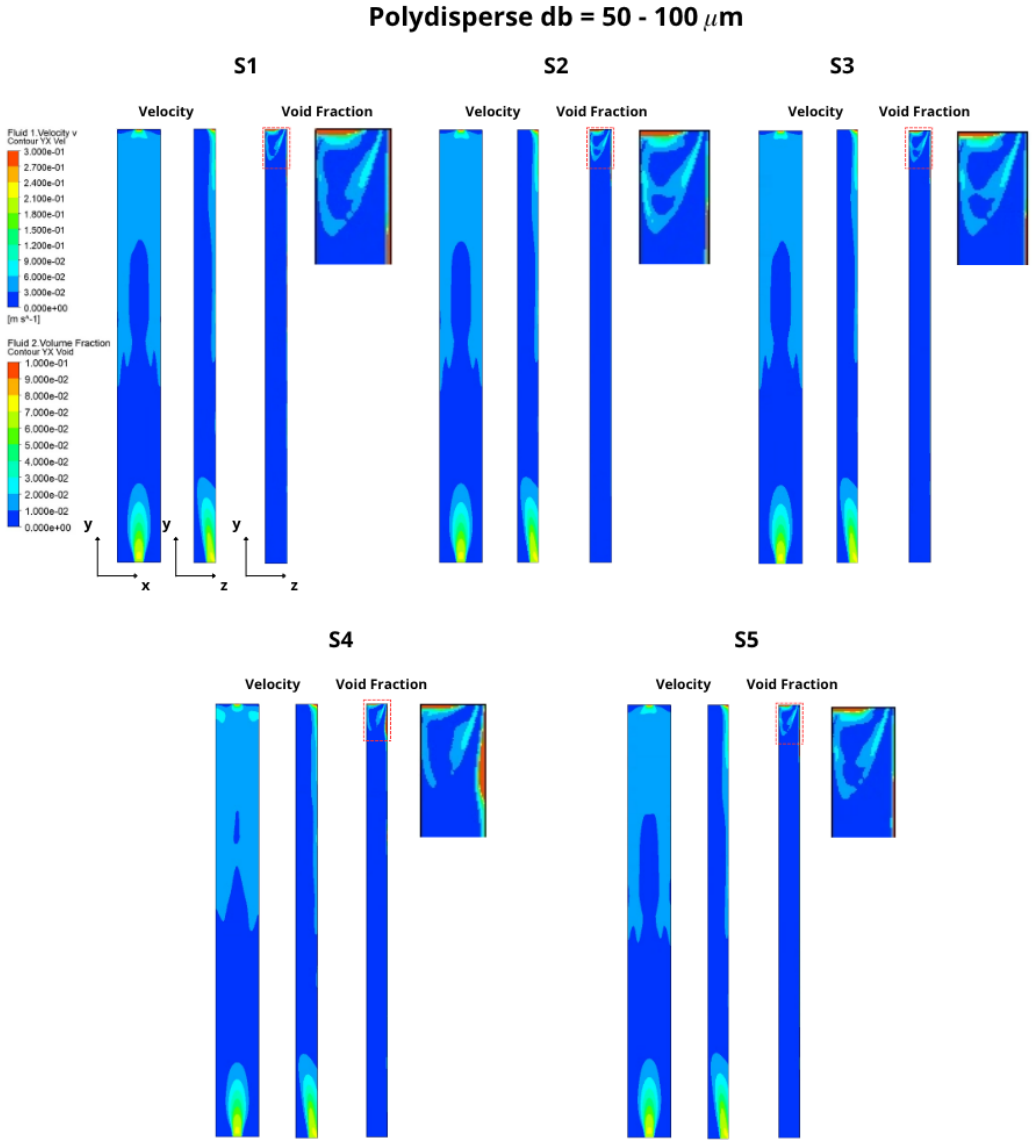

Source: Author.

4 RESULTS AND DISCUSSIONS

4.1 Model Calibration

The calibration of the coefficients of the two-phase mathematical model was carried out based on the experimental and numerical results of Rodríguez e Amores (2020), who simulated two-phase flow in an alkaline water electrolysis cell using a two-dimensional approach in the COMSOL® software. For comparison purposes, the present study adopted a similar geometry, consisting of electrodes with a height of 33 mm and a spacing of 1.5 mm relative to the membrane, modeled in three dimensions in ANSYS® CFX® with a minimum depth of 1 x 10^{-5} m. Figure 34 shows the hydrogen gas volume fraction contours obtained from Rodríguez e Amores (2020). The results indicated volume fractions ranging from 0 to 5% of gas.

Figure 34 – Demonstration of numerical and experimental analyses

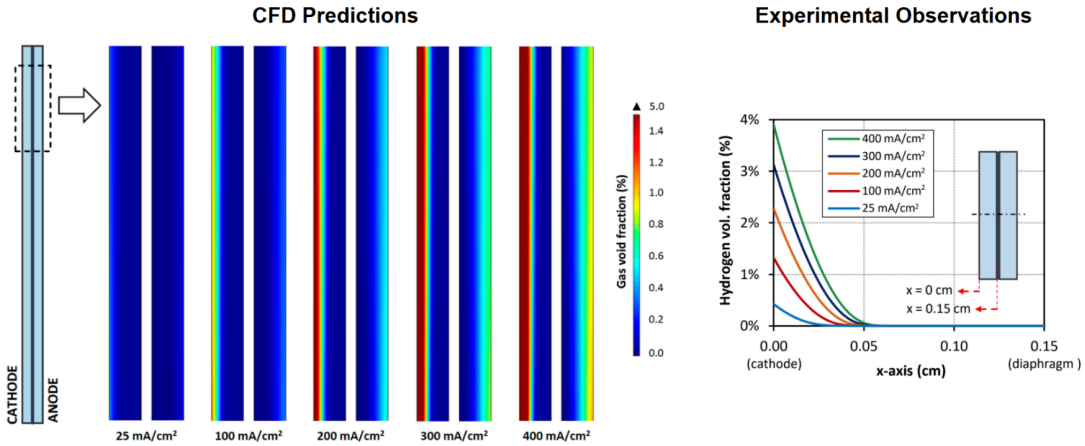

Source: Adapted from (RODRíGUEZ; AMORES, 2020).

To represent the system, the electrolyte volumetric flow rate was considered to be equally distributed between the two compartments of the cell, adopting 700 mL/min as the reference value, which corresponds to half of the total flow rate reported in the original study. To estimate the hydrogen flow rate generated electrochemically, a current density of 400 mA/cm² was used. The superficial gas generation velocity U_g, and consequently, the total volumetric flow rate was computed based on the equations derived from Faraday's Law, as proposed by Lima, Starke e Silva (2025):

$$U_g = \frac{M_g}{\rho_g \, nF} \, i \tag{55}$$

$$Q_{H_2,\text{total}} = U_g \cdot A_{\text{electrode}} \tag{56}$$

where M_g is the hydrogen molar mass (0.002 kg/mol); ρ_g is the hydrogen density at 25 °C and 1 atm (0.08076 kg/m³); $n = 2$ is the number of electrons transferred per mole of gas produced; $F = 96485$ C/mol is Faraday's constant; $i = 4000$ A/m^2 is the current density; $A_{\text{eletrodo}} = 3.3 \times 10^{-7}$ m^2 is the surface area modeled in the 3D domain.

The estimated hydrogen volumetric flow rate based on these parameters was approximately 1.016×10^{-2} ml/min. However, this extremely low value, resulting from the minimal depth adopted in the ANSYS CFX 3D representation, makes the evaluation of two-phase flow impossible.

An iterative calibration of the gas inlet flow rate was then required. This calibration was conducted by seeking values that would allow for adequate visualization of gas dispersion inside the cell and enable comparison with the profiles provided by Rodríguez e Amores (2020). The flow rate that provided the best visualization was on the order of 10 mL/min, which resulted in a visible gas volume fraction similar to the 300 mA/cm² profile shown in Figure 34.

Flow rates below this limit proved insufficient to capture the gas layer formed near the electrode surface, while higher values, in the monodisperse cases, resulted in the formation of a dense gas layer along the electrode wall.

Since the force sensitivity analysis demonstrated that the turbulent dispersion force is the most relevant in the model, different turbulent dispersion coefficients were tested to assess their influence on the flow. For the monodisperse case, bubbles with a diameter of 50 μm were used, and the turbulent dispersion coefficient was varied between 0.1 and 0.3.

However, Figure 35 shows that the low void fraction applied in this case was not sufficient to highlight the impact of turbulent dispersion. Although the gas volume fraction at x = 0 is similar to that reported by Rodríguez e Amores (2020), the overall profile does not exhibit the same distribution along the domain. This indicates that the model could not properly capture the influence of C_{TD} even with higher values, it was unable to reproduce the expected bubble dispersion.

Figure 35 – Comparison of the gas volume fraction contours obtained with two turbulent dispersion coefficients for a Monodisperse two-phase flow case

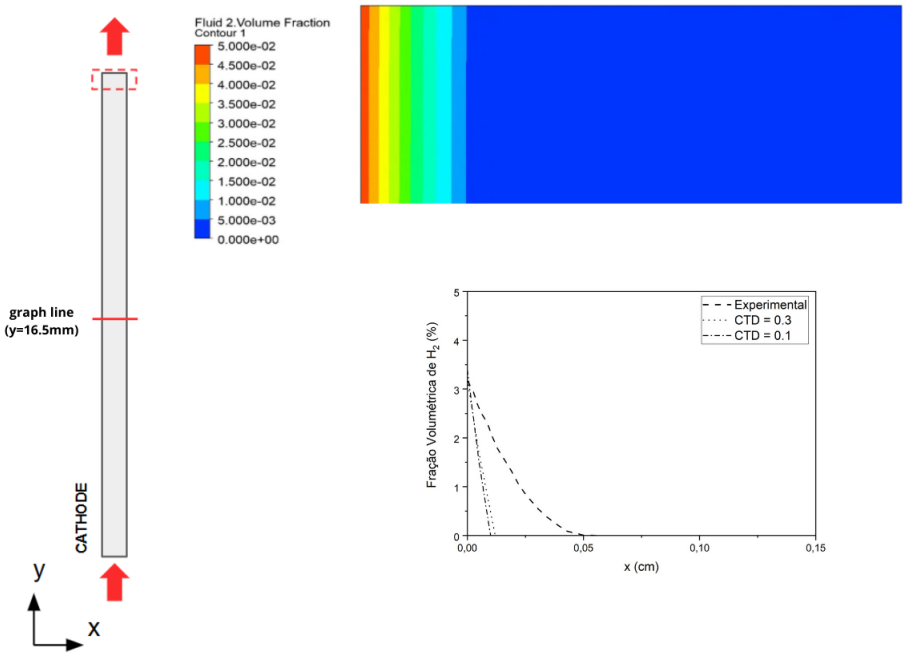

Source: The Author.

Considering this, and to avoid future overestimations caused by an excessively high turbulent dispersion coefficient in the subsequent simulations applied to the geometry of this study, a value of C_{TD} = 0.1 was adopted as the most appropriate for representing the monodisperse two-phase flow case. The use of a conservative coefficient is advantageous, as it prevents overestimating the dispersion force, which could mask the real characteristics of the flow.

Figure 36a shows the polydisperse case, where the model was simulated with a bubble size range from 50 to 100 μm. The bubbles were evenly distributed across five different diameter size groups (20% of the total quantity of bubbles in each group), and initially, the effects of the drag force were simulated without considering turbulent dispersion, breakage, or coalescence. After that, simulations were conducted, varying the turbulent dispersion coefficient. Compared to the monodisperse case, the model exhibited different dynamics: the bubbles appeared more dispersed throughout the fluid domain. The division of the dispersed phase into groups of varying diameters resulted in a gas volume fraction that was more evenly distributed. Figure 36b shows the graphs comparing the model that includes only the drag force with those that incorporate different turbulent dispersion coefficients. In the case with only the drag force, the gas layer near the electrode is more concentrated than in the cases with turbulent dispersion, indicating that the turbulent dispersion force influences the flow by reducing gas accumulation near the electrode and promoting its distribution throughout the domain. However, similarly to the monodisperse case, varying the C_{TD} did not significantly affect the gas layer near the electrode. Therefore, as in the monodisperse case, a more conservative C_{TD} = 0.1 was selected to avoid overestimations in the subsequent simulations.

Figure 36 – Void fraction contours obtained with only-drag force and turbulent dispersion force cases with two different C_{TD} for the polydisperse cases

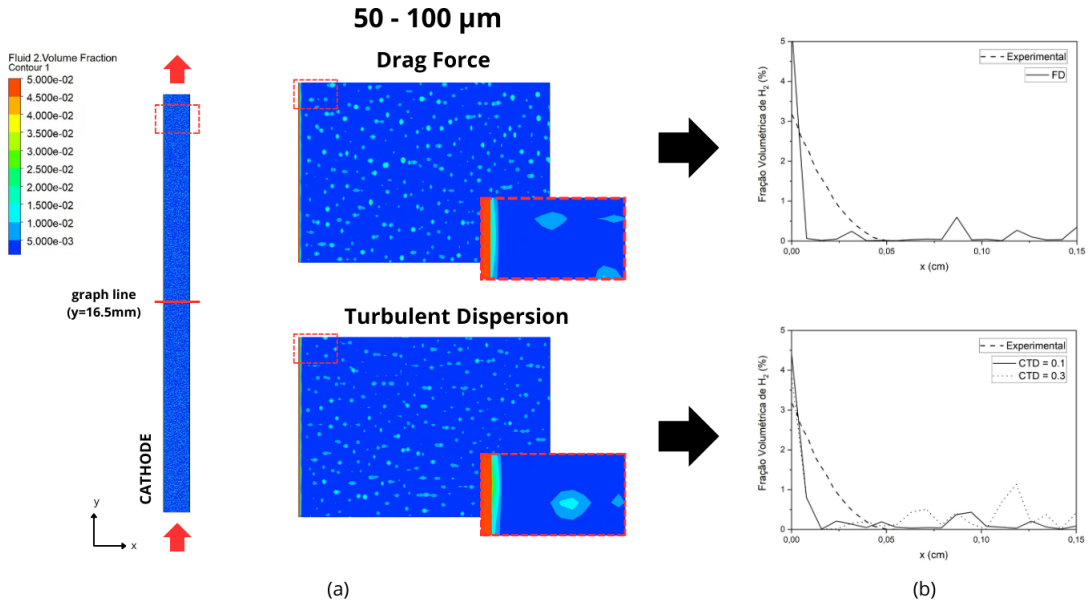

Source: The Author.

In order to assess the influence of the breakage and coalescence kernels, simulations were performed under two conditions: with coalescence only and with both coalescence and breakage simultaneously. The default values for the breakage and coalescence coefficients are typically set to 1, as defined by the software. However, since the objective of this study was to configure the model to better match the experimental results of Rodríguez e Amores (2020), these coefficients were changed.

Initially, simulations were carried out using only the Liao *et al.* (2015) coalescence model, as shown in Figure 37. The default coefficient value, $C_{Coalescence}$ = 1, demonstrated a decrease in the gas layer near x=0 on the electrode surface. This can be attributed to a high coalescence rate in the superficial layer that accelerates the formation of larger bubbles. Despite the larger bubble inertia, the increased surface area of these larger bubbles causes them to be more easily dragged from the electrode surface into the electrolyte, thereby reducing the bubble layer on the electrode. The value of 0.1 proved to be more conservative, maintaining a thin gas layer along the electrode surface. Therefore, this value was selected for subsequent simulations.

Figure 37 – Void fractions contours obtained with different coalescence coefficients

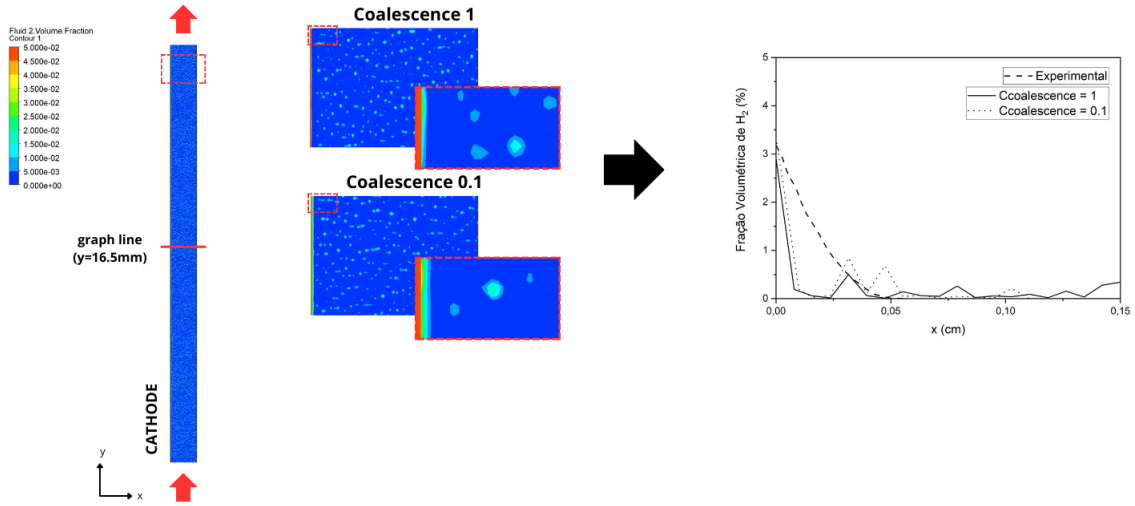

Source: The Author.

As with the coalescence coefficient, different bubble breakage coefficients, C_{Break} = 1, 0.1, and 0.01, were tested. As noted in Figure 38, the increase of the breakage coefficient contributed to a reduction in the gas concentration near the electrode surface. Even for the smallest breakage coefficient, a slight redistribution of gas was observed, likely due to velocity fluctuations that enhance local breakup rates. Considering the coalescence model is active, the bubbles grow through coalescence and then break into smaller bubbles, reducing the gas layer thickness. The inertia of small bubbles is lower, which makes them more sensitive to fluctuations in the electrolyte flow, is the reason for bubble release. Therefore, a more conservative approach was adopted by using a breakage coefficient of 0.01, reducing the breakage and avoiding excessive bubble fragmentation.

Figure 38 – Void fractions contours obtained with different breakage coefficients

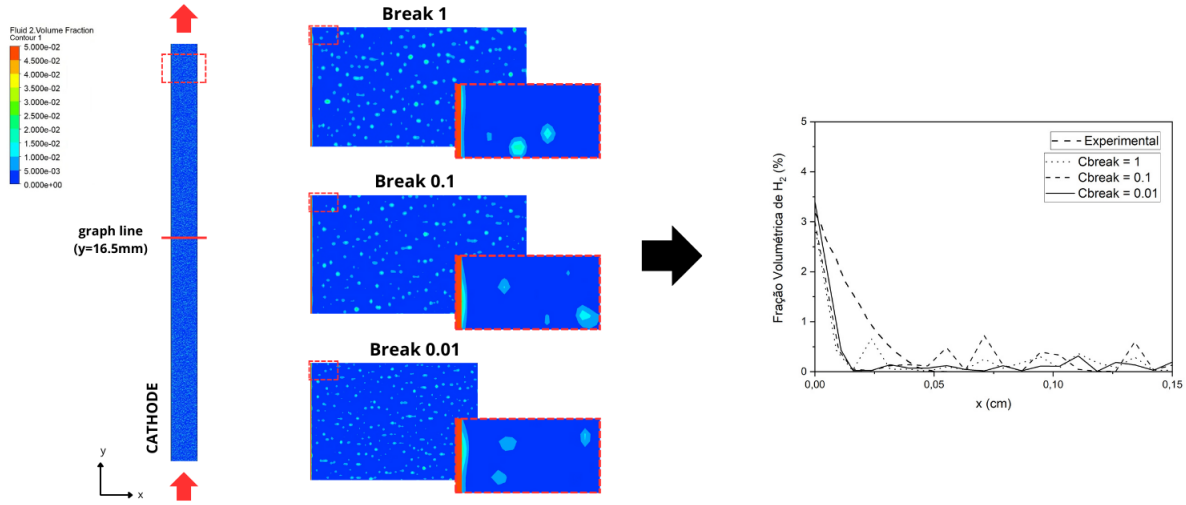

Source: The Author.

Figure 39 presents the results for the final case tested in the calibration process, which included the remaining relevant interfacial forces: the wall lubrication force (F_{WL}), the lift force (F_L), and the effects of bubble-induced turbulence. The addition of these forces had the main impact on the formation of a more stable gas layer on the electrode surface, representing a physical behavior more consistent with experimental observations.

The lift force (F_L) significantly contributed to deflecting the bubbles toward the wall, while the wall lubrication force (F_{WL}) acted to repel them, preventing their direct adhesion to the electrode. This balance of forces, where the F_L approximates the bubbles to the wall and the F_{WL} repels them, promotes a more diffuse distribution of the gas phase along the electrode surface.

Finally, the bubble-induced turbulence intensified local dispersion, supporting the redistribution of bubbles and preventing excessive accumulation in specific regions, which directly contributes to the homogenization of the gas layer at the electrode–electrolyte interface.

Figure 39 compares the gas volume fraction obtained experimentally with that calculated by the calibrated numerical model. Although the absolute values obtained in the simulation did not closely match the experimental results, the simulated curve reproduced a characteristic pattern of electrolysis systems, particularly regarding the formation and growth of the gas layer near the electrode.

Figure 39 – Comparison of void fraction contours and curve obtained from the simulation after model calibration

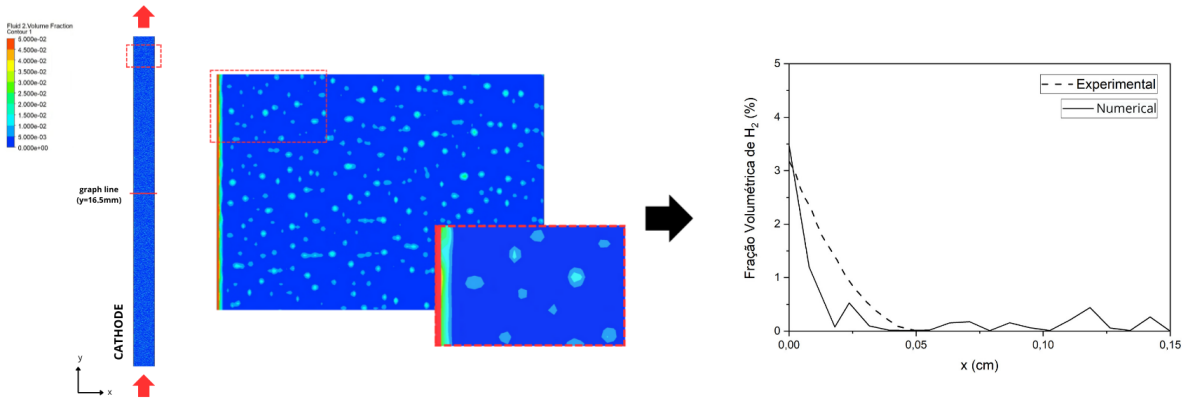

Source: The Author.

4.2 Case Study – TUClausthal Geometry

This section presents the results and discussions obtained from computational simulations carried out using a geometry based on the experimental study developed by Technische Universität Clausthal (TU Clausthal), in Germany.

The final configuration of the numerical model was established after a series of sensitivity analyses and calibrations. For the monodisperse simulations, the model incorporated the drag

force (F_D) and turbulent dispersion force (F_{TD}), with a conservative dispersion coefficient of 0.1. For the polydisperse case, the model was extended to include not only F_D and F_{TD} (also with a coefficient of 0.1), but also the wall lubrication force (F_{WL}), the lift force (F_L), and the population balance model with a coalescence coefficient of 0.1 and a breakage coefficient of 0.01.

Six different scenarios were tested, aiming at comparisons that highlights the effects of gas bubbles on the electrolyte flow hydrodynamics. The simulated cases include:

- A single-phase flow (electrolyte only);
- Three monodisperse two-phase flows, with bubble diameters of 50, 100, and 200 μm;
- Two polydisperse two-phase flows, with diameter ranges of 50–100 μm and 100–200 μm;

Figure 40 presents the velocity contour for the first three scenarios: the single-phase case, the monodisperse two-phase case with 50 μm bubbles, and the polydisperse two-phase case with bubbles ranging from 50 to 100 μm. All simulations were conducted with an electrolyte volumetric flow rate of 50 mL/min. The velocity profiles are shown in the YZ and XY planes to better visualize the flow behavior along the cell height and width.

As noted, the velocity contour for the single-phase flow case is symmetric in XY plane and well developed along the y-axis, with peak velocities centered in the axial region.

In the monodisperse two-phase flow case, there is a significant change in the velocity pattern. The presence of bubbles promotes a redistribution of the velocity field, with low-velocity zones near the walls and concentrated high-velocity regions near the electrode, suggesting the influence of buoyancy and bubble dispersion.

In the polydisperse two-phase case (50–100 μm), the flow exhibits a smoother and more evenly distributed velocity profile, with lower peak intensity. This trend may be related to the coexistence of bubbles of different sizes, which could promote additional momentum exchange and dispersion effects within the flow. Larger bubbles may generate local velocity perturbations, while smaller ones, due to their lower inertia, tend to follow the liquid motion more closely. The combined action of these mechanisms might contribute to a more homogeneous velocity field and less pronounced gradients.

This initial comparison highlights how the presence and size distribution of bubbles directly influence the flow structure, affecting both the velocity profile and the flow magnitude.

Figure 40 – Comparison of electrolyte velocity contours in single-phase, monodisperse two-phase flow, and polydisperse two-phase flow

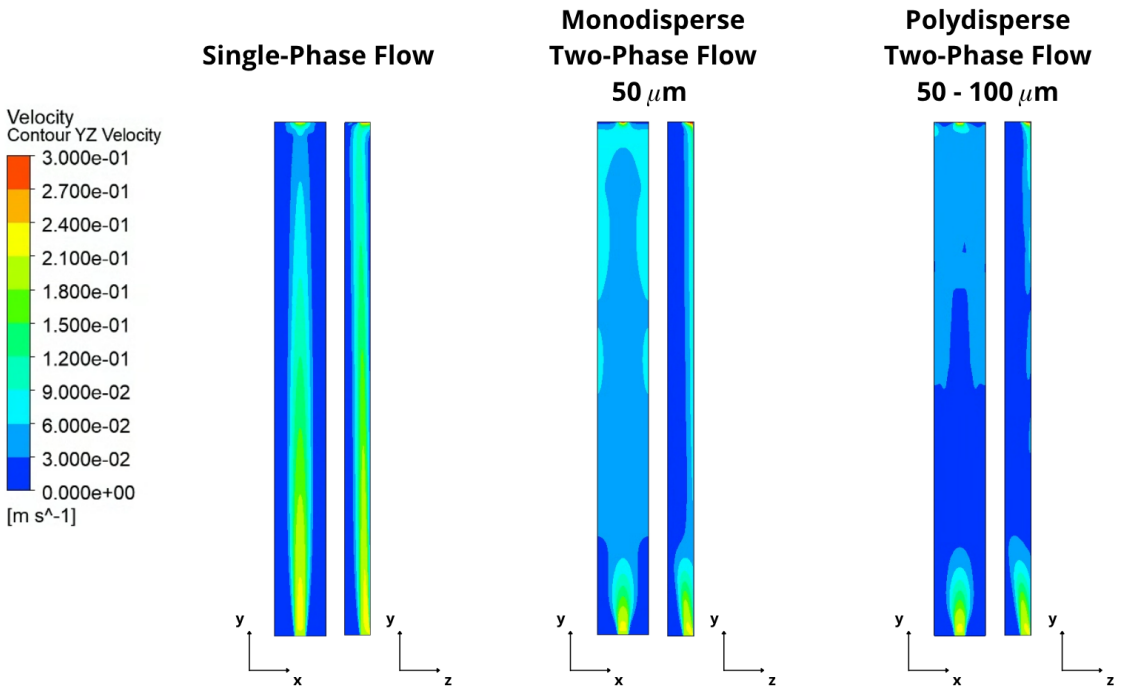

Source: The Author.

4.2.1 Evolution of the Velocity Profile Along the Geometry

Figure 41 shows the evolution of the electrolyte velocity profile for the single-phase case, with a flow rate of Q = 50 mL/min, at different positions along the vertical axis of the cell (y = 5 mm, 50 mm, and 95 mm). The velocity curves were extracted in two orientations: side view (YZ plane) and front view (XY plane), aiming to characterize the flow near the inlet (5 mm), middle section (50 mm), and upper part (95 mm) of the cell.

At the inlet (y = 5 mm), the velocity profiles are asymmetric and exhibit low magnitudes, indicating that the flow is still forming under the influence of boundary conditions. In the intermediate region (y = 50 mm), the profile is already partially developed, with increasing central velocities and the onset of a velocity gradient typical of laminar flow. Near the outlet (y = 95 mm), a parabolic profile is observed, characteristic of a fully developed laminar flow, in both the XY and YZ planes. This behavior is expected for the studied regime, in which the electrolyte flows between flat electrodes at low velocities, with a predominance of a single-phase laminar flow.

Figure 41 – Comparison of electrolyte velocity profiles along the geometry in the single-phase case for Q = 50 mL/min

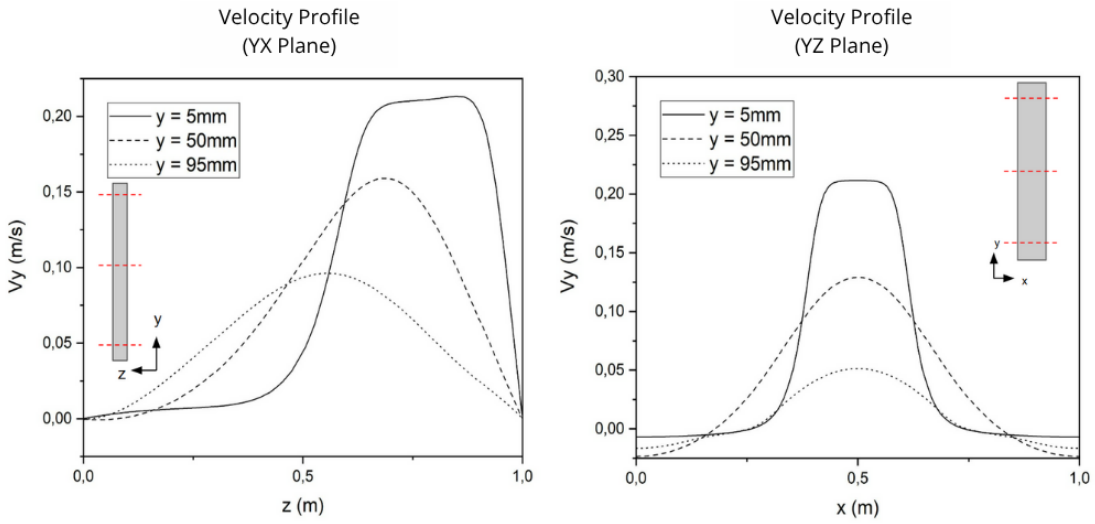

Source: The Author.

Figure 42 presents a comparison of the electrolyte velocity profiles for the monodisperse two-phase cases, with bubble diameters of 50, 100, and 200 μm. Additionally, the single-phase case was included for comparison. All cases simulated with a flow rate of Q = 50 mL/min. As in the single-phase case, velocity curves were extracted in the YZ (side) and XY (front) planes, at positions y = 5 mm, 50 mm, and 95 mm along the height of the cell.

As observed, the electrolyte flow pattern undergoes significant changes with the introduction of the gas phase. In all two-phase flow cases, a marked deceleration of the electrolyte is observed in the lower region of the cell (y = 5 mm) when compared to the single-phase flow case. This effect is attributed to the interference of gas dispersion in the pressure gradient, which causes a flattening of the velocity profile. This behavior was also reported by Boissonneau e Byrne (2000), who associated it with bubble-induced turbulence.

In contrast, in the upper region of the cell (y = 95 mm), the profiles show an increase in electrolyte velocity, indicating the action of the gas-lift effect. This phenomenon results from the rise of gas bubbles, which drag the liquid upward, accelerating the local flow. The profile at this height reflects the combined effect of reduced flow resistance and the buoyant force generated by the gas phase. Furthermore, the increase in diameter results in a velocity profile more rounded and displaced in relation to the electrode wall.

As discussed in the force sensitivity analysis, this effect was due to the turbulent dispersion force acts more intensely on larger bubbles, promoting a more effective homogenization of the superficial gas layer. As a result, the redistribution of bubbles directly affects the electrolyte velocity profile, demonstrating the strong influence of hydrodynamic interaction between the phases.

Figure 42 – Comparison of electrolyte velocity profiles along the geometry in the monodisperse two-phase case for Q = 50 mL/min

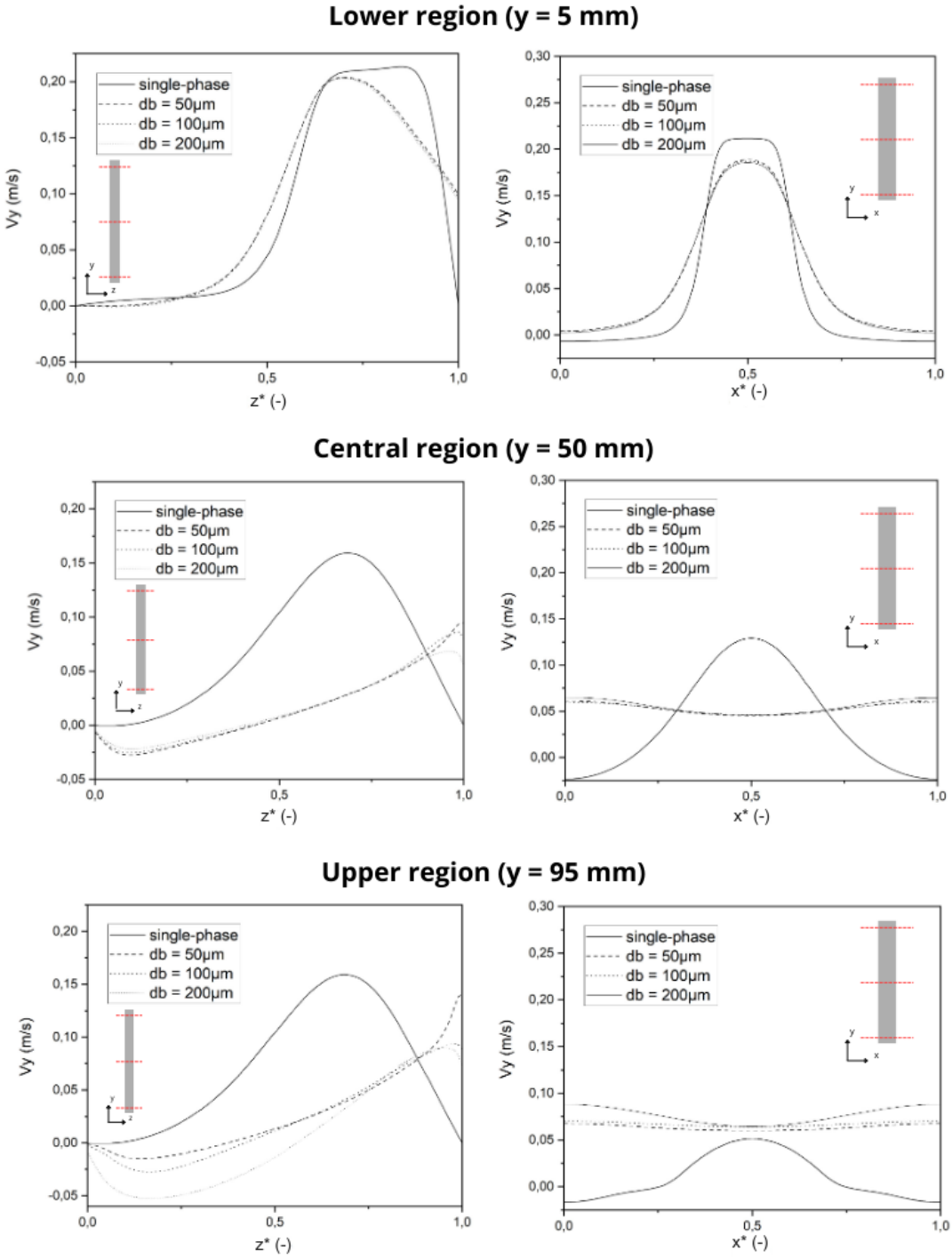

Source: The Author.

Figure 43 presents the electrolyte velocity profiles in the YZ and XY planes for the polydisperse two-phase cases. As previously shown for the monodisperse case, a comparison was also performed for the polydisperse case, considering bubble diameter ranges of 50–100 μm and 100–200 μm. Additionally, the single-phase case was included to enable a reference com-

parison. The profiles were extracted at the same vertical positions: y = 5 mm, 50 mm, and 95 mm.

As shown in the YZ plane, both cases share a similar behavior in the initial and intermediate regions of the cell (y = 5 mm and y = 50 mm), indicating that the flow is influenced by a comparable bubble distribution dynamic up to half of the cell height. This similarity results from the combined action of the different bubble size groups in the MUSIG model, which promotes a more balanced dispersion of the gas phase in the lower portion of the domain.

However, the effects of bubble diameter become more evident in the upper section (y = 95 mm). The velocity profile for the 50–100 μm case shows higher values, close to the walls, indicating that part of the gas remains adhered to the electrode surface. This behavior is typical of regions with a stronger gas-lift effect, which favors liquid acceleration near the wall.

In contrast, the maximum velocity position for the 100–200 μm case is displaced from the wall, while the velocity near the electrode boundary approaches zero. This indicates that the gas phase no longer adheres to the surface, which results in a more centralized flow.

Both cases exhibit noticeable electrolyte recirculation between positions 0 and 0.5 along the z-axis at y = 95 mm, with this effect being more pronounced in the case with smaller bubbles. This behavior reflects the influence of a larger number of small bubbles, which tend to accumulate and circulate for longer periods in the upper cell regions, promoting stagnation zones and fluid backflow. In the XY plane, the analysis reveals that both polydisperse cases display a progressive acceleration profile of the electrolyte in the upper half of the geometry, with the curve at y = 95 mm reaching the highest values. This effect is directly associated with the upward buoyancy promoted by the accumulation of bubbles in the upper cell regions.

Figure 43 – Comparison of electrolyte velocity profiles along the geometry in the polydisperse two-phase flow case for Q = 50 mL/min

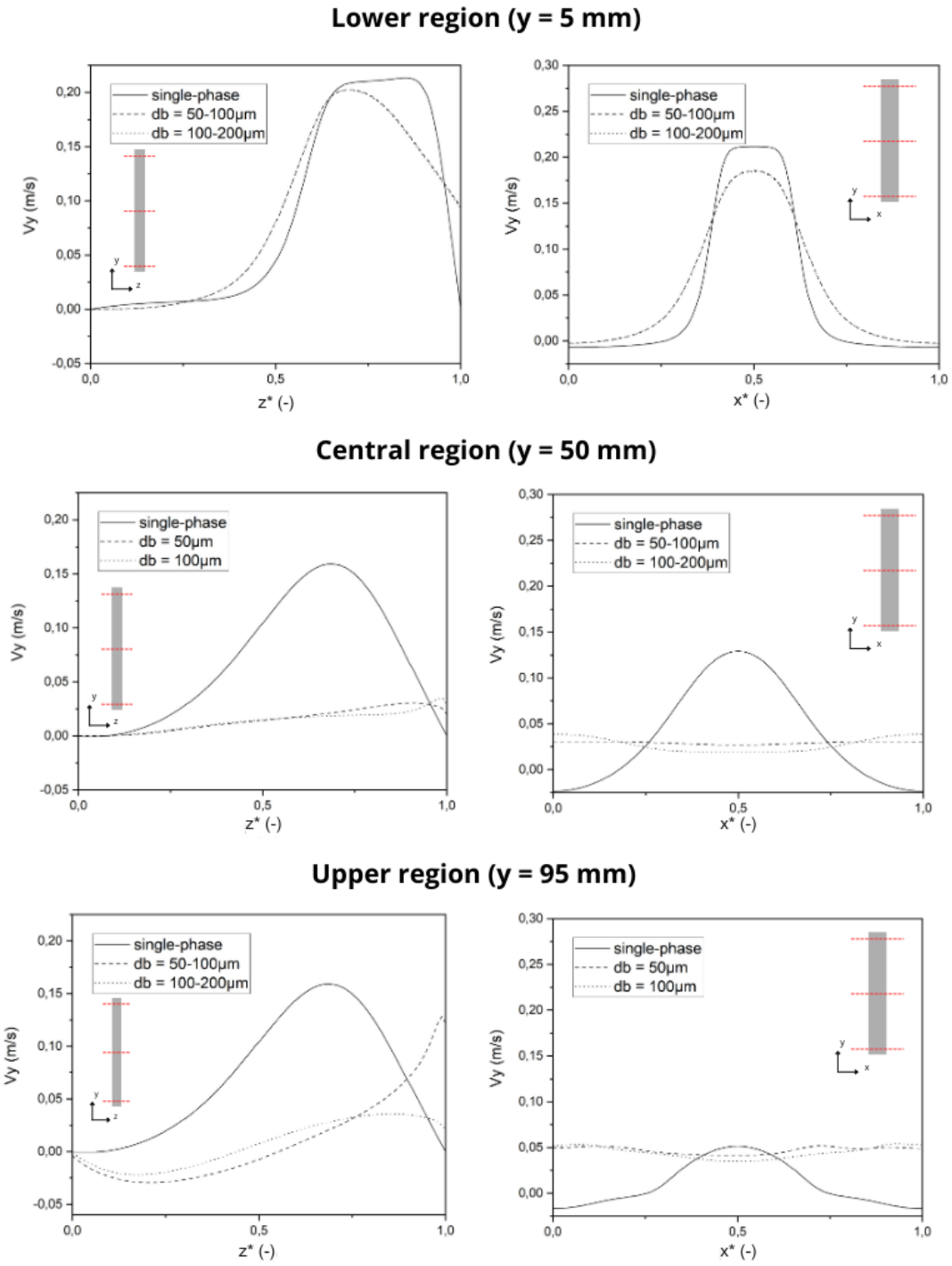

Source: The Author.

4.2.2 Gas Phase Distribution – Monodisperse Two-Phase Flow

The flow pattern of each case directly influences how hydrogen bubbles are distributed throughout the cell geometry. Figure 44 shows the volume fraction contours of the gas phase

in the YZ planes for the monodisperse two-phase flow cases, with bubble diameters of 50, 100, and 200 μm.

Figure 44 – Gas volume fraction distribution in the monodisperse two-phase flow case for different bubble diameters - Scale from 0 to 1

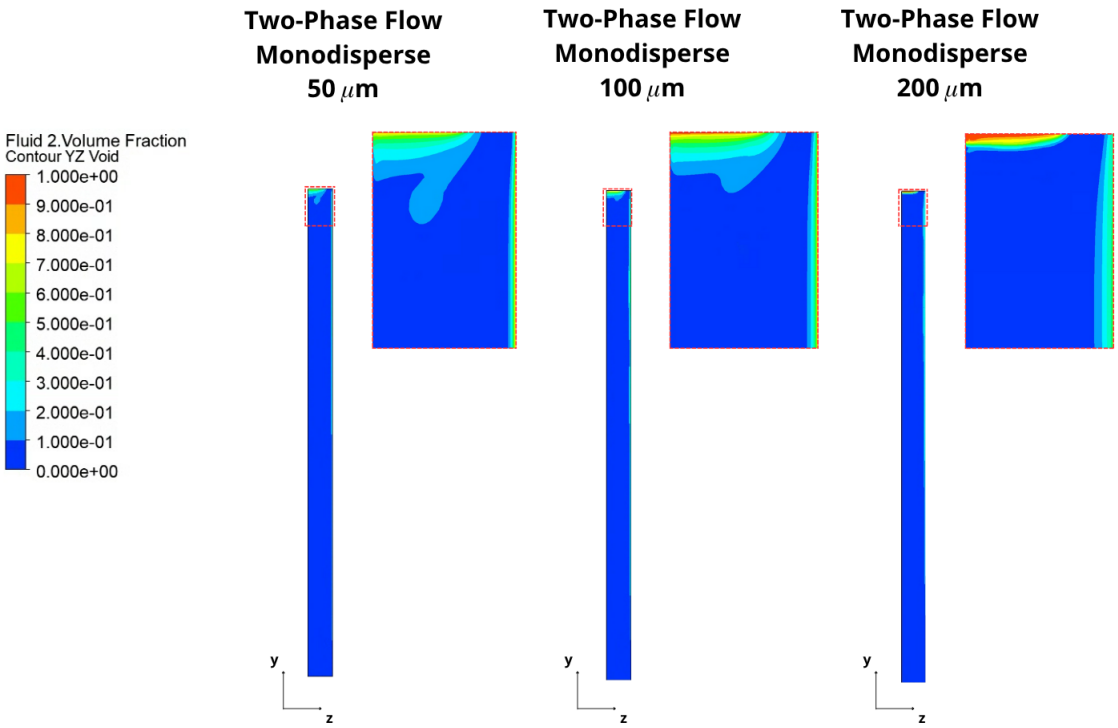

Source: The Author.

As noted, the smaller the bubble diameter, the higher is bubble dispersion near the outlet; the bubble distribution changes significantly with bubble diameter accross the domain. The gas volume fraction is more spread out along the upper region of the cell for 50 μm bubbles, forming a longer and more diffuse gas layer. This pattern indicates greater dispersion, favored by the lower inertia of the bubbles. A more intense concentration of the gas phase is observed in the upper region of the domain for 100 μm bubbles, with the formation of a visibly thicker layer near the electrode. In the case of 200 μm bubbles, the gas concentration becomes even more pronounced, forming a compact layer at the domain outlet. This transition from a diffuse pattern (50 μm) to a concentrated one (200 μm) illustrates the critical role of bubble diameter in two-phase flow regimes. Figure 45 shows the distribution of the gas volume fraction in the geometry on a scale from 0 to 0.1, to better visualize the bubble distribution.

Figure 45 – Illustration of gas dispersion variation in the monodisperse two-phase case with increasing bubble diameter - Scale from 0 to 0.1

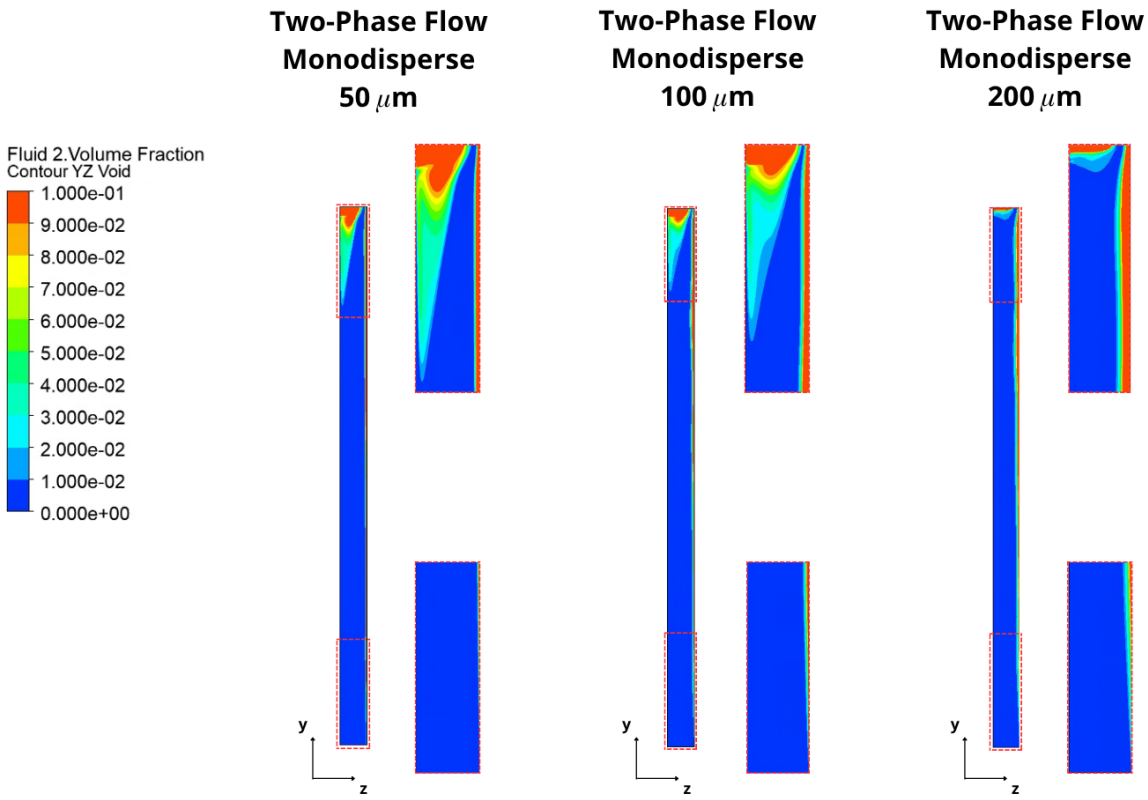

Source: The Author.

To evaluate the amount of gas trapped within the flow domain, the average void fraction was calculated using CFX Post for three monodisperse two-phase flow cases with a fixed volumetric flow rate of 50 mL/min and varying bubble diameters of 50, 100, and 200 μm. The results show a gradual increase in the average void fraction as the bubble diameter increases, with values of 2.66%, 2.83%, and 2.98%, respectively, as shown in Table 5. These findings indicate that increasing the bubble diameter does not reduce the amount of gas retained in the system. On the contrary, it leads to a more concentrated gas layer within the domain, suggesting a change in the distribution of the dispersed phase rather than a decrease in its total volume. A broader analysis considering different electrolyte flow rates will be presented in the following sections to further explore this behavior.

Table 5 – Average gas volume fraction for different bubble diameters for monodisperse case (Q = 50 mL/min)

Bubble Diameter	Void Fraction (%)
50 μm	2.66
100 μm	2.83
200 μm	2.98

Source: Author.

To better visualize the influence of bubbles on the flow, an analysis of the electrolyte streamlines was carried out. Figure 46 presents the electrolyte velocity streamlines for the monodisperse two-phase cases with 50, 100, and 200 μm bubbles, as well as for the single-phase case, for comparison purposes.

Recirculation region is observed in the upper part of the cell, near the outlet for the single-phase flow case. This behavior is attributed to the geometric restriction imposed by the small outlet, which induces the formation of low-pressure zones that favor electrolyte recirculation. The flow still exhibits the formation of a vortex near the outlet for the two-phase flow case, which promotes the recirculation of the electrolyte. Nevertheless, a new flow dynamic is observed when the bubbles are introduced. Recirculation is intensified by the presence of the bubbles for the 50 μm bubbles case, resulting in gas entrapment along the electrode outer wall. The smaller bubble diameter favors gas accumulation in recirculation zones. As the bubble diameter increases (100 and 200 μm), the bubbles rise faster and disperse less due to their larger diameter, reducing the amount of gas retained near the side walls and modifying the recirculation pattern. This results in a more organized flow structure, with less gas entrapment at the boundaries. The effect of increasing diameter can also be seen in the three-dimensional streamlines, showing that the larger the bubbles, the more intense and concentrated their distribution becomes.

This analysis suggests that bubble diameter directly influences the phase interaction, affecting both the efficiency of gas removal and the electrolyte flow pattern. The presence of recirculation zones, associated with the flow tendencies imposed by the geometry, favors gas entrapment, which can negatively impact the cell's performance by reducing the hydrogen release rate.

Figure 46 – Demonstration of electrolyte velocity streamlines for monodisperse two-phase flow cases

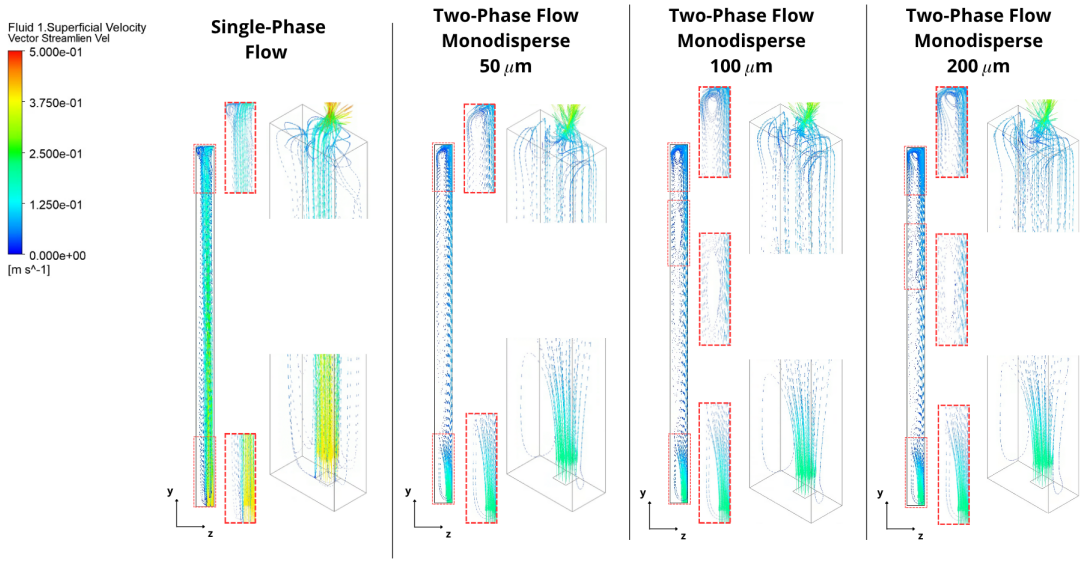

Source: The Author.

4.2.3 Gas Phase Distribution – Polydisperse Two-Phase Flow

Figure 47 presents the gas phase volume fraction contours for the polydisperse cases with bubble diameter ranges of 50–100 μm and 100–200 μm. Compared to the monodisperse cases, a substantial change in the distribution of the dispersed phase is observed, particularly the reduction of high-concentration bubble regions, indicating a more homogeneous behavior.

The polydisperse model demonstrated a greater ability to represent the dynamic behavior of hydrogen gas, as the division into distinct size groups allows bubbles to respond differently to the interfacial forces present in the flow. Smaller bubbles, for example, have lower inertia, making them sensitive to drag force (F_D) and turbulent dispersion (F_{TD}). The drag force contributes to maintain small bubbles aligned with the main fluid stream, causing them to be attracted to recirculation zones.

Larger bubbles, on the other hand, due to their greater inertia and volume, are less affected by turbulent fluctuations and tend to follow a more linear trajectory. In contrast, the lift force (F_L) induces significant lateral migration for micrometric bubbles, deflecting them toward the wall and explaining their accumulation near the electrode. Additionally, the wall lubrication force (F_{WL}) becomes particularly relevant for these larger bubbles near the wall, acting locally to prevent them from adhering directly to the electrode surface. This heterogeneity among bubble groups results in a more complex multiphase flow, characterized by distinct patterns of dispersion, entrapment, and lateral migration throughout the cell.

The simulations reveal the formation of a gas entrapment region that recirculates predominantly near the cell outlet for the 50–100 μm case. The lower inertia of these bubbles allows them to be more easily captured for recirculation zones. The continuous action of the turbulent

dispersion force within these vortices promotes bubble spreading, which indirectly hinders their coalescence and favors the formation of a diffuse gas layer.

By raising the bubble size range to 100–200 μm, the gas phase exhibits reduced dispersion compared to smaller bubbles, forming a more concentrated layer in the upper region of the cell, with accumulation zones adjacent to the electrode wall. The higher inertia of larger bubbles combined with the effect of the lift and the wall lubrication force contributes to the formation of localized gas pockets that cannot fully disperse due to the reduced influence of turbulent dispersion. On the other hand, these reduce gas entrapment in the vortices.

Figure 47 – Hydrogen volume fraction contours for the polydisperse two-phase cases

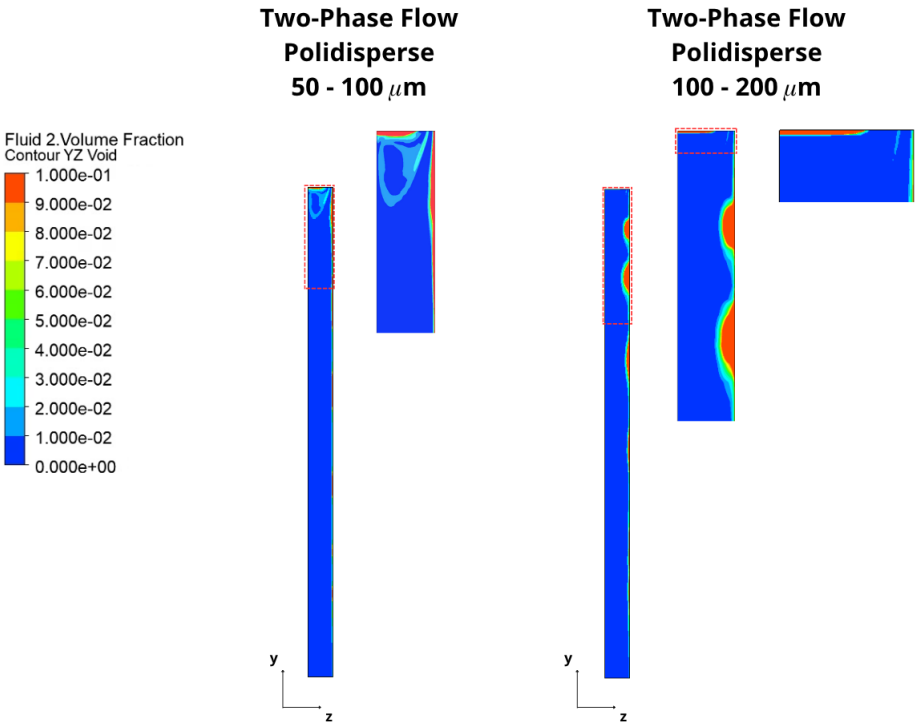

Source: The Author.

To evaluate the amount of gas trapped within the flow domain in the polydisperse case, the average void fraction was also calculated in CFX-Post for two configurations with the same volumetric flow rate of 50 mL/min but different bubble diameter ranges: 50–100 μm and 100–200 μm. The results show an increase in the average void fraction from 1.19% to 1.26%, as shown in Table 6. Unlike the monodisperse case, the polydisperse case exhibited a lower overall amount of gas trapped within the domain, suggesting that the dynamics between bubble size groups result in different gas retention patterns. However, similar to the monodisperse case, the amount of gas increases with the larger range of bubble size groups.

Table 6 – Average gas volume fraction for different bubble diameters for polydisperse case (Q = 50 mL/min)

Bubble Diameter	Void Fraction (%)
50-100 μm	1.19
100-200 μm	1.26

Source: Author.

In addition to the analysis of the total gas volume fraction, the distribution of size fractions for each bubble group was evaluated throughout the domain, with the aim of gaining a deeper understanding of the internal dynamics of the polydisperse model and the effects of the breakage and coalescence kernels. Figure 48 presents the volume fraction contours for each of the five bubble size groups, comparing the polydisperse cases with diameter ranges of 50–100 μm and 100–200 μm.

Figure 48 – Evolution of bubble diameters within the domain

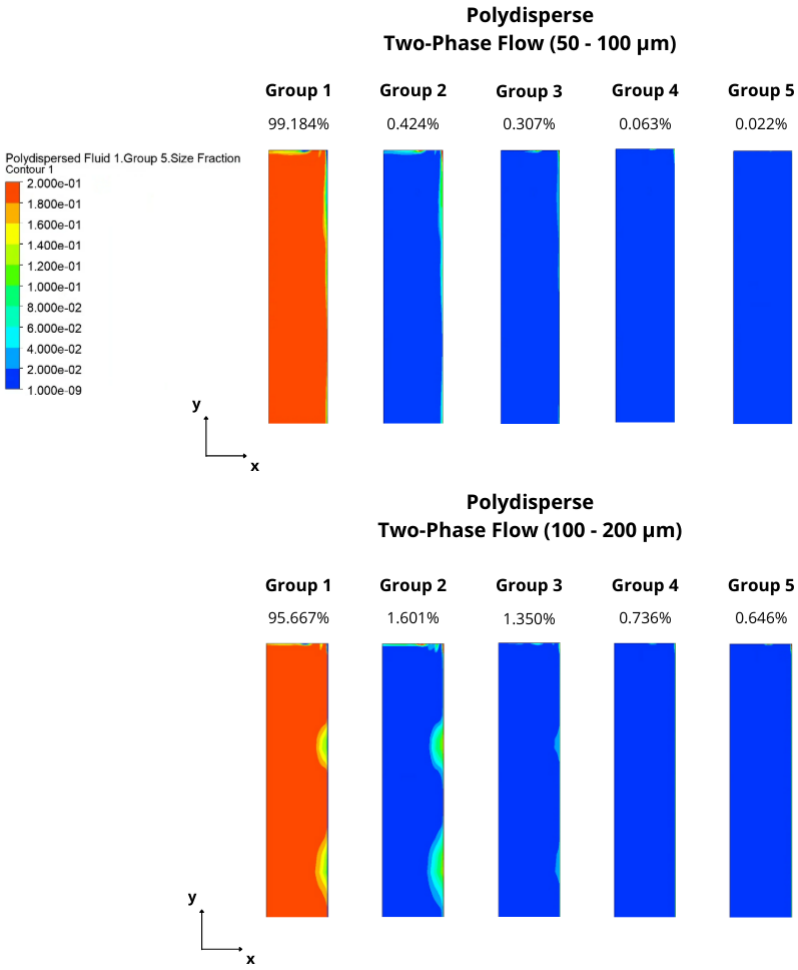

Source: The Author.

As previously defined, both simulations considered a uniform inlet condition, where all five groups were injected with the same volume fraction through the electrode wall. However,

the analysis of the results reveals that, even under identical initial conditions, Group 1 (smaller bubbles) prevails almost over the entire domain.

This dominance is visually evident in the wide regions where Size Fraction Group 1 reaches values close to 100% in both cases. This indicates that the larger bubbles (Groups 2 to 5) were rapidly broken up shortly after entering the electrolyte flow. Even with a conservative breakage coefficient (C_{Break} = 0.01), the velocity gradients and local turbulence were sufficient to promote the fragmentation of larger bubbles, highlighting the model's high sensitivity to the analyzed flow regime.

On the other hand, coalescence ($C_{Coalescence}$ = 0.1) was not sufficiently effective in reversing this process. Once formed, small bubbles do not coalesce frequently enough to generate larger groups, resulting in a population dominated by the smallest bubble size classes. The larger bubble groups were identified only in very localized regions, such as at the electrode wall (injection point) and in gas accumulation zones or recirculation areas, where the local flow dynamics may temporarily favor the existence of larger bubbles before they are eventually fragmented. This tendency is even more pronounced in the 50–100 μm case. On the other hand, the 100–200 μm configuration showed a slight increase in the quantity of bubbles from other groups, with Group 1 accounting for 95% of the total number of bubbles, compared to 99% in the 50–100 μm case, mainly due to the gas pockets trapped near the electrode. The previously observed gas entrapment vortex (as discussed in the streamline section) was found to consist almost exclusively of Group 1 bubbles, confirming that gas accumulation in this region was primarily of small bubbles, which were generated through breakage and did not evolve into larger groups.

Tables 7 and 8 present the percentage of bubbles belonging to each group at three heights along the geometry (y = 5, 50, and 95 mm), extracted from the same analysis (in the YZ plane) shown in Figure 48. It can be observed that, throughout the entire flow region, Group N1 was predominant, accounting for approximately 99% of the total number of bubbles. Although the remaining groups exhibited low incidence, differences between the two analyzed cases can still be identified.

For the diameter range of 50–100 μm, the occurrence of Groups N2 to N5 was lower compared to the 100–200 μm case, indicating that the evolution toward larger groups is more pronounced when the initial bubble range is also larger. Moreover, in the 50–100 μm case, Group N5 showed a reduction in percentage at y = 95 mm compared to y = 50 mm, suggesting that the upper region of the domain favored the breakup of these bubbles into smaller sizes.

In contrast, in the 100–200 μm case, the reduction was not limited to Group N5 but also occurred in Groups N2, N3, and N4. This behavior resulted in a relative increase of Group N1, demonstrating that as the initial bubble diameter increases, fragmentation also extends to the intermediate groups, reinforcing the predominance of smaller bubbles (N1).

Table 7 – Probability of occurrence for bubble size groups (50–100 μm range)

Position (Y)	N1 (%)	N2 (%)	N3 (%)	N4 (%)	N5 (%)
Y = 05 mm	99.99466	0.00372	0.00148	0.00011	0.00003
Y = 50 mm	99.99591	0.00279	0.00115	0.00013	0.00003
Y = 95 mm	99.95384	0.03143	0.01300	0.00144	0.00029

Source: Author.

Table 8 – Probability of occurrence for bubble size groups (100–200 μm range)

Position (Y)	N1 (%)	N2 (%)	N3 (%)	N4 (%)	N5 (%)
Y = 05 mm	99.974	0.017	0.007	0.001	0.001
Y = 50 mm	99.950	0.030	0.014	0.003	0.002
Y = 95 mm	99.975	0.017	0.007	0.001	0.000

Source: Author.

To further understand the interaction between the liquid and gas phases and the influence of bubble size on hydrodynamics, a comparative analysis of the electrolyte streamlines was also conducted, between the single-phase and polydisperse two-phase cases with bubble diameter ranges of 50–100 μm and 100–200 μm, as shown in Figure 49.

The electrolyte surface velocity streamlines reinforce the differences in flow patterns between the monodisperse and polydisperse two-phase cases. Both cases significantly altered the recirculation regions compared to the single-phase flow, with vortices appearing smaller and more concentrated in the upper extremity of the geometry.

Recirculation zones are observed along the opposite face of the electrode throughout the cell upper half for the smaller bubble case. In contrast, the vortex becomes smaller for larger bubbles. The effect of turbulence dissipation generated by larger bubbles decelerates the electrolyte, allowing the bubbles to recirculate and be directed into the main flow plume. As a result, the polydisperse case with larger bubbles does not exhibit bubble entrapment, as the bubbles recirculate less and tend to be released more easily.

Figure 49 – Electrolyte velocity streamlines for polydisperse two-phase flow cases

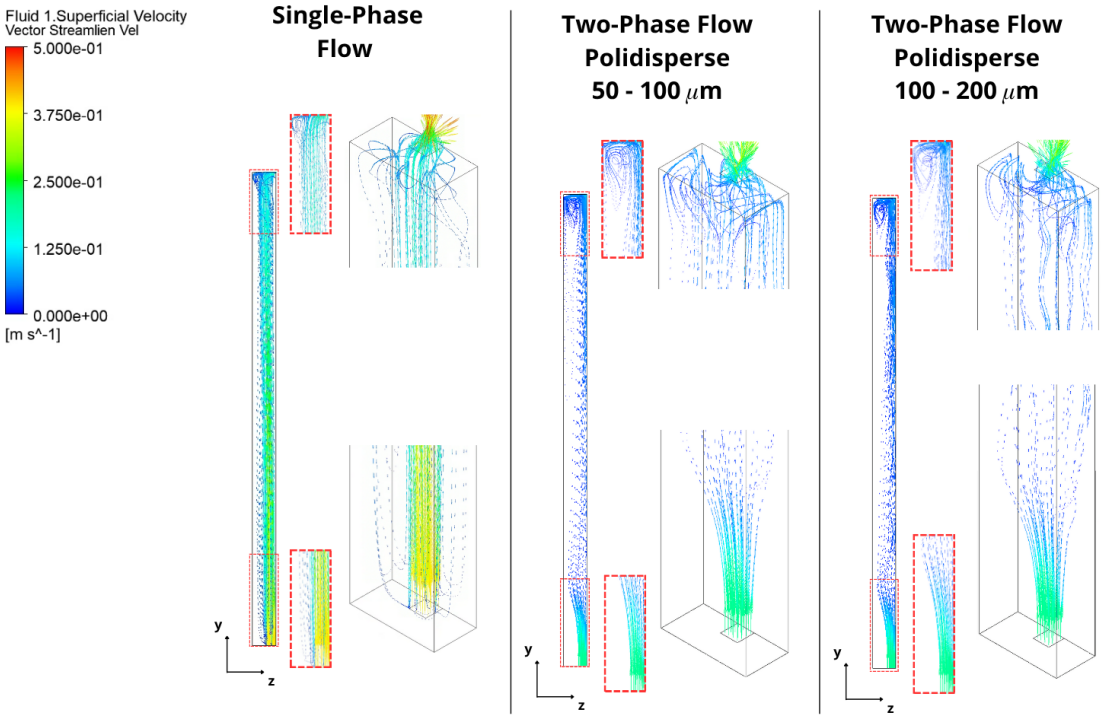

Source: The Author.

4.2.4 Influence of Electrolyte Flow Rate

To analyze the influence of the electrolyte volumetric flow rate on flow behavior and gas volume fraction distribution along the geometry, the cases that showed the largest gas dispersion were selected: the monodisperse two-phase case with 50 μm bubbles, and the polydisperse two-phase case with a bubble size range of 50 to 100 μm.

Both models were tested with three different electrolyte flow rates: Q = 30, 50, and 70 mL/min. These results were then compared to their corresponding single-phase cases, in order to enable a deeper analysis of flow patterns and the influence of increasing the electrolyte flow rate.

Figure 50 illustrates the evolution of the V_y velocity component of the electrolyte at three different heights: y = 5 mm, 50 mm, and 95 mm, for the three electrolyte volumetric flow rates. The velocity profiles for all three single-phase flow rates exhibit the characteristic development of a channel flow. Near the inlet, the profile tends to be more uniform, gradually evolving into a more parabolic or fully developed pattern in the middle of the channel, with maximum velocity at the center and lower values near the walls.

Figure 50 – Comparison of electrolyte velocity profiles along the geometry in the polydisperse two-phase case for different electrolyte volumetric flow rates

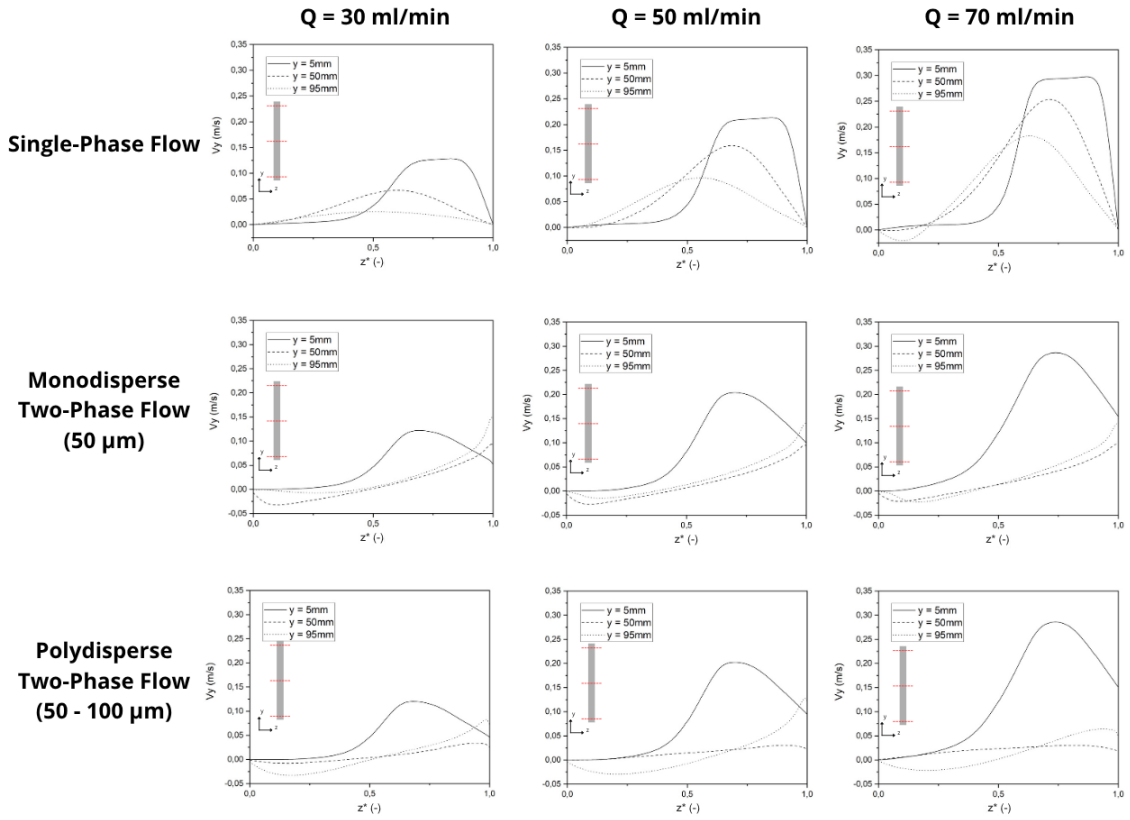

Source: The Author.

Near the outlet, the velocity magnifies along with greater recirculation in the region opposite the electrode, indicating the growth of a vortex at the upper end of the geometry, previously discussed in Figure 46 and Figure 49.

As previously noted, the introduction of 50 μm bubbles significantly alters the electrolyte velocity profiles compared to the single-phase case. At y = 5 mm, the velocity profile is strongly influenced by increasing the electrolyte flow rate.

At middle height, the region near the electrode remains unchanged across all three flow rates, indicating that the amount of gas did not vary. Near the outlet, recirculation along the wall opposite the electrode increases for the 70 mL/min flow rate, indicating that the vorticity tends to grow with higher electrolyte velocity. Meanwhile, the upward gas velocity does not reduce near the electrode, and the curve shape continues to reflect the influence of the gas-lift effect caused by the presence of bubbles. Therefore, it can be concluded that the amount of bubbles remains similar across the three monodisperse cases.

As shown in Figure 50, the velocity profile at y = 5 mm for the polydisperse case follows the same pattern as observed in the monodisperse case. In all simulations, the curve at y = 50 mm does not change with the flow rate. For the profile closer to the outlet, a comparison between the 30 and 50 mL/min simulations reveals the expected increase in velocity magnitude

with increasing flow rate. However, the profile for the 70 mL/min case shows a different pattern. The region near the electrode exhibits a reduction in electrolyte velocity and produces a more flattened curve.

Figure 51 shows the electrolyte velocity contours, while Figure 52 presents the void fraction contours, both for the monodisperse and polydisperse cases.

The velocity contours of the monodisperse two-phase flow case, in Figure 51, maintained a more uniform flow as the electrolyte volumetric flow rate increased. At all flow rates, the velocity contours appeared symmetric in the XY plane, with higher velocities in the upper half of the geometry. In the YZ plane, the region along the electrode surface also experienced acceleration due to the increase in the electrolyte flow rate. The electrolyte velocity does not evolve smoothly as in the monodisperse case. The distribution of bubbles into different groups contributes to the formation of localized stagnation points and regions of higher acceleration throughout the domain.

The volume fraction contours and streamlines, in Figure 52, show that the gas concentration remained unchanged with increasing flow rate. However, the recirculation zone at the upper end of the geometry became more localized; streamlines show recirculation from the upper to the lower end for the 30 mL/min case. From the volume fraction contours and velocity streamlines, the increase in electrolyte flow rate contributes to the reduction of the vortex near the outlet, thereby enhancing the release of trapped gas. However, the gas accumulation region along the upper face of the geometry, near the square outlet, still exists but less concentrated.

Figure 51 – Comparison of electrolyte velocity contours along the geometry in the polydisperse two-phase case for different electrolyte volumetric flow rates

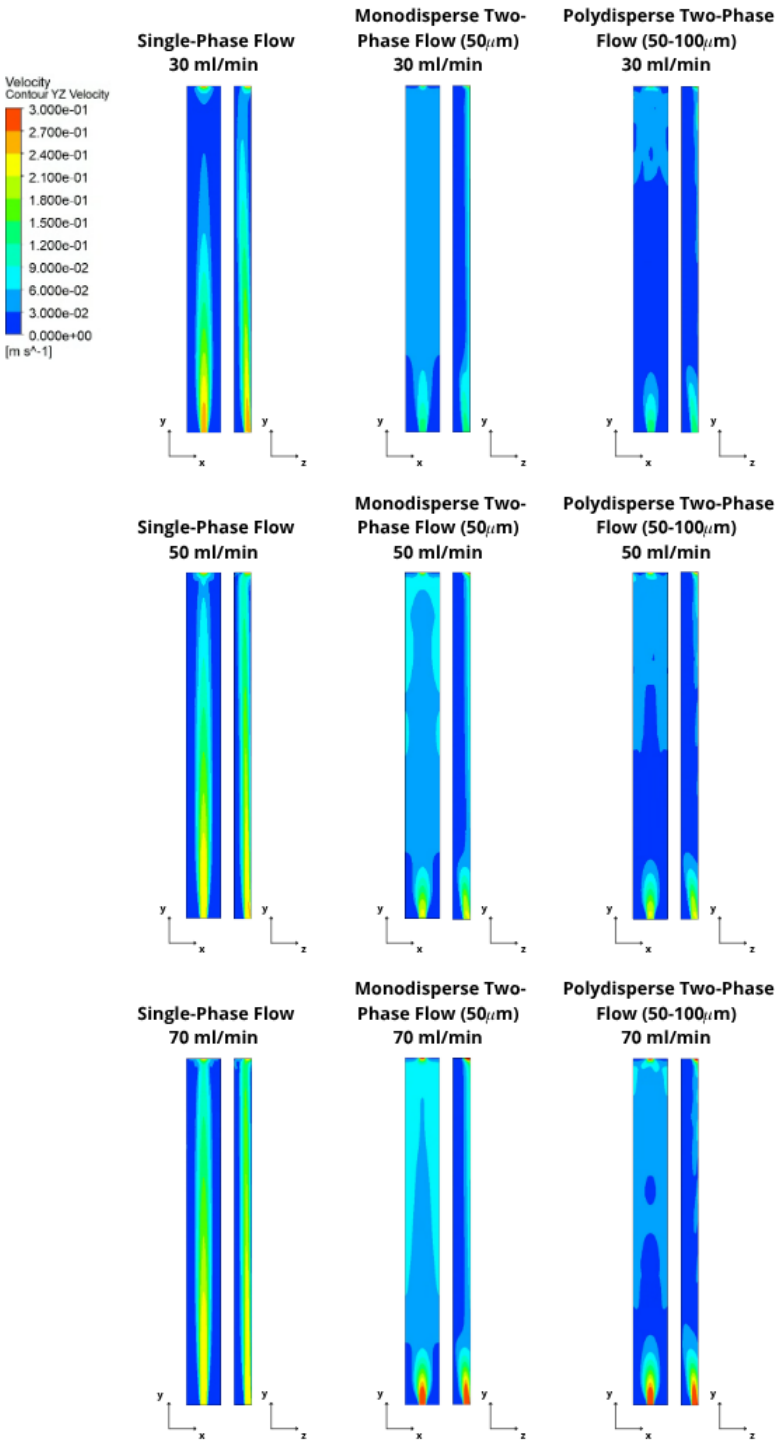

Source: The Author.

To evaluate the influence of bubble diameter and electrolyte flow rate on gas retention, Table 9 presents the average gas volume fraction obtained for the monodisperse case with diameters of 50, 100, and 200 μm, under three different flow rates: 30, 50, and 70 mL/min. As observed, increasing the bubble diameter results in a gradual increase in the average gas fraction across all flow rates. For instance, at Q = 30 mL/min, the void fraction rises from 2.881% for 50 μm to 3.132% for 200 μm. A similar trend is seen at Q = 50 and 70 mL/min. On the other hand, increasing the flow rate reduces the average void fraction for a given bubble size, suggesting that higher electrolyte velocities contribute to enhanced removal or dispersion of the gas phase, reducing its accumulation within the flow domain.

Table 9 – Average gas volume fraction for different bubble diameters in the monodisperse case

Bubble Diameter	Q = 30 mL/min	Q = 50 mL/min	Q = 70 mL/min
50 μm	2.881%	2.657%	2.503%
100 μm	3.042%	2.833%	2.698%
200 μm	3.132%	2.983%	2.891%

Source: Author.

In the polydisperse configuration, two bubble diameter ranges were analyzed: 50–100 μm and 100–200 μm. Table 10 summarizes the average gas volume fractions for each range under flow rates of 30, 50, and 70 mL/min. The results show a slightly higher void fraction for the 100–200μm range across all flow rates, indicating that larger bubbles tend to accumulate more gas within the domain. Unlike the monodisperse case, the average void fractions in the polydisperse case are significantly lower, remaining around 1.1–1.3%. This suggests that the distribution of bubble size groups in polydisperse systems promotes more effective dispersion and reduces gas retention. Furthermore, unlike the monodisperse results, increasing the flow rate does not consistently reduce the gas fraction, especially for the 100–200 μm case, which shows a slight increase from Q = 50 to Q = 70 mL/min, potentially due to dynamic interactions between bubble groups that enhance localized trapping.

Table 10 – Average gas volume fraction for different bubble diameter ranges in the polydisperse case

Bubble Diameter Range	Q = 30 mL/min	Q = 50 mL/min	Q = 70 mL/min
50–100 μm	1.250%	1.188%	1.130%
100–200 μm	1.295%	1.260%	1.270%

Source: Author.

Figure 52 – Comparison of gas void fraction contours along the geometry in the polydisperse two-phase case for different electrolyte volumetric flow rates

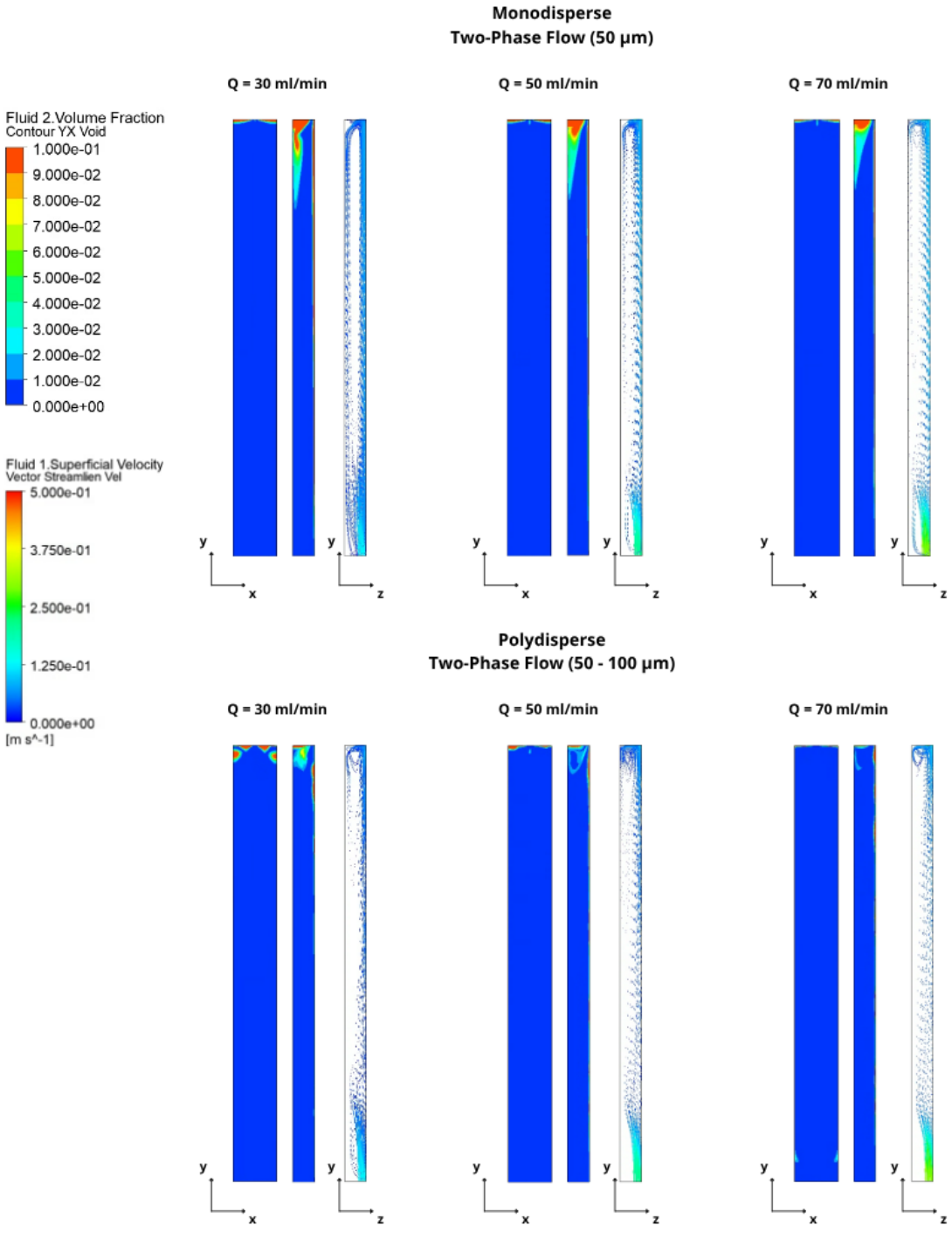

Source: The Author.

4.2.5 Influence of Gas Inlet Flow Rate

The final analysis conducted here addresses the influence of the gas volumetric inlet flow rate on the hydrodynamic behavior of the electrolyte. The variation of this parameter is directly

associated with the system energy density, as an increase in the electric current density enlarges the hydrogen production and, consequently, a higher gas flow into the cell.

In the previous simulations, a standard value of Q_g = 15 mL/min was adopted, corresponding to a current density of approximately 200 mA/cm², based on the experimental data from the TU Clausthal study. To expand the analysis, two additional flow rates were simulated, 10 and 20 mL/min, corresponding to estimated current densities of 130 mA/cm² and 260 mA/cm², respectively, as determined by Faraday's equations.

Figure 53 presents the electrolyte velocity profiles along the geometry for the monodisperse (50 μm) and polydisperse (50–100 μm) two-phase flow cases, considering different gas flow rates. A more uniform and predictable evolution of the flow is observed in the monodisperse case. The increase in gas flow rate results in higher electrolyte acceleration in the cell upper region, especially at y = 95 mm, which highlights the intensification of the gas-lift effect.

On the other hand, the velocities remain constant across the different scenarios in the middle height (y = 50 mm), indicating that the central region of the channel is less sensitive to variations in the gas flow rate. The velocity profile for the polydisperse case, however, does not exhibit a clear increasing tendency in velocity. Notably, the case with Q_g = 15 mL/min shows the highest velocity peak, while the 20 mL/min case displays a more smoothed profile, suggesting that the heterogeneity of the dispersed phase influences the flow dynamics.

Figure 53 – Comparison of electrolyte velocity profiles along the geometry in the polydisperse two-phase case for different hydrogen gas volumetric flow rates

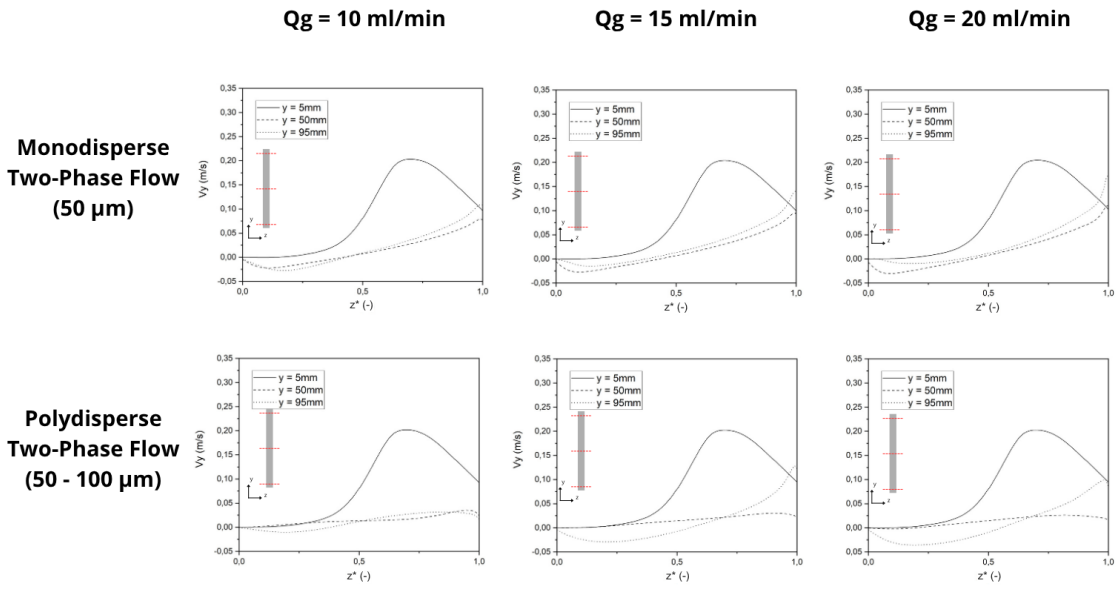

Source: The Author.

Figure 54 illustrates the gas volume fraction contours and, the Figure 55, the void fraction for the same scenarios. A relatively consistent gas distribution is observed in the monodisperse case as the gas flow rate increases. However, the higher the gas flow rate, the greater the amount of bubbles trapped on the opposite side of the electrode near the outlet. This accumulation

intensifies the electrolyte recirculation in that region, extending all the way to the cell bottom a behavior not observed in previous simulations with lower gas generation.

The behavior differs for the polydisperse case. The formation of gas accumulation points at the top of the domain is observed for Q_g = 15 mL/min. By increasing Q_g to 15 mL/min, recirculation with bubble entrapment is confirmed, as previously discussed.

Figure 54 – Comparison of electrolyte velocity contours along the geometry in the polydisperse two-phase case for different hydrogen gas flow rates

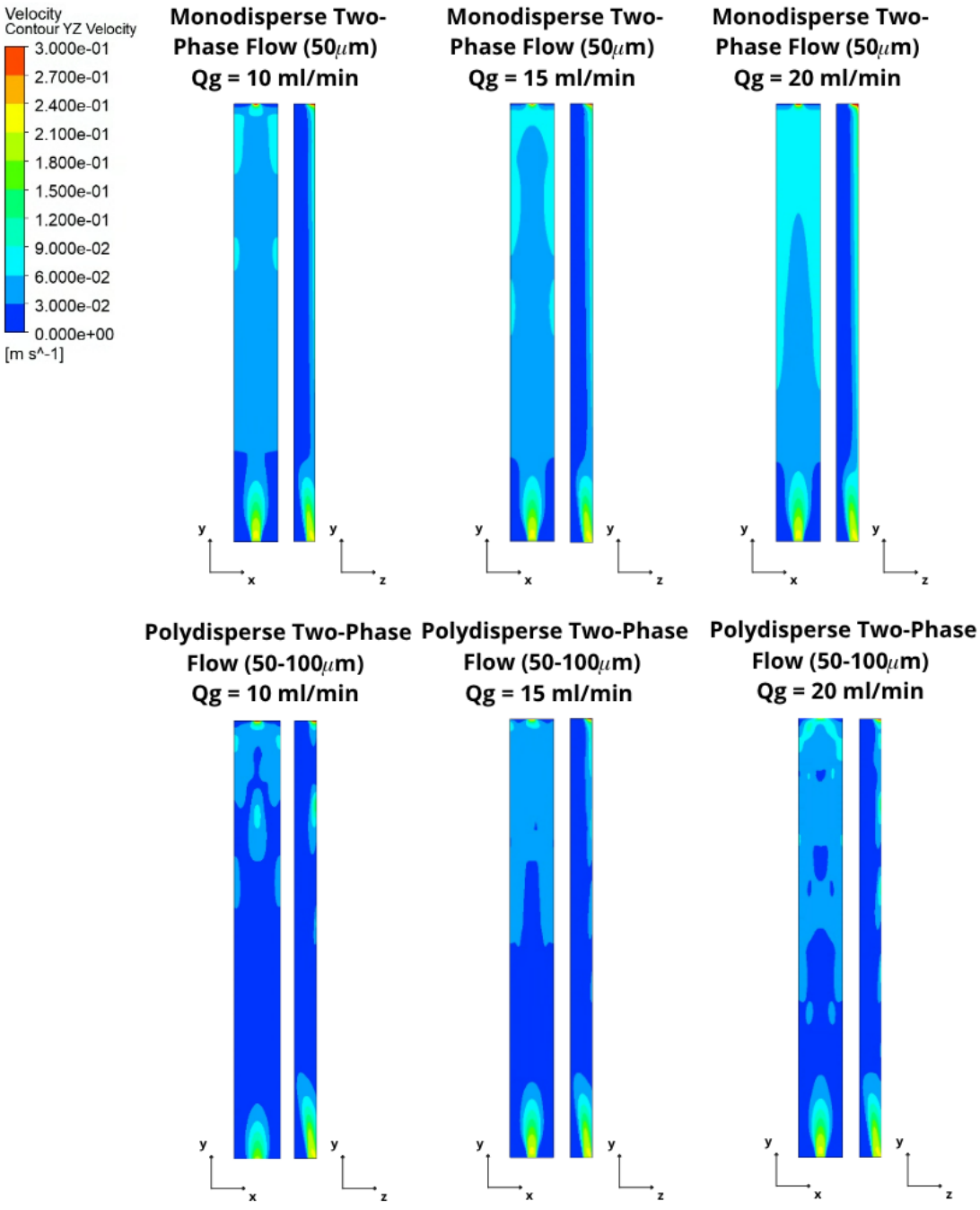

Source: The Author.

Finally, as demonstred in Figure 55, new gas accumulation points are identified along the electrode surface for the Q_g = 20 mL/min, promoting a more intense recirculation that now extends to the bottom of the cell, something not observed in any of the previously simulated polydisperse cases.

Figure 55 – Comparison of gas void fraction contours along the geometry in the polydisperse two-phase case for different hydrogen gas flow rates

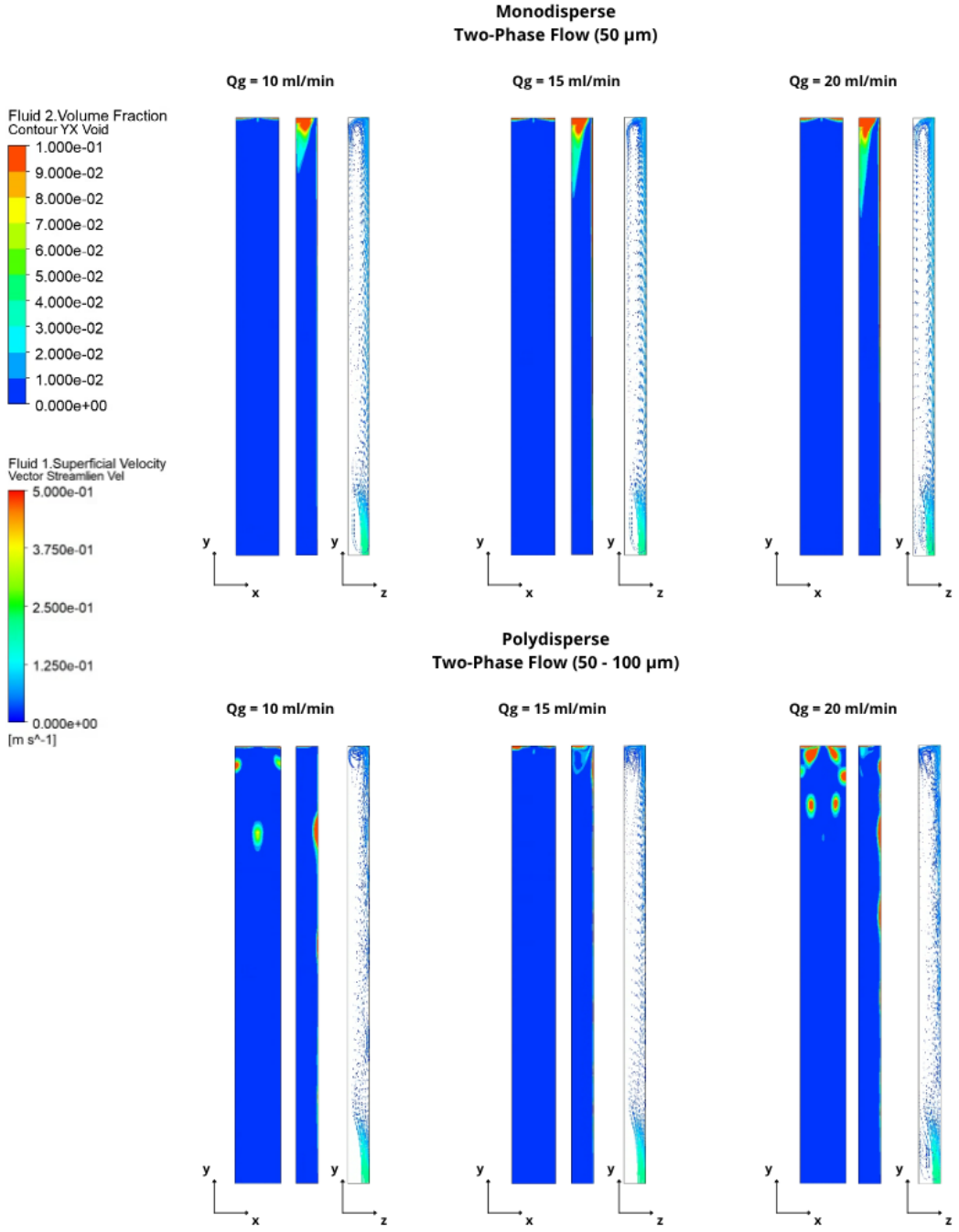

Source: The Author.

Table 11 presents the average gas volume fraction for the monodisperse case with a fixed bubble diameter of 50 μm under different hydrogen gas flow rates: Q_g = 10 mL/min, = 15

mL/min, and = 20 mL/min. The results indicate a clear positive correlation between the gas flow rate and the volume fraction of gas retained within the domain. As the flow rate increases from 10 to 20 mL/min, the average gas volume fraction rises from 2.044% to 3.194%. This behavior is expected, as higher gas injection rates introduce a greater number of bubbles into the system, increasing the amount of gas trapped in the electrolyte. The trend reinforces the sensitivity of two-phase flow characteristics to the gas inlet condition and highlights the need for careful control of gas flow rate in electrolysis systems to avoid excessive gas accumulation near the electrode surface.

Table 11 – Average gas volume fraction for monodisperse case (DB50) under different gas flow rates

Case	Q_g **= 10 mL/min**	Q_g **= 15 mL/min**	Q_g **= 20 mL/min**
50 μm	2.044%	2.657%	3.194%

Source: Author.

Table 12 presents the average gas volume fraction for the polydisperse case with a bubble size range of 50–100 μm, under three different hydrogen gas flow rates: Q_g = 10 mL/min, = 15 mL/min, and = 20 mL/min. The results demonstrate a progressive increase in the amount of gas retained within the domain as the gas flow rate rises. Specifically, the average void fraction increases from 0.919% at Q_g = 10 mL/min to 1.529% at Q_g = 20 mL/min. This behavior is consistent with expectations, as higher gas flow rates introduce a larger number of bubbles into the system, increasing overall gas retention.

Table 12 – Average gas volume fraction for polidisperse case (DB50-100) under different gas flow rates

Case	Q_g **= 10 mL/min**	Q_g **= 15 mL/min**	Q_g **= 20 mL/min**
50–100 μm	0.919%	1.188%	1.529%

Source: Author.

5 CONCLUSIONS AND SUGGESTIONS FOR FUTURE WORK

This study presents a detailed numerical investigation of gas–liquid two-phase flow in alkaline electrolytic cells, focusing on the modeling of the gas phase distribution generated electrochemically and its effects on the electrolyte flow profile. Single-phase, monodisperse two-phase, and polydisperse two-phase flow scenarios were simulated using ANSYS® CFX®, considering different bubble sizes, interfacial forces, and operating conditions.

Numerical simulations based on Computational Fluid Dynamics (CFD) have proven to be an essential tool in the study of electrolysis processes, enabling the analysis of phenomena that are difficult to observe experimentally. Investigating two-phase flow in an electrochemical system allows for the representation of complex phase interactions and significantly contributes to understanding bubble dynamics and phase coupling. The analyzes developed in this study enabled the representation of flow behavior within an electrolytic cell and provided valuable insights into the influence of operational parameter variations.

The comparative analysis with the literature showed that, despite the challenges of accurately replicating experimental data without access to all detailed input parameters from the original setup, the calibrated mathematical model was able to reproduce the qualitative patterns characteristic of the electrolysis phenomenon, such as the gas layer near the electrode and the distribution of bubbles within the domain.

The numerical analysis conducted using the geometry from Technische Universität Clausthal (TU Clausthal) revealed key characteristics that define the flow pattern and gas distribution: (i) A significant influence of the outlet channel on the electrolyte hydrodynamics was observed. Even in single-phase flow cases, recirculation zones were identified, which later persisted and intensified in two-phase flow simulations, acting as potential gas entrapment regions; (ii) The channel geometry favored the formation of gas entrapment zones caused by flow-induced vortices; (iii) The variation of operational parameters, such as the electrolyte flow rate and the gas flow rate of the generated gas, strongly influences the two-phase flow behavior within the electrolyte, affecting both the void fraction distribution and the dynamics of the velocity profile.

The numerical models exhibited substantial differences in representing bubble dynamics; however, it was possible to identify that the polydisperse model presented inaccuracies in the predicted results. Overall, the monodisperse model displayed a relatively homogeneous distribution of bubbles. In the tests involving variations of the electrolyte and gas volumetric flow rates, the velocity and void fraction patterns remained qualitatively consistent, with only their magnitudes increasing with the flow rate.

This behavior was not reproduced in the polydisperse model, where different bubble size groups were expected to exhibit greater heterogeneity. Although the model theoretically accounts for coalescence and breakup mechanisms, the results indicate an overestimation of bubble breakup, mainly due to the micrometer-scale dimensions of the bubbles, which led to a

predominance of the smallest group (group 1) throughout the domain. This predominance resulted in behavior more similar to a monodisperse two-phase flow.

Despite this limitation, the electrolyte velocity and gas void fraction contours still showed noticeable differences compared to the monodisperse case, indicating that the polydisperse model remained more sensitive to variations in operating conditions, even under the dominance of a single bubble size group caused by the breakup model inconsistency.
Overall, the main findings can be summarized as follows:

- The presence of the gas phase significantly alters the velocity profiles of the electrolyte, particularly in the upper regions of the cell, due to the gas-lift effect. It was observed that in all simulated cases (both polydisperse and monodisperse), there was an increase in the vertical velocity component (V_y) in the channel upper half. This effect became more pronounced with increasing gas volumetric flow rate, resulting in a greater rise in the upward electrolyte velocity. This highlights the potential of the dispersed phase to induce the flow of the continuous phase;

- A comparison between monodisperse and polydisperse cases showed clear differences in the average void fraction retained within the geometry. While the monodisperse model presented higher percentages of trapped gas, the polydisperse model resulted in lower averages, mainly due to the predominance of the smallest bubble group. The excessive breakup caused an unrealistic concentration of small bubbles, which are more easily carried by the electrolyte flow due to the stronger influence of the drag force.

- The monodisperse model proved to be less sensitive to variations in the two-phase flow dynamics observed in electrolysis. The electrolyte recirculation zones were not clearly detailed, and the bubble distribution remained relatively homogeneous, with interfacial forces exerting limited influence on the variations observed in the void fraction profile. The flow was predominantly governed by the drag force (F_D), while only the turbulent dispersion force (F_{TD}) showed a noticeable effect on the gas distribution, as demonstrated in the model sensitivity analysis.

- The polydisperse model, in turn, exhibited greater sensitivity to changes in interfacial forces and operational parameters, better reflecting the complexity of the two-phase flow system. Even with the predominance of the smallest size group, the MUSIG formulation allowed bubbles of different sizes to respond differently to the acting forces, leading to more diverse local flow structures and void fraction distributions.

- The bubble diameter directly influences the action of interfacial forces and the dispersion pattern: Smaller bubbles (50–100 μm) were more dispersed throughout the flow and more sensitive to the effects of the Turbulent Dispersion Force (F_{TD}). These smaller bubbles were more susceptible to interfacial forces and showed a stronger tendency to

become trapped in vortices, where the F_{DT} helps maintain them dispersed within the recirculation region. In contrast, larger bubbles (100–200 μm) were less affected by the F_{TD} due to their higher inertia. These bubbles tended to be less dispersed than smaller ones and were not trapped in the vortices. The Lift Force (F_L) played a more significant role for these larger bubbles by deflecting them toward the wall, which, combined with the wall lubrication force F_{WL} and lower effectiveness of the F_{TD}, resulted in a more concentrated accumulation of gas on the electrode surface. Overall, this analysis indicates that smaller bubbles promote a more homogeneous gas distribution and lower overall gas holdup, conditions that favor more effective gas removal near the electrodes. Consequently, operational or electrical parameters that lead to the generation of smaller bubbles are expected to enhance gas detachment efficiency and, therefore, improve the overall electrolysis performance.

- Both polydisperse cases (50–100 μm and 100–200 μm) demonstrated that the coalescence coefficient $C_{Coalescence}$=0.1 was insufficient to promote the significant formation of bubbles in groups with larger bubbles. As a result, most of the domain remained predominantly composed of bubbles from group 1. This outcome suggests that the coalescence rate needs to be significantly higher in order to achieve a broader distribution of bubble sizes. Moreover, the coalescence model adopted in this study includes the wake entrainment mechanism, which is primarily applicable to millimetric or large-deformable bubbles. For micrometric bubbles, this mechanism likely underestimates the frequency of interaction. Alternative formulations based on turbulent eddy collisions of the continuous phase would provide a more physically consistent representation for this scale.

- Even with the conservative break-up coefficient C_{Break}=0.01, the polydisperse model showed an excessive tendency toward bubble fragmentation. For micrometric bubbles, the breakup model proved unsuccessful in predicting realistic behavior, leading to an overestimation of small-size groups. This finding emphasizes the need for a careful evaluation of the applicability of breakup mechanisms at this scale.

- The increase of the electrolyte flow rate had a strong influence on the overall flow patterns. In the monodisperse case, the behavior was more homogeneous, whereas in the polydisperse case a nonlinear variation was observed with increasing flow rate. This effect is reinforced by the percentage of gas retained in the domain: in the monodisperse model, higher electrolyte flow rates resulted in lower gas holdup, while in the polydisperse case, particularly for the 100–200 μm range, the reduction in gas retention was not linear with the increase of the flow rate.

- The variation in gas flow rate significantly affected both the gas layer thickness and the electrolyte recirculation regions. Additionally, increasing the gas flow rate led to a

higher percentage of gas retained in the domain, a behavior consistently observed in both polydisperse and monodisperse cases.

5.1 Suggestions for Future Work

Based on the limitations and potential identified in this study, the following directions are suggested for future research:

- Extended sensitivity analyses are recommended to assess the actual necessity of the breakup model for micrometric bubbles and to identify more suitable coalescence mechanisms for this flow regime. As discussed in the conclusion section, the coalescence mechanism based on turbulent eddy collisions of the continuous phase is expected to provide a more physically consistent representation for micrometer-scale bubbles.
- Replication of the mathematical model in the full geometry of the Technische Universität Clausthal (TU Clausthal) to investigate the influence of additional inlet and outlet channels on the overall flow dynamics within the geometry. This step is essential to move from a simplified section to a complete representation of the electrolytic cell;
- Validation of the numerical model using experimental data extracted from the geometry of the Technische Universität Clausthal (TU Clausthal). This includes flow visualization techniques (e.g., PIV) that enable direct comparison of velocity profiles and bubble distribution, providing the detailed data required for calibration and validation;
- Implementation of more advanced multiphysics models, such as electrochemical–gas interaction, to more accurately represent the kinetics of hydrogen generation and its release. This integration would allow the gas production rate to be calculated dynamically, rather than imposed as a boundary condition;
- Geometric optimization of the electrolytic cell, considering design modifications to the channels or electrodes that promote more efficient gas phase removal and, consequently, improve the overall efficiency of electrolysis by mitigating the ohmic voltage drop induced by bubbles;

It is expected that the results and discussions presented in this work will contribute to the understanding and enhancement of two-phase flow modeling in electrolyzers, serving as a reference for future numerical and experimental studies in the field.

BIBLIOGRAPHY

ABDELOUAHED, L. *et al.* Current density distribution and gas volume fraction in the gap of lantern blade electrodes. **Chemical Engineering Research and Design**, Elsevier Ltd, v. 92, p. 559–570, aug 2014.

ABDELOUAHED, L. *et al.* Hydrodynamics of gas bubbles in the gap of lantern blade electrodes without forced flow of electrolyte: Experiments and cfd modelling. **Chemical Engineering Science**, Elsevier Ltd, v. 111, p. 255–265, 5 2014. ISSN 00092509.

ALDAS, K. Application of a two-phase flow model for hydrogen evolution in an electrochemical cell. **Applied Mathematics and Computation**, v. 154, p. 507–519, 7 2004. ISSN 00963003.

ALDAS, K. *et al.* Numerical and experimental investigation of two-phase flow in an electrochemical cell. **International Journal of Hydrogen Energy**, v. 33, p. 3668–3675, 7 2008. ISSN 03603199.

ALI, B. A.; PUSHPAVANAM, S. Analysis of unsteady gas–liquid flows in a rectangular tank: Comparison of euler–eulerian and euler–lagrangian simulations. **International Journal of Multiphase Flow**, v. 37, n. 3, p. 268–277, 2011.

ANSYS, Inc. **Ansys Documentation**. Canonsburg, PA, 2019. Accessed: 2019.

ANTAL, S. P. *et al.* Analysis of phase distribution in fully developed laminar bubbly two-phase flow. **Int. J. Multtphase Flow**, v. 17, 1991.

AUTON, T. R. *et al.* The force exerted on a body in inviscid unsteady non-uniform rotational flow. **Journal of Fluid Mechanics**, v. 197, p. 241–257, 1988. ISSN 14697645.

AVCI, A. C.; TOKLU, E. A new analysis of two phase flow on hydrogen production from water electrolysis. **International Journal of Hydrogen Energy**, Elsevier Ltd, v. 47, p. 6986–6995, 2 2022. ISSN 03603199.

AZEVEDO, H. S. de. **Estudo Numérico e Experimental do Escoamento Bifásico Líquido-Gás em um Rotor Centrífugo**. 2019. Dissertação (Mestrado) — Universidade Tecnológica Federal do Paraná, Curitiba, 2019. Programa de Pós-graduação em Engenharia Mecânica e de Materiais – PPGEM.

BALAT, M. Potential importance of hydrogen as a future solution to environmental and transportation problems. **International Journal of Hydrogen Energy**, v. 33, p. 4013–4029, 8 2008. ISSN 03603199.

BALL, M.; WEEDA, W. The hydrogen economy—vision or reality? *In*: ____. **Compendium of Hydrogen Energy: Hydrogen Use, Safety and the Hydrogen Economy: Volume 4**. [*S.l.*]: Elsevier, 2015. v. 4, p. 237–266. ISBN 9781782423645.

BERTODANO, M. L. D. *et al.* Phase distribution in the cap bubble regime in a duct. **Journal of Fluids Engineering, Transactions of the ASME**, v. 128, p. 811–818, 7 2006. ISSN 00982202.

BERTODANO, M. L. de. Turbulent bubbly flow in a triangular duct. **Rensselaer Polytechnic Institute**, 1991.

BERTOLA, F. *et al.* Momentum transfer in a swarm of bubbles: Estimates from fluid-dynamic simulations. **Chemical Engineering Science**, Elsevier Ltd, v. 59, p. 5209–5215, 2004. ISSN 00092509.

BESAGNI, G. *et al.* Computational fluid dynamics modelling of two-phase bubble columns: A comprehensive review. **Fluids**, v. 8, n. 3, p. 91, 2023.

BIDEAU, D. L. *et al.* Eulerian two-fluid model of alkaline water electrolysis for hydrogen production. **Energies**, MDPI AG, v. 13, 7 2020. ISSN 19961073.

BOISSONNEAU, P.; BYRNE, P. An experimental investigation of bubble-induced free convection in a small electrochemical cell. **Journal of Applied Electrochemistry**, v. 30, p. 767–775, 2000.

BURNS, A. D. *et al.* The favre averaged drag model for turbulent dispersion in eulerian multi-phase flows. **5th International Conference on Multiphase Flow, ICMF'04**, 2004.

CHANDRAN, P. *et al.* Study on the characteristics of hydrogen bubble formation and its transport during electrolysis of water. **Chemical Engineering Science**, Elsevier Ltd, v. 138, p. 99–109, 12 2015. ISSN 00092509.

CHARTON, S. *et al.* Hydrogen production by the westinghouse cycle: Modelling and optimization of the two-phase electrolysis cell. **WIT Transactions on Engineering Sciences**, WITPress, v. 65, p. 11–22, 2009. ISSN 17433533.

CHEN, P. Modeling the fluid dynamics of bubble column flows. **Washington University**, 2004.

CHENG, M. *et al.* Simulation of bubble-bubble interaction using a lattice boltzmann method. **Computers and Fluids**, v. 39, p. 260–270, 2 2010. ISSN 00457930.

CLIFT, R. *et al.* **Bubbles, Drops and Particles.** [*S.l.*]: Academic Press, 1978.

DANDY, D. S.; DWYER, H. A. A sphere in shear flow at finite reynolds number: effect of shear on particle lift, drag, and heat transfer. **J. zyxwvutsrqpo Fluid Mech. zyxwvutsrqp**, v. 216, p. 381410, 1990.

DAVIDSON, M. R. Numerical calculations of two-phase flow in a liquid bath with bottom gas injection: The central plume. **N.S. W.**, 2014.

DAWOOD, F. *et al.* Hydrogen production for energy: An overview. **International Journal of Hydrogen Energy**, Elsevier Ltd, v. 45, p. 3847–3869, 2 2020. ISSN 03603199.

DREW, D.; LAHEY, R. The virtual mass and lift force on a sphere in rotating and straining inviscid flow. **Int. J. Multiphase Flow**, v. 13, p. 113–121, 1987.

FRANK, T. *et al.* Validation of cfd models for mono- and polydisperse air-water two-phase flows in pipes. **Nuclear Engineering and Design**, v. 238, p. 647–659, 3 2008. ISSN 00295493.

FRANK, T. *et al.* Validation of cfd models for mono- and polydisperse air-water two-phase flows in pipes. **Nuclear Engineering and Design**, v. 238, p. 647–659, 3 2008. ISSN 00295493.

GONZALEZ, E. R.; TICIANELLI, E. A. **Eletroquímica: Princípios e Aplicações**. 2nd ed.. ed. [*S.l.*]: Editora da Universidade de São Paulo, 1998. 232 p.

HAMANN, C. H. *et al.* **Electrochemistry**. 2. ed.. ed. [*S.l.*]: Wiley-VCH, 2007. 531 p.

HULBURT, H. M.; KATZ, S. Some problems in particle technology a statistical mechanical formulation. **Chemical Engineering Science**, Pergamon Press Ltd, v. 19, p. 555–574, 1964.

ISHII, M.; HIBIKI, T. Thermo-fluid dynamics of two-phase flow. **Springer**, 2006.

ISHII, M.; MISHIMA, K. Two fluid model and hydrodynamic constitutive relations. **Nuclear Engineering and Design**, v. 82, p. 107–126, 1984.

ISHII, M.; ZUBER, N. **Drag Coefficient and Relative Velocity in Bubbly, Droplet or Particulate Flows**. Cambridge, MA: Massachusetts Institute of Technology, 1977. v. 73. 453 p. (Technical Report, v. 73).

JANSSEN, L. J. J. Effective solution resistivity in beds containing one monolayer or multilayers of uniform spherical glass beads. **Journal of Applied Electrochemistry**, v. 30, p. 507–509, 2000.

JOMARD, F. *et al.* Hydrogen filter press electrolyser modelled by coupling fluent ® and flux expert ® codes. **Journal of Applied Electrochemistry**, v. 38, p. 297–308, 3 2008. ISSN 0021891X.

JUPUDI, R. S. *et al.* Modeling bubble flow and current density distribution in an alkaline electrolysis cell. **Journal of Computational Multiphase Flows**, v. 1, n. 4, p. 341–347, 2009.

KIUCHI, D. *et al.* Ohmic resistance measurement of bubble froth layer in water electrolysis under microgravity. **Journal of The Electrochemical Society**, The Electrochemical Society, v. 153, p. E138, 2006. ISSN 00134651.

KOCAMUSTAFAOGULLARI, G.; ISHII, M. Foundation of the interracial area transport equation and its closure relations. **Int. J. Heat Mass Transfer**, v. 38, p. 481–493, 1995.

KRENZ, M. **Untersuchung des elektrodennahen Raumes gasentwickelnder Elektroden**. 1984. Dissertação (Mestrado) — Humboldt-Universität zu Berlin, Berlin, 1984.

KREPPER, E. *et al.* On the modelling of bubbly flow in vertical pipes. **Nucl. Eng. Des.**, v. 235, p. 597–611, 2005.

KREPPER, E. *et al.* The inhomogeneous musig model for the simulation of polydispersed flows. **Nuclear Engineering and Design**, v. 238, p. 1690–1702, 7 2008. ISSN 00295493.

KRISHNA, R.; BATEN, J. M. V. Scaling up bubble column reactors with the aid of cfd. **Institution of Chemical Engineers Trans IChemE**, v. 79, 2001.

LAHEY, R. T. *et al.* Phase distribution in complex geometry conduits. **Nuclear Engineering and Design**, v. 141, p. 177–201, 1993.

LEGENDRE, D.; MAGNAUDET, J. The lift force on a spherical bubble in a viscous linear shear flow. **Journal of Fluid Mechanics**, Cambridge University Press, v. 368, p. 81–126, 8 1998. ISSN 00221120.

LI, J. *et al.* Numerical simulation and analysis of a two-phase flow model considering bubble coverage for alkaline electrolytic water. **Applied Thermal Engineering**, v. 245, p. 122890, 2024.

LIAO, Y. *et al.* Baseline closure model for dispersed bubbly flow: Bubble coalescence and breakup. **Chemical Engineering Science**, Elsevier Ltd, v. 122, p. 336–349, 1 2015. ISSN 00092509.

LIMA, J. T. de; STARKE, A. R.; SILVA, A. K. da. Modeling multiphase flow dynamics in alkaline electrolysis for hydrogen production: A numerical approach. *In*: ABCM. **28th International Congress of Mechanical Engineering (COBEM 2025)**. Curitiba, Brazil, 2025. Paper COB-2025-2064.

LIU, C.-L. *et al.* Hydrodynamic characteristics of the two-phase flow field at gas-evolving electrodes: Numerical and experimental studies. **Royal Society Open Science**, v. 5, n. 5, p. 171255, 2018.

LIU, Y. *et al.* Experimental investigation and analysis for the bubble size distribution during alkaline water electrolysis by using a wire electrode. **DeCarbon**, v. 5, p. 100052, 2024.

LO, S. **Application of the MUSIG model to bubbly flows**. Aeat-1096. [*S.l.*]: AEA Technology, 1996.

LOTE, D. A. *et al.* Computational fluid dynamics simulations of the air-water two-phase vertically upward bubbly flow in pipes. **Industrial and Engineering Chemistry Research**, American Chemical Society, v. 57, p. 10609–10627, 8 2018. ISSN 15205045.

LUCAS, D. *et al.* Prediction of radial gas profiles in vertical pipe flow on the basis of bubble size distribution. **Int. J. Therm. Sci**, v. 40, p. 217–225, 2001.

LUCAS, D. *et al.* Evolution of flow patterns, gas fraction profiles and bubble size distributions in gas–liquid flows in vertical tubes. **Trans. Inst. Fluid-Flow Machinery**, v. 112, p. 37–46, 2003.

LUCAS, D. *et al.* Development of co-current air-water flow in a vertical pipe. **International Journal of Multiphase Flow**, v. 31, p. 1304–1328, 12 2005. ISSN 03019322.

LUCAS, D. *et al.* Use of models for lift, wall and turbulent dispersion forces acting on bubbles for poly-disperse flows. **Chemical Engineering Science**, v. 62, p. 4146–4157, 8 2007. ISSN 00092509.

LUO, H.; SVENDSEN, H. F. Theoretical model for drop and bubble breakup in turbulent dispersions. **AIChE Journal**, v. 42, n. 5, p. 1225–1233, 1996.

MANDIN, P. *et al.* Bubble over-potential during two-phase alkaline water electrolysis. **Electrochimica Acta**, Elsevier Ltd, v. 128, p. 248–258, 5 2014. ISSN 00134686.

MARFAING, O. *et al.* An analytical relation for the void fraction distribution in a fully developed bubbly flow in a vertical pipe. **Chemical Engineering Science**, Elsevier Ltd, v. 152, p. 579–585, 10 2016. ISSN 00092509.

MARTÍNEZ-BAZÁN, C. *et al.* On the breakup of an air bubble injected into a fully developed turbulent flow. part 1. breakup frequency. **Journal of Fluid Mechanics**, v. 401, p. 157–182, 1999.

MAT, M. D. *et al.* A two-phase flow model for hydrogen evolution in an electrochemical cell. **International Journal of Hydrogen Energy**, v. 29, p. 1015–1023, 8 2004. ISSN 03603199.

MCLAUGHLIN, J. B. Inertial migration of a small sphere in linear shear flows. **Journal of Fluid Mechanics**, v. 224, p. 261–274, 1991. ISSN 14697645.

MUDDE, R. F.; SIMONIN, O. Two- and three-dimensional simulations of a bubble plume using a two-fluid model. **Chemical Engineering Science**, v. 54, p. 5061–5069, 1999.

NAGAI, N.; ITO, T.; NISHIJIRI, N. Visualization and numerical simulation of two-phase flow between electrodes on alkaline water electrolysis. **Journal of Flow Visualization and Image Processing**, v. 17, n. 2, p. 99–112, 2010.

NAGAI, N. *et al.* Influences of bubbles between electrodes onto efficiency of alkaline water electrolysis. **Proceedings of PSFVIP-4**, 2003.

OEY, R. S. *et al.* Sensitivity study on interfacial closure laws in two-fluid bubbly flow simulations. **AIChE Journal**, v. 49, p. 1621–1636, 7 2003. ISSN 00011541.

PANT, K. K.; GUPTA, R. B. **Hydrogen fuel: production, transport and storage**. [*S.l.*]: CRC Press, 2009.

POPE, S. B. **Turbulent Flows**. Cambridge, UK: Cambridge University Press, 2000.

PRINCE, M. J.; BLANCH, H. W. Bubble coalescence and break-up in air-sparged bubble columns. **AIChE J.**, v. 36 (10), p. 1485–1499, 1990.

RODRíGUEZ, J.; AMORES, E. Cfd modeling and experimental validation of an alkaline water electrolysis cell for hydrogen production. **Processes**, MDPI AG, v. 8, p. 1–17, 12 2020. ISSN 22279717.

ROSA, E. S. Escoamento multifásico isotérmico: Modelos de multifluidos e de mistura. **Bookman**, 2012.

RUE, R. D. L. *et al.* On the conductivity of dispersions. **93. N. Chtani, Sci. Repts. Research Inst., Tohoku Univ**, v. 106, p. 547, 1953.

RZEHAK, R.; KREPPER, E. Closure models for turbulent bubbly flows: A cfd study. **Nuclear Engineering and Design**, v. 265, p. 701–711, 2013. ISSN 00295493.

SAFFMAN, P. G. The lift on a small sphere in a slow shear flow. **J. Fluid Mech**, v. 22, p. 385–400, 1965.

SANKARANARAYANAN, K.; SUNDARESAN, S. Two-fluid model and hydrodynamic constitutive relations. **Chem. Eng. Sci.**, v. 57, p. 3521–3542, 2002.

SATO, Y.; SEKOGUCHI, K. Liquid velocity distribution in two-phase bubble flow. **International Journal of Multiphase Flow**, v. 2, n. 1, p. 79–95, 1975.

SCHMIDTKE, M. *et al.* Vof-simulation of the rise behaviour of single air bubbles in linear shear flows. **In: Conference on Transport Phenomena with Moving Boundaries**, 2005.

SHANG, Z. A novel drag force coefficient model for gas-water two-phase flows under different flow patterns. **Nuclear Engineering and Design**, Elsevier Ltd, v. 288, p. 208–219, 5 2015. ISSN 00295493.

SIMONNET, M. *et al.* Experimental determination of the drag coefficient in a swarm of bubbles. **Chemical Engineering Science**, v. 62, p. 858–866, 2 2007. ISSN 00092509.

SUN, X. *et al.* Liquid velocity in upward and downward air-water flows. **Annals of Nuclear Energy**, v. 31, p. 357–373, 3 2004. ISSN 03064549.

TOMIYAMA, A. Struggle with computational bubble dynamics. **Multiphase Science and Technology**, v. 10, p. 369–405, 1998.

TOMIYAMA, A. *et al.* Effects of eötvös number and dimensionless liquid volumetric flux on lateral motion of a bubble in a laminar duct flow. **Adv. Multiphase Flow**, p. 3–15, 1995.

TOMIYAMA, A. *et al.* Transverse migration of single bubbles in simple shear rows. **Chemical Engineering Science**, v. 57, p. 1849–1858, 2002. Disponível em: www.elsevier.com/locate/ces.

WANG, M. *et al.* The intensification technologies to water electrolysis for hydrogen production - a review. **Renewable and Sustainable Energy Reviews**, Elsevier Ltd, v. 29, p. 573–588, 2014. ISSN 13640321.

WANG, S. K. *et al.* 3-d turbulence structure and phase distribution measurements in bubbly two-phase flows. **Int. J. Multiphase Flo** , v. 13, p. 327–330, 1987.

WANG, T.; WANG, J.; JIN, Y. Theoretical prediction of flow regime transition in bubble columns by the population balance model. **Chemical Engineering Science**, v. 60, n. 23, p. 6199–6209, 2005.

WEAST, R. C. **Handbook of Chemistry and Physics.** 57. ed. [*S.l.*]: CRC Press, 1976.

XU, W. *et al.* Numerical simulation of gas–liquid two-phase flow cfd–pbm model in a micro–nanobubble generator. **Minerals**, v. 12, n. 10, p. 1270, 2022.

YAMOAH, S. *et al.* Numerical investigation of models for drag, lift, wall lubrication and turbulent dispersion forces for the simulation of gas-liquid two-phase flow. **Chemical Engineering Research and Design**, Institution of Chemical Engineers, v. 98, p. 17–35, 6 2015. ISSN 02638762.

YAN, Y. *et al.* Numerical investigation of indoor particulate contaminant transport using the eulerian-eulerian and eulerian-lagrangian two-phase flow models. **Experimental and Computational Multiphase Flow**, Tsinghua University Press, v. 2, p. 31–40, 3 2020. ISSN 26618877.

YEOH, G. H.; TU, J. Computational techniques for multi-phase flows. **Elsevier**, 2009.

ZENG, K.; ZHANG, D. Recent progress in alkaline water electrolysis for hydrogen production and applications. **Progress in Energy and Combustion Science**, v. 36, p. 307–326, 6 2010. ISSN 03601285.

ZHAN, S. *et al.* 3d numerical simulations of gas–liquid two-phase flows in aluminum electrolysis cells with the coupled model of computational fluid dynamics–population balance model. **Industrial & Engineering Chemistry Research**, v. 56, n. 31, p. 8649–8662, 2017.

ZHAN, S. *et al.* Cfd simulation of effect of interphase forces and turbulence models on gas–liquid two-phase flows in non-industrial aluminum electrolysis cells. **JOM**, 2017.

ZHANG, Z. *et al.* Three-dimensional simulation of two-phase flow distribution in spherical concave-convex shaped flow field for alkaline water electrolyzer. **International Journal of Hydrogen Energy**, v. 48, n. 33, p. 33401–33410, 2023.